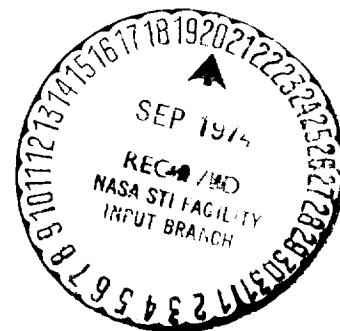


NASA TMX-72525

TIROS III RADIATION DATA USERS' MANUAL

By
Staff Members
of the
Aeronomy and Meteorology Division
Goddard Space Flight Center
National Aeronautics and Space Administration



August, 1962

FOREWORD

Many members of the staff of the Aeronomy and Meteorology Division contributed to the success of the TIROS III scanning radiometer experiment. Valuable contributions in the areas of laboratory measurements of materials and computer programming for data processing came from the Meteorological Satellite Laboratory, U. S. Weather Bureau, whose efforts are gratefully acknowledged.

The task of assembling the information contained in this manual into written form suitable for publication was largely accomplished by Mrs. I. Persano Strange and Mr. Robert Hite, Aeronomy and Meteorology Division, whose efforts are hereby acknowledged.

A companion volume, the "TIROS III Radiation Data Catalog," will be published approximately concurrently with this manual.

ABSTRACT

The NASA TIROS III Meteorological Satellite contains a five-channel medium resolution scanning radiometer. Two of the channels of this instrument are sensitive to reflected solar radiation and the remaining three respond to emitted radiation from the earth and its atmosphere. The three thermal channels are calibrated in terms of equivalent black-body temperatures, and the visible channels in terms of effective radiant emittances. The calibration data, along with orbital and attitude data and the radiation data from the satellite, were incorporated in a computer program for an IBM 7090 which was used to produce the "Final Meteorological Radiation Tape (Binary)."

After launch, the radiometer displayed the same degradation characteristics as did its predecessor in TIROS II. The onset of degradation, beginning at different time periods after launch for the different channels, results in a departure of the data from the pre-launch laboratory calibration. Since the cause of the problem has not been pinpointed, no changes were made on the TIROS III radiometer calibration. This matter still is being studied at the Goddard Space Flight Center.

Before serious work with the TIROS III radiation data is attempted, an understanding of the radiometer, its calibration, and the problems encountered in the experiment is essential. The instrumentation design, development work, and the calibrations herein described were performed by the Goddard Space Flight Center staff, whereas the computer and programming efforts were carried out jointly by the Meteorological Satellite Laboratory staff, U. S. Weather Bureau, and the Goddard Space Flight Center staff.

In this manual, the radiometer and its calibration, data processing, and degradation and other possible sources of error are discussed.

TABLE OF CONTENTS

	Page
Abstract	iii
List of Common Symbols	vi
I. Introduction	1
1.1 The TIROS III Program	1
1.2 Geographic Limitations of Data Utilization	1
1.3 Description of the Principle of the Radiometer	1
II. Calibration	1
2.1 Effective Spectral Response	2
2.1.1 Definition	2
2.1.2 Discussion	2
2.2 Effective Radiant Emittance	3
2.2.1 Definition	3
2.2.2 \bar{W} vs. T_{BB}	3
2.3 Flow Sequence	3
2.4 Relation Between Electronics and Radiometer Temperatures	3
2.5 Space-Viewed Level	3
2.6 Target Blackbody Temperature, T_{BB} , and Target Effective Radiant Emittance, \bar{W} , vs. Digital Number, D	3
2.6.1 Thermal Channels 1, 2 and 4	3
2.6.2 Visible Channels 3 and 5	4
2.7 Summary of the Calibration	4
III. Data Processing	4
3.1 Information Flow in the Satellite	4
3.2 Information Flow at the Command and Data Acquisition Station	5
3.3 Information Flow at the Data Reduction Center	5
IV. Format of the Final Meteorological Radiation Tape (Binary)	6
V. IBM 7090 Computer Flow Diagram	8
VI. Pre-Launch and Post-Launch Observations and Developments	8
6.1 Pre-Launch Degradation of Channels 3 and 5	8
6.2 Post-Launch Degradation of Channels 1, 2, 4 and 5	9
6.3 Estimate of the Accuracy of the Data	9
VII. Conclusions	10
VIII. References and Bibliography	10

LIST OF FIGURES

Figure		Page
1.	Block Diagram of the Scanning Radiometer	13
2.	ϕ_λ vs. λ , Channel 1	14
3.	ϕ_λ vs. λ , Channel 2	15
4.	ϕ_λ vs. λ , Channel 3	16
5.	ϕ_λ vs. λ , Channel 4	17
6.	ϕ_λ vs. λ , Channel 5	18
7.	\bar{W} vs. T_{BB} , Channel 1	19
8.	\bar{W} vs. T_{BB} , Channel 2	20
9.	\bar{W} vs. T_{BB} , Channel 4	21
10.	Calibration Flow Diagram	22
11.	F_{SC} vs. V_{RAD} , Channel 1	23
12.	F_{SC} vs. V_{RAD} , Channel 2	24
13.	F_{SC} vs. V_{RAD} , Channel 3	25
14.	F_{SC} vs. V_{RAD} , Channel 4	26
15.	F_{SC} vs. V_{RAD} , Channel 5	27
16.	T_C and T_E vs. Orbit Number	28
17.	T_{BB} vs. D at $T_C = 0^\circ\text{C}$, Channel 1	29
18.	T_{BB} vs. D at $T_C = 7^\circ\text{C}$, Channel 1	30
19.	T_{BB} vs. D at $T_C = 12^\circ\text{C}$, Channel 1	31
20.	T_{BB} vs. D at $T_C = 18^\circ\text{C}$, Channel 1	32
21.	T_{BB} vs. D at $T_C = 23.5^\circ\text{C}$, Channel 1	33
22.	T_{BB} vs. D at $T_C = 30^\circ\text{C}$, Channel 1	34
23.	T_{BB} vs. D at $T_C = 0^\circ\text{C}$, Channel 2	35
24.	T_{BB} vs. D at $T_C = 7^\circ\text{C}$, Channel 2	36
25.	T_{BB} vs. D at $T_C = 12^\circ\text{C}$, Channel 2	37
26.	T_{BB} vs. D at $T_C = 18^\circ\text{C}$, Channel 2	38
27.	T_{BB} vs. D at $T_C = 23.5^\circ\text{C}$, Channel 2	39
28.	T_{BB} vs. D at $T_C = 30^\circ\text{C}$, Channel 2	40
29.	\bar{W} vs. D at $T_C = 0^\circ\text{C}$, Channel 3	41
30.	\bar{W} vs. D at $T_C = 7^\circ\text{C}$, Channel 3	42
31.	\bar{W} vs. D at $T_C = 12^\circ\text{C}$, Channel 3	43
32.	\bar{W} vs. D at $T_C = 18^\circ\text{C}$, Channel 3	44
33.	\bar{W} vs. D at $T_C = 23.5^\circ\text{C}$, Channel 3	45
34.	\bar{W} vs. D at $T_C = 30^\circ\text{C}$, Channel 3	46
35.	T_{BB} vs. D at $T_C = 0^\circ\text{C}$, Channel 4	47

Figure

36. T_{BB} vs. D at $T_C = 7^\circ\text{C}$, Channel 4	48
37. T_{BB} vs. D at $T_C = 12^\circ\text{C}$, Channel 4	49
38. T_{BB} vs. D at $T_C = 18^\circ\text{C}$, Channel 4	50
39. T_{BB} vs. D at $T_C = 23.5^\circ\text{C}$, Channel 4	51
40. T_{BB} vs. D at $T_C = 30^\circ\text{C}$, Channel 4	52
41. \bar{W} vs. D at $T_C = 0^\circ\text{C}$, Channel 5	53
42. \bar{W} vs. D at $T_C = 7^\circ\text{C}$, Channel 5	54
43. \bar{W} vs. D at $T_C = 12^\circ\text{C}$, Channel 5	55
44. \bar{W} vs. D at $T_C = 18^\circ\text{C}$, Channel 5	56
45. \bar{W} vs. D at $T_C = 23.5^\circ\text{C}$, Channel 5	57
46. \bar{W} vs. D at $T_C = 30^\circ\text{C}$, Channel 5	58
47. Calibration Flow Diagram	59
48. Block Diagram of the Radiation Experiment in the Satellite	60
49. Block Diagram of Information Flow at a Data Acquisition Station, Including Auxiliary Uses of the Radiation Data	61
50. Block Diagram of Information Flow at the Data Reduction Center in Producing a Digital Magnetic Tape for Computer Input	62
51. Interpretation of FMR Tape Format	63
52. (a, b, c, and d) Flow Diagram for the IBM 7090 Computer Program Used in Reducing the Radiation Data	64
53. Flight Space Level minus Calibrated Space Level (Δf) vs. Orbit Number, Channel 1	68
54. Flight Space Level minus Calibrated Space Level (Δf) vs. Orbit Number, Channel 2	69
55. Flight Space Level minus Calibrated Space Level (Δf) vs. Orbit Number, Channel 4	70
56. Ratio of \bar{W}_s/\bar{W}_s^* to \bar{W}_s/\bar{W}_s^* vs. Orbit Number	71

LIST OF TABLES

I. Mean Orbital Characteristics of TIROS III	1
II. Filter and Lens Materials	11
III. Effective Spectral Response, Channel 1	11
IV. Effective Spectral Response, Channel 2	11
V. Effective Spectral Response, Channel 3	11
VI. Effective Spectral Response, Channel 4	11
VII. Effective Spectral Response, Channel 5	12
VIII. T_{BB} vs. \bar{W} , Channel 1	12
IX. T_{BB} vs. \bar{W} , Channel 2	12
X. T_{BB} vs. \bar{W} , Channel 4	12
XI. Changes in T_{BB} and \bar{W} due to Differences of T_C from T_E	12

LIST OF COMMON SYMBOLS

A_λ	Spectral absorptivity of the thermistor detector
D	Digital Number: scale 0 to 127
F	Number of cycles-per-second above the base frequency of a given 50 c.p.s. subcarrier band
Δf	The flight measured space level (both directions viewing outer space) minus the ground-calibrated "space" level (both directions viewing black bodies of liquid nitrogen temperatures (-196°C)) in terms of cycles-per-second of a given 50 c.p.s. subcarrier band
F_{SC}	Output frequency of the voltage controlled oscillator
J_λ	Spectral radiant intensity of visible light source, i.e., a standard tungsten lamp or the sun (watts/steradian)
R_λ^B	Spectral reflectivity of the black half of the chopper disk
R_λ^M	Spectral reflectivity of the aluminized half of the chopper disk
R_λ^P	Spectral reflectivity of the radiometer prism
R_λ	The ratio R_λ^B/R_λ^M
$R_{\lambda\lambda}$	Spectral reflectivity of SiO_2 or BaF_2
R	Distance from the visible light source to the center of the diffuse reflector
T_{BB}	Equivalent blackbody temperature (degrees Kelvin)
T_C	Radiometer housing temperature
T_E	Satellite electronics temperature
$W_\lambda(T)$	Spectral radiant emittance (the Planck function) for a blackbody of temperature T (watts/meter ² /micron)
\bar{W}	Effective radiant emittance defined by eq. (6) for channels 1, 2, and 4, and defined by eq. (9) for channels 3 and 5 (watts/meter ²)
\bar{W}^*	Defined by eq. (10)
V_{RAD}	Output voltage of the radiometer
f_λ	Spectral transmission of the filter-lens combinations in the radiometer
r_λ	Spectral reflectivity of the diffuse reflector employed in the calibration of the visible channels
τ_λ	Spectral transmission of SiO_2 or BaF_2 , defined by eq. (5)
Ω	Solid angle of the sun as viewed from the earth
γ	Incidence angle of radiation from visible light source impinging upon diffuse reflector employed in the calibration of the visible channels
λ	Wavelength in microns
ϕ_λ	Effective spectral response of the radiometer defined by eqs. (1), (2) and (3)

I. INTRODUCTION

1.1 The TIROS III Program^{1,2,3,4}

The NASA TIROS III Meteorological Satellite was injected into orbit on July 12, 1961. Its mean orbital characteristics are listed in Table I.

TABLE I

Perigee Altitude.....	460.1 st. mi.
Apogee Altitude.....	506.8 st. mi.
Inclination.....	47.90°
Anomalistic Period.....	100.41 min.

The instrumentation flown in the satellite includes two television cameras and three radiometers. The radiometers measure emitted and reflected solar radiation from the earth and its atmosphere. One is a wide field non-scanning instrument having two detectors, one white and the other black. A second radiometer is the University of Wisconsin's heat balance experiment. This manual is concerned only with the third radiation measuring device, the five-channel medium resolution scanning radiometer.

1.2 Geographic Limitations of Data Utilization

Before attempting to interpret the data contained on the "Final Meteorological Radiation Tape (Binary)," careful consideration should be given to all points discussed in this manual. For an understanding of the significance of the radiant emittance values or equivalent blackbody temperatures, a familiarity with the principle of the radiometer, its peculiarities, and the method of calibration is essential.

Care should be exercised in the use of the correlation of the radiation data with geographic location, such as attempted comparisons with synoptic situations. Uncertainties in attitude lead to an estimated maximum error of 1° to 2° in great circle arc. At a nadir angle of 0°, a 2° error would result in a position error on the surface of the earth of less than 20 miles. At a nadir angle of 60°, a 2° error corresponds to an error of more than 200 miles. It should be emphasized that such errors result in distortion as well as translation, and a simple linear shift of the data is in general not sufficient for correction.^{5,6,7,8,9}

In addition to attitude errors, time errors also contribute to difficulties in geographic correlation. The principal sources of time errors are mistakes at the ground station in transmission of the end-of-tape pulse, erroneous sensing by the analog-to-digital converter of the end-of-tape pulse, and the necessity of counting through noise on the relative satellite clock frequency. These errors are generally estimated to be less than ten seconds in TIROS III, much less than in TIROS II. However, users are cautioned to be watchful for those rare cases where there still might be larger errors of the order of one minute or more. Time errors also result in distortion as well as translation.

1.3 Description of the Principle of the Radiometer^{1,2}

The principle of the radiometer is illustrated in Fig. 1 where the components of a single channel are pictured. The fields of view of the channels are approximately coincident, each being about five degrees wide at the half-power points of the response. The optical axis of each channel is bi-directional 180° apart. As the half-aluminized, half-black chopper disk rotates, radiation from first one direction and then the other reaches the detector. This results in a chopped output which is amplified and rectified, giving a DC signal which (neglecting electronic noise and possible optical imbalance) is theoretically proportional to the difference in energy flux viewed in the two directions.

The radiometer is mounted in the satellite such that the optical axes are inclined 45° to the satellite spin axis. (The viewing directions are designated "wall" and "floor" according to their orientation in the satellite.) When one optic views the earth, the other views outer space. Thus, the outer space radiation level (assumed to be zero) can be used as a reference. When both optics are viewing outer space, the resultant signal is designated as the "space viewed level." Theoretically, this signal should be zero, but in reality is not, due to electronic noise and any initial optical imbalance, plus subsequent changes in balance caused by the degradation of certain channels after varying time periods in orbit, thus altering the laboratory calibration. As the satellite rotates on its axis, the radiometer scan pattern on the surface of the earth is defined by the intersection of a 45° half-angle cone and a sphere. This pattern ranges from a circle when the spin vector is parallel to the orbital radius vector, to two hyperbola-like branches when the spin vector is perpendicular to the radius vector. The orbital motion of the satellite provides the scan advance. Variations in the amplitude of the radiometer signal are converted into subcarrier frequency deviations and stored by means of a miniature magnetic tape recorder. When the satellite is interrogated while passing over a Command and Data Acquisition Station, the information is telemetered back to earth where it is recorded on magnetic tape. The further processing of these magnetic tapes is discussed in Section III of this manual.

II. CALIBRATION

Before considering the calibration flow sequence, it is necessary to define and discuss two quantities which are fundamental to the calibration. These are the effective spectral response and the effective radiant emittance.

2.1 Effective Spectral Response

2.1.1 *Definition.* The effective spectral response, ϕ_λ , is defined as

$$\phi_\lambda = R'_\lambda(R'_\lambda - R''_\lambda)f_\lambda A_\lambda \quad (1)$$

In the actual computation of ϕ_λ , either the expression

$$\phi_\lambda = R'_\lambda(1 - R''_\lambda)f_\lambda \quad (2)$$

or the expression

$$\phi_\lambda = R'_\lambda(R'_\lambda - R''_\lambda)f_\lambda \quad (3)$$

was used. The use of the factor $(1 - R''_\lambda)$ assumes that the reflectivity of the aluminized half of the chopper disk is independent of wavelength. In both equations (2) and (3), it is assumed that the detector absorptivity is independent of wavelength. However, recent laboratory measurements using sample bolometers of the type used in the radiometer indicate that the spectral absorptivity of the detectors is flat between 0.25 and 2.0 microns, but varies somewhat and generally decreases beyond 2.0 microns.

The materials used in the lens and filter of each channel are given in Table II. The effective spectral response for each channel is given in Figs. 2 through 6 and in Tables III, IV, V, VI and VII.

2.1.2 *Discussion.* The quantity R_λ for channels 2 and 4 was taken from measurements performed at the Meteorological Satellite Laboratory of the Weather Bureau, using a Beckman IR-7 spectrophotometer. The determinations were made on two different chopper disks taken from a radiometer similar to that flown in TIROS III. An average of the two was taken and used for channels 2 and 4. The value $(R'_\lambda - R''_\lambda)$ was measured with the TIROS III chopper disks by the Barnes Engineering Company for channels 1, 3 and 5.

A discussion of the final values of ϕ_λ derived for each channel follows:

CHANNEL 1

The function f_λ was taken from Barnes Engineering Company measurements made on the channel 1 filter of the TIROS III radiometer in combination with plane samples of the lens elements. The hemispherical germanium immersion lens used in this channel was found to have wavelength-independent transmission in this spectral region, but this constant was incorporated into the f_λ function. The function R'_λ was taken from a Barnes measurement on a good $\lambda/4$ front-surfaced aluminum mirror.

CHANNEL 2

The filter function was taken from measurements made on a similar filter by the Meteorological Satellite Laboratory of the Weather Bureau. The transmission of the germanium doublet lens was obtained by squaring a measurement made by Barnes on a plane sample of lens material having a thickness equivalent to the mean thickness of one of the lens elements. The product of filter-lens combination was used as the function f_λ . The function R'_λ was taken from a Barnes measurement on a good $\lambda/4$ front-surfaced aluminum mirror. Beyond 16μ , due to lack of measurements, the reflectivity was assumed to be constant at the 16μ value.

CHANNEL 3

Barnes measurements were used for the sapphire (Al_2O_3) lens. For the barium fluoride (BaF_2) lens, the transmissivity was computed from the index of refraction of BaF_2 , measured at varying wavelengths by the University of Michigan.¹⁰

Assuming that the barium fluoride provided reflection losses only, the reflectivity was determined by the equation.

$$R_{e\lambda} = \left(\frac{N_\lambda - 1}{N_\lambda + 1} \right)^2 \quad (4)$$

where N_λ is the spectral index of refraction, and the transmissivity was determined by the equation

$$\tau_\lambda = (1 - R_{e\lambda})^2 \quad (5)$$

The function $f(\lambda)$ was obtained from the product of the transmissivities of the two lenses.

The function R'_λ was taken from an average of measurements taken by Barnes on the two reflecting surfaces of the prisms from radiometers 102A and 103A and from a Barnes measurement on a good $\lambda/4$ front-surfaced aluminum mirror.

CHANNEL 4

The function f_λ was taken from measurements made by the Eastman Kodak Company on a sample InSb filter. The transmission of the KRS-5 lens was found to be constant throughout the entire 7.4 to 32.6μ range and was not included in the transmission. The function R'_λ was taken from a Barnes measurement on a good $\lambda/4$ front-surfaced aluminum mirror. Beyond 16μ , due to lack of measurements, the reflectivity was assumed to be constant at the 16μ value.

CHANNEL 5

Barnes measurements were used for the sapphire (Al_2O_3) lens. For the silicon dioxide (SiO_2)

lens, the transmissivity was computed from the index of refraction of SiO_2^{10} , in the same manner as the transmissivity was computed for the BaF_2 lens in channel 3. The filter measurements for this channel were made by Barnes. The function $f(\lambda)$ was obtained from the products of the transmissivities of the two lenses and the filter.

The function R_λ^P was taken from an average of measurements taken by Barnes on the two reflecting surfaces of the prisms from radiometers 102A and 103A and from a Barnes measurement on a good $\lambda/4$ front-surfaced aluminum mirror.

2.2 Effective Radiant Emittance

2.2.1 Definition. The effective radiant emittance of a target, \bar{W} , for channels 1, 2 and 4 is defined as that portion of blackbody radiant emittance which would be detected by a sensor with a spectral response ϕ_λ when the field of view is completely filled. This may be written as

$$\bar{W} = \int_0^\infty W_\lambda(T) \phi_\lambda d\lambda \quad (6)$$

The effective radiant emittance for channels 3 and 5 is defined by eq. (9) below.

2.2.2 \bar{W} vs. T_{BB} . The \bar{W} vs. T_{BB} functions in Tables VIII, IX, and X and Figs. 7 through 9 were obtained using equation (6). The integration necessary in the computation of each point was carried out using an LGP-30 electronic computer.

2.3 Flow Sequence

The radiation data flow sequence is shown in Fig. 10. The sequence from satellite through ground station is illustrated in Fig. 10(a). When a blackbody temperature T_{BB} is viewed by one side of the radiometer while the other side views outer space, and with a radiometer housing temperature, T_C , a radiometer output voltage V_{RAD} is obtained. This signal is fed into a voltage controlled oscillator which produces an output frequency F_{SC} when the oscillator electronics temperature is T_E .

At the ground station the frequency F_{SC} , now increased by a factor of 30, is fed into a demodulator, the output of which enters an analog-to-digital converter. The resulting digital number D and the temperature T_C , which is also telemetered from the satellite, are used to obtain the value T_{BB} for channels 1, 2 and 4 and the value \bar{W} for channels 3 and 5 from the calibration data as indicated below.

2.4 Relation Between Electronics and Radiometer Temperatures

The relation between the radiometer output voltage, V_{RAD} , and the frequency output of the voltage controlled oscillator, F_{SC} , depends on the electronics temperature, T_E , as shown sche-

matically in Fig. 10(c). Algebraically, the relation may be expressed as

$$F_{SC} = f(V_{RAD}, T_E) \quad (7)$$

However, it may be seen from the five-channel subcarrier oscillator curves, Figs. 11-15, that output frequency is relatively independent of T_E for small variations in T_E . Thus, it was assumed that if T_E did not differ appreciably from T_C , the final calibration of T_{BB} or \bar{W} vs. F_{SC} could be carried out by keeping T_E equal to T_C and considering T_C as the variable parameter, as shown schematically in Fig. 10(c).

The validity of the TIROS III calibration and its effect on the accuracy of the results was checked using the flight data for T_E and T_C . The temperature comparison of T_E and T_C for TIROS III is shown in Fig. 16. It is seen from the graph that the difference between T_E and T_C did not exceed 5.5°C. Using Figs. 11-15 and Figs. 17-46, it was determined that for a 5.5°C temperature difference between T_C and T_E the maximum average temperature difference in the thermal channels is 0.8°K, while the maximum average difference in effective radiant emittances in the visible channels, expressed in percentage of one solar constant radiated from a diffuse source, is 0.2% as seen in Table XI.

2.5 Space Viewed Level

The TIROS II calibration method assumed that the radiometer was in perfect balance at all radiometer housing temperatures. However, from the TIROS II flight data, the signal obtained when both optics viewed outer space evidenced a variable property, seemingly dependent upon the radiometer housing temperature. These results were verified in the laboratory by simulating outer space conditions with two targets at liquid nitrogen temperatures. (The signal obtained at liquid nitrogen temperatures is so small that it may be compared with the very low "space" temperature.)

A new calibration procedure was adapted to account for this space level shift.

2.6 Target Blackbody Temperature, T_{BB} , and Target Effective Radiant Emittance, \bar{W} , vs. Digital Number, D

Unlike the TIROS II calibration, it was possible to calibrate the TIROS III radiometer and its electronics data storage package as a system. The radiometer was placed in a vacuum chamber, while the electronics canister was placed in a thermally-insulated environmental chamber.

2.6.1 Thermal Channels 1, 2 and 4. Two laboratory blackbody targets, placed in a container so that liquid or gaseous nitrogen could flow around them, were used in the calibration procedure.

At a certain radiometer housing temperature, T_c , regulated by the temperature of alcohol flowing through tubes in thermal contact with the radiometer housing in the vacuum chamber, liquid nitrogen at -196°C was pumped through the tubes in one target while the temperature of the nitrogen flowing through tubes in the other target was varied from -196°C to about $+30^\circ\text{C}$.

This procedure was carried out at eight different radiometer housing temperatures (0° , 7° , 12° , 18° , 23.5° , 30° , 37° and 45°C) while viewing the warm target respectively through the wall and floor sides of the radiometer. The temperatures of each target were recorded by means of thermocouples. Using the formula

$$D = \frac{127}{50} F \quad (8)$$

shown schematically in Fig. 10(d), a curve of T_{BB} vs. D was constructed for each channel on both wall and floor sides, at varying values of T_c (Figs. 17-28 and 35-40). If the quantity \bar{W} is desired, it may be determined from the \bar{W} vs. T_{BB} graphs for each channel. (Figs. 7, 8 and 9). The complete calibration is shown schematically in Fig. 47(a).

2.6.2 Visible Channels 3 and 5. A tungsten filament lamp calibrated by the Bureau of Standards was used in the calibration procedure. Radiation from the lamp was diffusely reflected from a sheet of white paper of known spectral reflectivity. The output signal of each channel was read with the illuminated paper normal to rays from the lamp and completely filling one field of view of the radiometer. The other field of view was covered with black tape. In order to obtain more than one point per calibration, the white paper was placed at different distances from the tungsten filament source lamp. The effective radiant emittance was computed using:

$$\bar{W} = \frac{\cos \gamma}{R^2} \int_0^\infty J_\lambda r_\lambda \phi_\lambda d_\lambda \quad (9)$$

A curve of \bar{W} vs. voltage, V , was then constructed, with T_c being the ambient temperature of the room in which the calibration was made. In order to construct \bar{W} vs. F_{sc} curves at various values of T_c , it was necessary to make additional measurements in vacuum where T_c could be controlled. Two targets consisting of diffusers illuminated by light bulbs, one target for each of the wall and floor sides, were used for both channels in this calibration. The voltages could be regulated. A certain range of voltages was selected and measurements of the various values of T_c were made of each voltage, recording corresponding radiometer voltage and output frequency at each level. Measurements were made by illuminating

alternately both wall and floor sides, keeping the lights off on the side that was to simulate space viewing. In order to correlate the vacuum measurements with the tungsten-filament lamp source measurements, it was necessary to make one set of vacuum measurements at the same T_c that existed for the air measurements. By relating bulb voltage levels to \bar{W} at the air measurement T_c , \bar{W} vs. F_{sc} curves were constructed for the same eight T_c values as used in the thermal channels (Figs. 29-34 and 41-46). A comparison calibration was made using rays from the mid-day sun as the visible light source, and the results agreed well within 5% of the tungsten lamp calibration.

In order to calculate the reflectance (loosely "albedo") of a spot on earth viewed by the radiometer, one must know \bar{W}^* , the particular value of \bar{W} which would be measured if the spot viewed were a perfectly diffuse reflector having unit reflectivity and illuminated by solar radiation at normal incidence. Using eq. (9) for this calculation, and setting $\gamma = 0^\circ$, $R = 1$ astronomical unit, $r_\lambda = 1$, and $J_\lambda = (\bar{W}_\lambda(T) \times \text{Cross-sectional Area of Sun}) / \pi$, we have

$$\bar{W}^* = \frac{\Omega}{\pi} \int_0^\infty W_\lambda(T) \phi_\lambda d_\lambda \quad (10)$$

Calculations of \bar{W}^* were made taking the sun as a 5800°K blackbody for channel 3 and as a 6000°K blackbody for channel 5. The complete calibration is shown schematically in Fig. 47(b).

2.7 Summary of the Calibration

When a certain value of effective radiant emittance \bar{W} or equivalent blackbody temperature T_{BB} is viewed by the radiometer through a given side with a given radiometer housing temperature whose value lies within 5.5°C of the electronics temperature T_e (under which conditions the variability with temperature of the voltage-frequency transfer in the oscillator introduces a negligible error compared to the system inaccuracy of the experiment) an output signal F_{sc} results. This is shown diagrammatically in Figs. 10(b) and 10(c).

The calibration for each side of each channel is carried out for eight parametric values of T_c ; hence, it is necessary to interpolate between the two transfer functions bracketing an actual value of T_c to arrive at the calibration for a given orbital period.

III. DATA PROCESSING

3.1 Information Flow in the Satellite

The radiation experiment instrumentation is independent of the television camera system except for power, command, certain timing signals

and antennas (Fig. 48).¹ The output of the five medium resolution radiometer channels is fed into five subcarrier oscillators. These voltage controlled oscillators are of the phase shift type with symmetric amplifiers in the feedback loops, the gains of which are controlled by the balanced input signal. A sixth channel is provided for telemetry of the wide angle low resolution sensor data, the University of Wisconsin's heat balance data, environmental temperatures, instrumentation canister pressure, and calibration. A mechanical commutator switches resistive sensors in one branch of a phase shift oscillator. The seventh channel, a tuning fork oscillator, serves as a reference frequency and timing signal. The outputs from these seven different channels are summed and the resultant composite signal equalized in a record amplifier which drives the head of a miniature tape recorder. An oscillator provides an alternating current bias to the record head and the signal required for the erase head. For convenience, erase of the magnetic tape occurs immediately before recording. The record spectrum extends from 100 cps to 550 cps. The tape recorder is an endless-loop, two-speed design running at 0.4 ips record and 12 ips playback speed. The endless loop records continuously, day and night, except during a playback sequence. A hysteresis synchronous motor generates torque in the record mode through a mylar belt speed reduction. The fourth subharmonic of the tuning fork oscillator, generated by flip flops, drives a cam shaft which activates a bank of micro switches connected to the five commutated sub-channels of the time-sharing sixth channel. Each is sampled six seconds and the fifth includes a group of seven to be sub-commutated.

Playback is initiated upon command by applying power to a direct current motor. A magnetized flywheel generates a frequency proportional to the motor speed. A frequency discriminator feeds the error signal to the stabilized power supply of the motor and closes the servo loop. Playback speed is essentially constant from 0° to 50° C. A low flutter and wow of 2.5% peak-to-peak measured without frequency limitations is achieved by using precision bearings and ground-in-place shafts having tolerances of better than 50 parts per million. A command pulse activates the playback motor, the playback amplifier, and the 238 Mc FM telemetry transmitter feeding the duplexer and antenna.

In order to permit comparison of the low resolution measurements with TV pictures, each TV shutter action generates a 1.5 second pulse which is recorded as an amplitude modulation of the channel seven timing signal. There are nine solar cells mounted behind narrow slits for north angle determination. These slits have an opening angle of close to 180° in planes through the spin axis. The sun illumination generates pulses as long as

illumination parallel to the spin axis is avoided. One of these sensors generates a 0.5 second pulse in addition to the north indicator code so that spin rate information and a measure of relative sun position is available. Again, this pulse is recorded as an amplitude modulation of channel seven. Reconstruction of the radiation information vitally depends on its correlation with absolute time. An accurate but relative timing signal is provided by the tuning fork oscillator and a crude one by the sun pulses except when the satellite is in the earth's umbra. Absolute time is transmitted to the satellite and recorded on the tape as a one-second dropout of channel seven. The occurrence of this pulse is known within milliseconds of absolute time.

3.2 *Information Flow at the Command and Data Acquisition Station*

Upon interrogation, the 238 Mc carrier is received by a 60-foot parabolic antenna, and the composite signal is recorded on magnetic tape and, simultaneously, fed to a "Quick-Look" demodulator (Fig. 49(a)).¹¹ At the same time, the envelope of channel 7 and the clipped signal of channel 4 are graphically recorded. The 8-30 micron "events" on the graphic record show alternately the earth and sky scan intervals as the satellite spins and progresses along the orbit, and the channel 7 envelope shows the three distinctive types of AM pulses impressed on the clock frequency during the record; namely, the sun sensor pulses, the TV camera pulses, and the "end-of-tape" pulse. Auxiliary uses of the radiation data include determination of the spin axis attitude in space and the times when television pictures were taken and recorded in the satellite, to be read out later over a ground station (Figs. 49(b) and 49(c)).

The magnetic tapes are routinely mailed every day to the Aeronomy and Meteorology Division, GSFC, in Greenbelt, Maryland. The master tape containing the composite radiation signal is demultiplexed, demodulated, and fed into an analog-to-digital converter (Fig. 50). The pressure is read separately. The analog-to-digital converter produces a magnetic "Radiation Data Tape" made up of 36 bit words suitable for an IBM 7090 computer.

3.3 *Information Flow at the Data Reduction Center*

The IBM 7090 computer program requires inputs from three sources to produce the "Final Meteorological Radiation (FMR) Tape." One source is the Radiation Data Tape containing radiation data and satellite environmental parameters in digital form. Another source is the calibration for converting digital information to meaningful physical units. The third source is the "Orbital Tape" from the NASA Space Computing Center containing satellite position and attitude data. The FMR Tape (in binary form) then is

the basic repository of data from the medium resolution scanning radiometer. In order to study and utilize the scanning radiometer data, appropriate computer programs must be written to "talk" to the Final Meteorological Radiation Tape and provide for printing out data, punching cards, or producing maps. The make-up of the IBM 7090 computer program and the format of the Meteorological Radiation Tape are discussed in detail in Sections IV and V.

IV. FORMAT OF THE FINAL METEOROLOGICAL RADIATION TAPE (BINARY)

TIROS III radiation data will be available on low density, binary tapes prepared on an IBM 7090 computer. The FMR Tape is the product of a computer program whose input is the orbital data, digitized radiation data, and TIROS III radiometer calibration package. In addition to the calibrated radiation measurements, the final meteorological radiation tape also contains geographical locations associated with the radiation measurements, orbital data, solar ephemeris, and satellite temperature. The exact format of these data is described below, and the purpose of this section is to emphasize certain features that will aid programmers in utilizing these data.

Each orbit of radiation data is treated as a file which contains a documentation record plus data records that represent approximately one minute intervals of time. The documentation record is the first record of each file and contains 14 data words whose format is described below. Dref was defined as the number of days between zero hour of September 1, 1957, and zero hour of launch date. Julian time counts zero time as zero hour at Greenwich on the day of launch, thus launch time is given in GMT and launch day is zero day, with succeeding days numbered sequentially. However, if the satellite life extends beyond about 100 days, the value of dref is redefined by adding approximately 100, while the Julian day is decreased by the same amount.

Each record of data covers approximately one minute of time, and the data are found in the decrement (D) and address (A) of each data word. The record terminates with the end of swath in progress at 60.0 seconds past the minute specified in words 1D, 1A, and 2D. In the case of satellite-earth orientation such that the radiometer continuously scans the earth for more than one rotation of the satellite, the record will terminate with the end of the revolution in progress at 60.0 seconds past the minute specified in words 1D, 1A, and 2D. The End of File gap will be duplicated at the end of the last file on each Final Meteorological Radiation Tape.

For each earth viewing swath, the radiation measured from Channel 1 ($6.0 - 6.5\mu$), Channel 2 ($8 - 12\mu$) and Channel 4 ($8 - 30\mu$) is reported as the equivalent blackbody temperature, while the radiation measured from Channel 3 ($0.2 - 6.0\mu$) and Channel 5 ($0.55 - 0.75\mu$) is reported in watts/meter². For each fifth measurement in a swath, the point on earth being "viewed" by the radiometer is defined in terms of latitude and longitude. These computations are based on the best available estimate of satellite attitude.

In order that the user may distinguish between data from the wall and floor sides of the satellite, the data words containing the measured energy are labeled with a 1 in position 19 when the wall side of the satellite is viewing the earth. The user should realize that if the signal from the satellite becomes noisy, swath sizes are abnormal, and the data can be labeled and located incorrectly. In order to flag abnormal data, minus signs are inserted for the following three reasons:

1. A measurement within a swath whose digital response falls below the arbitrarily defined threshold between earth and space. (The end of a swath is arbitrarily defined by three consecutive measurements falling below the threshold.)
2. An entire swath is labeled with minus signs when the observed swath size falls outside of the theoretical swath size $\pm 25\%$. The theoretically computed swath size is based on the best available estimate of satellite attitude, height, and spin rate.
3. The entire swath is labeled with minus signs when this swath is the last swath in the closed mode where the radiometer has been continuously scanning the earth for more than one spin revolution.

At the end of each earth viewing swath, two additional data words contain the end of swath code, the minimum nadir angle of the radiometer optical axis occurring in this swath, and the latitude and longitude of the point on earth being "viewed" by the radiometer when the minimum nadir angle occurred.

The block of data from words 6D to 24A will be repeated, thus defining every fifth measurement in a swath. The address of the third word in the last response of a swath will contain 010101010101010 to signal end of record. A "look ahead" feature has been incorporated into TIROS III data reduction, and if the End of Tape signal occurs within an earth-viewing swath, that entire swath is discarded.

Occasionally, dropouts are encountered and the corresponding data records contain no radiation data. This event is relatively rare in TIROS III data, but in such cases the radiation data record contains only five words (1D to 5A) which document the record with respect to time. In such records, the datum in the address of the third word (T_c) is destroyed by the End of Record Code.

FORMAT OF FINAL METEOROLOGICAL RADIATION TAPE

Documentation Record

Word No.	Quantity	Units	Scaling	Remarks
1	Dref.		B = 35	Number of days between zero hour of Sept. 1, 1957, and zero hour of launch day.
2	Date			Date of Interrogation expressed as a packed word, i.e., July 12, 1961 would be (071261) ₁₀ or (071475) ₁₀ . These numbers are shifted to extreme right side of the data word.
3	Day	Julian Day	B = 35	Start time of this file of radiation data.
4	Hour	Z Hour	B = 35	
5	Minute	Z Minute	B = 35	
6	Seconds	Z Seconds	B = 26	
7	Day	Julian Day	B = 35	Time of Interrogation, i.e., end time of this file of radiation data.
8	Hour	Z Hour	B = 35	
9	Minute	Z Minute	B = 35	
10	Seconds	Z Seconds	B = 26	
11	Satellite Spin Rate	Deg./Sec.	B = 26	Satellite spin rate (accuracy about 0.01 deg/sec)
12	Frequency	36, 72, 144	B = 35	Data sampling frequency (cycles of a 550 cps tuning fork)
13	Orbit No.		B = 35	Orbit No. at time of Interrogation
14	Station Code		B = 35	Code defining ground station ("1" for Wallops Island, Va., "2" San Nicholas Island, Calif.)

Format of FMR TAPE—Nth Record

1D	Day		B = 17	Julian Day
1A	Hour		B = 35	Z time in day specified in word 1D
2D	Minute		B = 17	
2A	GHA	Degrees	B = 29	Greenwich hour angle and declination of sun at time specified in words 1D, 1A, and 2D. 90° are added to declination to yield positive numbers.
3D	Decl.	Degrees	B = 11	
3A	T _C	Degrees K	B = 35	Reference temperature of the medium resolution radiometer.
4D	T _E	Degrees K	B = 17	Reference temperature of maindeck electronics.
4A	Height	Kilometers	B = 35	Height of satellite at time specified in words 1D, 1A, and 2D.
5D	Latitude	Degrees	B = 11	Latitude of subsatellite point at time specified in words 1D, 1A, 2D. 90° are added to all latitudes to yield positive numbers.
5A	Longitude	Degrees	B = 29	Longitude of subsatellite point at time specified in words 1D, 1A, 2D. Longitudes are reported as 0 to 360°, with west being positive.
6D	Seconds		B = 8	Seconds past time specified in words 1D, 1A, 2D when first earth viewing response is detected, and every fifth response thereafter.
6A	Latitude	Degrees	B = 29	Latitude of subsatellite point at time specified in words 1D, 1A, 2D, 6D. 90° are added to all latitudes to yield positive numbers.
7D	Longitude	Degrees	B = 11	Longitude of subsatellite point at time specified in words 1D, 1A, 2D, 6D. Longitudes are reported as 0 to 360°, with west being positive.
7A	Latitude	Degrees	B = 29	Latitude of point on earth being "viewed" by radiometer at time specified in words 1D, 1A, 2D, 6D. 90° are added to all latitudes to yield positive numbers.
8D	Longitude	Degrees	B = 11	Longitude of point on earth being "viewed" by radiometer at time specified in words 1D, 1A, 2D, 6D. Longitudes are reported as 0 to 360°, with west being positive.
8A	Nadir Angle	Degrees	B = 29	Nadir angle of optic axis from radiometer to point specified in words 7A, 8D.
9D	Azimuth Angle	Degrees	B = 11	Azimuth angle of optic axis from radiometer to point specified in word 7A, 8D. This angle is measured clockwise and expressed as a positive number.
9A	Zero			
10D	T _{BB} (ch. 1)	Degrees K	B = 14	Measurement by each of the five medium resolution channels at time specified in 1D, 1A, 2D, 6D when radiometer is "viewing" point on earth specified in words 7A, 8D.
10A	T _{BB} (ch. 2)	Degrees K	B = 32	
11D	W (ch. 3)	Watts/m ²	B = 14	
11A	T _{BB} (ch. 4)	Degrees K	B = 32	
12D	W (ch. 5)	Watts/m ²	B = 14	
12A	Zero			
13D	T _{BB} (ch. 1)	Degrees K	B = 14	The data sample immediately following the measurement recorded in words 10D-12A.
13A	T _{BB} (ch. 2)	Degrees K	B = 32	
14D	W (ch. 3)	Watts/m ²	B = 14	
14A	T _{BB} (ch. 4)	Degrees K	B = 32	
15D	W (ch. 5)	Watts/m ²	B = 14	
15A	Zero			
16D	T _{BB} (ch. 1)	Degrees K	B = 14	The data sample immediately following the measurement recorded in words 13D-15A.
16A	T _{BB} (ch. 2)	Degrees K	B = 32	
17D	W (ch. 3)	Watts/m ²	B = 14	
17A	T _{BB} (ch. 4)	Degrees K	B = 32	
18D	W (ch. 5)	Watts/m ²	B = 14	
18A	Zero			
19D	T _{BB} (ch. 1)	Degrees K	B = 14	The data sample immediately following the measurement recorded in words 16D-18A.
19A	T _{BB} (ch. 2)	Degrees K	B = 32	
20D	W (ch. 3)	Watts/m ²	B = 14	
20A	T _{BB} (ch. 4)	Degrees K	B = 32	
21D	W (ch. 5)	Watts/m ²	B = 14	
21A	Zero			
22D	T _{BB} (ch. 1)	Degrees K	B = 14	The data sample immediately following the measurement recorded in words 19D-21A.
22A	T _{BB} (ch. 2)	Degrees K	B = 32	
23D	W (ch. 3)	Watts/m ²	B = 14	
23A	T _{BB} (ch. 4)	Degrees K	B = 32	
24D	W (ch. 5)	Watts/m ²	B = 14	
24A	Zero			

The block of data from words 6D to 24A will be repeated, thus defining every fifth point in a swath. The address of the third word in the last response of the last swath of each record will contain 010101010101010 to signal the end of record. Each time the swath terminates, two words (N and N+1) will follow the last "earth viewing" response with the following format:

Word No.	Quantity	Units	Scaling	Remarks
ND.....	Code.....	11111111111111		Code indicating end of swath.
NA.....	Nadir Angle.....	Degrees.....	B = 29	The minimum nadir angle that occurred in the previously defined swath
(N+1)D.....	Latitude.....	Degrees.....	B = 11	Latitude of point on earth being "viewed" by radiometer when the minimum nadir angle occurred. 90° are added to all latitudes to yield positive numbers.
(N+1)A.....	Longitude.....	Degrees.....	B = 29	Longitude of point on earth being "viewed" by radiometer when minimum nadir angle occurred. Longitudes are reported as 0 to 360°, with west being positive.

The End-of-File code word appearing on TIROS II FMR Tapes has been omitted from the TIROS III FMR Tapes. A look-ahead feature was incorporated such that the last record terminates with the end of the last swath prior to the EOT signal. A flow diagram to aid in interpreting this Format is shown in Fig. 51. It is seen that the Format is analogous to four "nested loops" (in programming language), i.e., groups of five responses, entire swaths, one-minute records, and files. It is pointed out that a particular swath (and, hence, a particular record and a particular file) can end either on the "anchor data response" or on any of the four following non-geographically located data responses and that Fig. 51 merely illustrates one possible combination of ending responses.

V. IBM 7090 COMPUTER FLOW DIAGRAM

The Final Meteorological Radiation Tape, described in the previous section, is prepared with an IBM 7090 computer program whose input consists of orbital data, digital radiation data, and TIROS III radiometer calibration package. The flow chart shown in Fig. 52 outlines the logical steps in this program and thus gives some insight into the mechanics of preparing these tapes. The flow chart has been greatly condensed since it is impossible to present a detailed flow chart within the space limitations of this publication.

The first phase of this program sets up the documentation data and then reads the entire file of radiation data to compute the start time from the end-of-tape time and the data sampling frequency. Given the starting and ending times, the program then searches the orbital tape to find orbital data (subsattellite point, height, nadir angle, right ascension, and declination) covering the same time interval. These data are then arranged in tables as a function of time so that interpolation subroutines can be used in the second phase to obtain values of the orbital characteristics for any specified time.

At this point, an optional feature allows the program to accept the attitude data from the orbital tape, or an alternate estimate of the attitude from a second documentation card. If the alternate attitude is accepted, the nadir angles are recomputed.

The second phase of the program reduces the digitized radiation data into useful meteorological data. This begins with a detailed examination of

the radiation data to distinguish between earth and space viewed data. This distinction is based on an arbitrarily defined threshold value applied to channel 2. Both sensors are assumed to be viewing space when the measured radiation falls below the threshold value, and one sensor is viewing the earth when the measured radiation exceeds the threshold value. The end of swath is arbitrarily defined as three consecutive space-viewed measurements.

For each earth-viewing swath, the program proceeds to determine which sensor is viewing the earth, computes the latitude and longitude of the point on earth being "viewed" by the radiometer for each fifth measurement in the swath; and converts the digitized data into radiation units for each measurement in the swath. The data words containing radiation measurements contain a 1 in position 19 when the wall sensor is viewing the earth.

Each record on the final meteorological radiation tape covers approximately one minute of time and terminates with the end of swath in progress at 60.0 seconds past the minute. When the end of tape is encountered, the program writes the last data record and reinitializes in preparation for the next orbit of radiation data.

VI. PRE-LAUNCH AND POST-LAUNCH OBSERVATIONS AND DEVELOPMENTS

6.1 Pre-Launch Degradation of Channels 3 and 5

Between the original calibration and the launch of the satellite, several "check-of-calibration"

measurements of all channels were made. There is evidence from these measurements that channel 3 suffered a progressive decrease in sensitivity.

On the other hand, the check-of-calibration data *do not* indicate a similar decrease in the sensitivity of channel 5 before launch (although such data for another radiometer which was exposed to ambient conditions for several months following its original calibration did show a progressive sensitivity decrease for channel 5 as well as for channel 3).

It was not felt that the check-of-calibration data were of sufficient quantity to justify revising completely the original calibration of channel 3 (or channel 5). Hence, the original calibration is shown in this Manual and will be used to produce the FMR Tapes. Evidence of the differential pre-launch sensitivity decrease of channel 3 over channel 5, however, can be seen in the early-orbit values of $(W_5 \cdot W_3^*) / (W_3 \cdot W_5^*)$ discussed in paragraph 6.2.

Tests are under way in the laboratory attempting to determine the cause of the observed pre-launch decrease in sensitivity of the solar channels, but, as of this writing, no conclusive results are available.

6.2 Post-Launch Degradation of Channels 1, 2, 4 and 5

From about orbit 118 on, channel 1 displayed an extremely high space-viewed level with the signal initially going in a negative sense from this level followed by a reversal to the positive sense when the wall optic scanned the earth. The signal remained always positive with respect to the space-viewed level when the floor side scanned the earth. This degradation pattern became more pronounced with increasing time in the life of the satellite. From about orbit 130 on, channel 4 displayed the same form of degradation, and from about orbit 875 on, channel 2 also degraded steadily. Histories of the differences between the original calibration space-viewed levels and the space-viewed levels telemetered while in orbit are shown in Figs. 53 through 55 for the three thermal channels.

The ratio of (W/W^*) measured by channel 5 to (W/W^*) measured by channel 3, viz. $(W_5 \cdot W_3^*) / (W_3 \cdot W_5^*)$, when viewing the same scan spot on earth, yields a comparison of reflectance of solar radiation as measured by the two solar channels. Theoretically, the two reflectance measurements should be substantially the same. A history of the ratio $(W_5 \cdot W_3^*) / (W_3 \cdot W_5^*)$ calculated from many measurements during the life of TIROS III is shown in Fig. 56. It is seen that in the early orbits the ratio is greater than the expected value of unity. The pre-launch decrease in sensitivity discussed in paragraph 6.1 could account for this difference. It is further seen that, although the scatter among the individual data points is large,

there is a progressive decrease in the ratio throughout the entire life of the satellite. That this was indeed a decrease in sensitivity of channel 5 (and not an increase in sensitivity of channel 3) was evidenced by the general decrease over many days of the maximum channel 5 signals observed visually on analog records of a large number of orbits. However, it is difficult to assign absolute values to the channel 5 degradation because it is not known what changes, if any, channel 3 was undergoing at the same time. Only when the FMR Tapes are available can absolute values possibly be determined by means of long-term broad-scale statistical averages using computer techniques.

An investigation of the degradation problem that has occurred in similar ways in both TIROS II and TIROS III continues, but as of this printing, no definite conclusions as to its cause have been reached. Furthermore, the analysis of such a situation turns out to be rather complex, and no satisfactory model has been found which would lead to a possible method of correcting the flight data for this effect.

6.3 Estimate of the Accuracy of the Data

Inaccuracies in the data are caused by such effects as wow and flutter in the magnetic tape, noise, drift of T_E from T_C , uncertainties in the original calibration (due to such effects as assuming that the spectral absorptivity of the bolometers is flat over all wavelengths), and, of course, loss of sensitivity and degradation of the various channels after the original calibration.

The estimates of accuracy given below apply to the mid-range of target intensities. As can be seen from the figures of F_{SC} vs. T_{BB} , the accuracy of the thermal channels suffers at very low target temperatures.

Channel 1

The estimated relative accuracy of T_{BB} measurements is $\pm 2^\circ\text{K}$ and the estimated absolute accuracy is $\pm 5^\circ\text{K}$ up to orbit 118, after which degradation becomes appreciable.

Channel 2

The estimated relative accuracy of T_{BB} measurements is $\pm 2^\circ\text{K}$ and the estimated absolute accuracy is $\pm 4^\circ\text{K}$ up to orbit 875, after which degradation becomes appreciable.

Channel 3

The estimated relative accuracy of \bar{W} measurements is $\pm 20 \text{ w/m}^2$. Because of the pre-launch decrease in sensitivity described in paragraph 6.1 and because the mechanism causing the post-launch progressive change in the ratio of solar channel measurements is not fully understood, no estimates of absolute accuracy are given.

Channel 4

The estimated relative accuracy of T_{BB} measure-

ments is $\pm 2^\circ\text{K}$ and the estimated absolute accuracy is $\pm 4^\circ\text{K}$ up to orbit 130, after which degradation becomes appreciable.

Channel 5

The estimated relative accuracy of W measurements is $\pm 3\ w/m^2$. Because the mechanism causing the post-launch progressive change in the ratio of solar channel measurements is not fully understood, estimates of absolute accuracy are not given, except that *immediately* after launch it is estimated that the absolute accuracy was $\pm 10\ w/m^2$.

VII. CONCLUSIONS

The greatest uncertainty in the radiation measurements is due to the apparent shift in the zero radiation level. The error introduced by not correcting for this effect is probably largest at low equivalent blackbody temperatures, becoming smaller with increasing temperature. The significance of the data is doubtful beyond orbit 118 for channel 1, orbit 130 for channel 4, and orbit 875 for channel 2, due to the degradations which developed in the outputs of these channels after launch.

The absolute measurements by channel 5 immediately after launch are probably valid within $\pm 10\ w/m^2$. Otherwise, because of the as yet unexplained degradation mechanisms which operated both before and after the satellite went into orbit, the absolute measurements from the two solar channels are probably low. However, the relative measurements from the solar channels are still valid for such purposes as the contrast mapping of cloud systems.

VIII. REFERENCES AND BIBLIOGRAPHY

1. Bandeen, W. R., R. A. Hanel, John Licht, R. A. Stampf, and W. G. Stroud: "Infrared and Reflected Solar Radiation Measurements from the TIROS II Meteorological Satellite." *J. of Geophys. Res.*, **66**, 3169-3185, October 1961.
2. Hanel, R. A., and W. G. Stroud: "Infrared Imaging from Satellites." *J. of the SMPTE*, **69**, 25-26, January 1960.
3. Sternberg, Sidney and William G. Stroud: "TIROS I: Meteorological Satellite" *Astronautics*, **5**, 32-34 and 84-86, June 1960.
4. Stroud, W. G.: "Initial Results of the TIROS I Meteorological Satellite." *J. of Geophys. Res.*, **65**, 1643-1644, May 1960.
5. Bandeen, William R. and Warren P. Manger: "Angular Motion of the TIROS I Meteorological Satellite due to Magnetic and Gravitational Torques" *J. of Geophys. Res.*, **65**, 2992-2995, September 1960.
6. Doolittle, R. C., L. Miller and I. Ruff: "Geographic Locations of Cloud Features" Appendix A of "Final Report on the TIROS I Meteorological Satellite System," Part II by Staff, Meteorological Satellite Laboratory, U. S. Weather Bureau, in *NASA Technical Report R-131*, 1962.
7. Bristor, C. L., E. G. Albert, and J. B. Jones: "Problems in Mapping Data from Meteorological Satellites" *Space Research II, Proceedings of the Second International Space Science Symposium, Florence, Italy, April 10-14, 1961*, North-Holland Publishing Company, Holland.
8. Hubert, L. F.: "TIROS I: Camera Attitude Data, Analysis of Location Errors, and Deviation of Correction for Calibration" *MSL Report No. 5* to NASA.
9. Dean, C.: "Attitude Determination from Picture Data," "TIROS I: An Operational Evaluation of a New Meteorological Tool," *Second Semi-Annual Technical Summary Report*, Contract AF 19 (604), 5581, Allied Research Associates, Inc. June 30, 1960.
10. Ballard, S. S., K. A. McCarthy, and W. L. Wolfe: *State-of-the-Art Report Optical Material for Infrared Instrumentation*, Report Number 2389-11-S, University of Michigan Willow Run Laboratories, Ann Arbor, Michigan. January 1959. (Unclassified).
11. Davis, J., R. Hanel, R. Stampf, M. Strange, and M. Townsend, "Telemetering IR Data from the TIROS II Meteorological Satellite" *NASA Technical Note D-1293*.
12. Astheimer, R. W., R. DeWaard, and E. A. Jackson: "Infrared Radiometric Instrumentation on TIROS II." *J. Optical Soc. Amer.*, **51**, 1386-1393, December 1961.
13. Conrath, Barney J. "Earth Scan Analog Signal Relationships in the TIROS Radiation Experiment and Their Application to the Problem of Horizon Sensing." *NASA Technical Note D-1341*.
14. Fritz, Sigmund and Jay S. Winston: "Synoptic Use of Radiation Measurements from Satellite TIROS II." *Monthly Weather Review*, **90**, 1-9, January 1962.
15. Greenfield, S. M. and W. W. Kellogg: "Calculations of Atmospheric Infrared Radiation as seen from a Meteorological Satellite." *J. of Meteor.*, **17**, 283-289, June 1960.
16. Hanel, R. A. and D. Q. Wark: "TIROS II Radiation Experiment and Its Physical Significance." *J. Opt. Soc. Am.*, **51**, 1394-1399, December 1961.
17. Nordberg, W., W. R. Bandeen, B. J. Conrath, V. Kunde and I. Persano: "Preliminary Results of Radiation Measurements from the TIROS II Meteorological Satellite." *J. of the Atmos. Sciences*, **19**, 20-30, January 1962.
18. Wark, D. Q.: "On Indirect Temperature Soundings of the Stratosphere from Satellites." *J. of Geophys. Research*, **66**, 77-82, January 1961.
19. Wark, D. Q., G. Yamamoto and J. H. Lienesch: "Methods of Estimating Infrared Flux and Surface Temperatures from Meteorological Satellites." (To be published in the *J. of the Atmos. Sciences*.)
20. Wexler, R.: "Satellite Observations of Infrared Radiation." *First Semi-Annual Technical Summary Report*. (Allied Research Assoc., Inc., Boston, Mass.), Contract No. AF19-(604)-5968, ARCRC. December 24, 1959.

TABLE II—Filter and lens materials

	Channel 1	Channel 2	Channel 3	Channel 4	Channel 5
Lens 1	Germanium immersion lens detector, first surface coated with pure ZnS of $\lambda/4$ optical thickness at 6.3μ .	Germanium with both surfaces coated with pure ZnS of $\lambda/4$ optical thickness at 10μ .	Synthetic Barium Fluoride (BaF_2) with no coatings.	KRS-5 (Thallium-bromo-iodide) with no coatings. ¹⁰	Pure quartz (SiO_2) with no coatings.
Lens 2	Germanium with both surfaces coated with pure ZnS of $\lambda/4$ optical thickness at 6.3μ .	Germanium with both surfaces coated with pure ZnS of $\lambda/4$ optical thickness at 10μ .	Synthetic Sapphire (Al_2O_3) with no coatings.	None	Synthetic Sapphire (Al_2O_3) with no coatings.
Lens 3	Germanium with both surfaces coated with pure ZnS of $\lambda/4$ optical thickness at 6.3μ .	None	None	None	None
Filter 1	Narrow band, OCLI, interference type centered at 6.3μ with 14 multilayers, both surfaces of Al_2O_3 substrate and alternate films of Ge and SiO .	Indium Antimonide (InSb), both surfaces coated with pure ZnS of $\lambda/4$ optical thickness at 10μ .	None	Indium Antimonide (InSb) coated with pure ZnS, one surface with $\lambda/4$ optical thickness at 13μ and other at 20μ .	Narrow band Infrared Industries Type 259,011,513.
Filter 2	None	Arsenic Trisulfide (As_2S_3) glass, uncoated 0.5 mm plane piece. ¹⁰	None	None	Narrow band Infrared Industries Type 259,011,608.
Filter 3	None	None	None	None	Infrared Industries chance glass ON-20 1/8 inch thick.

TABLE III—Effective spectral response, Channel 1

λ (Microns)	ϕ_λ
5.7	0
5.8	.005
5.9	.028
6.0	.101
6.1	.187
6.2	.251
6.3	.267
6.4	.283
6.5	.291
6.6	.105
6.7	.035
6.8	.011
6.9	.005
7.0	0

TABLE V.—Effective spectral response, channel 3

λ (Microns)	ϕ_λ	λ (Microns)	ϕ_λ
.25	.138	2.81	.700
.26	.233	3.02	.699
.28	.366	3.50	.738
.31	.474	4.10	.722
.41	.604	4.22	.688
.51	.638	4.34	.714
.61	.571	4.45	.702
.71	.508	4.58	.693
.81	.430	4.70	.666
.91	.461	4.82	.632
1.01	.515	4.94	.597
1.21	.596	5.06	.558
1.41	.620	5.30	.456
1.61	.645	5.66	.304
1.81	.663	6.14	.085
1.91	.677	6.26	.058
2.01	.686	6.40	.042
2.21	.697	6.60	.026
2.41	.700	6.80	.010
2.61	.707	6.82	0

TABLE IV.—Effective spectral response, channel 2

λ (Microns)	ϕ_λ	λ (Microns)	ϕ_λ
7.07	.0	13.33	.106
7.41	.058	13.79	.036
7.69	.168	14.28	.008
8.00	.284	14.81	.009
8.33	.338	15.38	.024
8.70	.405	16.00	.088
9.09	.464	16.67	.099
9.52	.487	17.39	.081
10.00	.473	18.18	.057
10.53	.473	19.05	.040
11.11	.430	20.00	.024
11.76	.358	21.05	.012
12.50	.267	22.22	.003
12.90	.201	25.00	0

TABLE VI.—Effective spectral response, channel 4

λ (Microns)	ϕ_λ	λ (Microns)	ϕ_λ	λ (Microns)	ϕ_λ
7.4	0	16.6	.610	26.8	.320
7.6	.046	17.0	.600	27.2	.300
8.0	.268	17.2	.587	27.6	.277
8.6	.361	18.0	.566	27.8	.233
8.8	.388	19.0	.537	28.0	.195
9.2	.425	19.2	.530	28.4	.200
9.8	.455	20.0	.521	28.8	.190
10.2	.477	21.0	.485	29.0	.179
11.2	.523	22.0	.439	29.4	.178
12.0	.544	23.0	.402	29.8	.162
12.8	.559	24.0	.358	30.0	.151
13.6	.584	24.2	.349	30.4	.141
14.0	.583	25.0	.351	31.2	.100
14.4	.644	25.4	.362	32.0	.056
15.4	.625	26.2	.354	32.4	.021
16.2	.614	26.4	.350	32.6	0

TABLE VII.—Effective spectral response, channel 5

λ (Microns)	ϕ_λ	λ (Microns)	ϕ_λ
.475	0	.800	0
.500	.021	1.100	.002
.525	.106	1.130	.011
.550	.287	1.200	.006
.575	.284	1.400	.010
.600	.200	1.600	.029
.625	.223	1.800	.050
.650	.266	2.000	.052
.675	.256	2.200	.051
.700	.174	2.400	.056
.725	.190	2.600	.063
.750	.095	2.700	.067
.775	.009	2.800	.005
		2.900	0

TABLE IX— T_{BB} vs. \bar{W} , Channel 2

T_{BB} (°K)	\bar{W} (watts/m ²)
170	2.48
190	5.33
210	10.10
230	17.37
250	27.65
270	41.38
290	58.89
310	80.41
330	106.07
350	135.94
370	170.00

TABLE VIII— T_{BB} vs. \bar{W} , Channel 1

T_{BB} (°K)	\bar{W} (watts/m ²)
180	0.018
199	0.061
218	0.164
237	0.377
256	0.769
275	1.419
294	2.422
313	3.876
332	5.878
351	8.524
370	11.902

TABLE X T_{BB} vs. \bar{W} , Channel 4

T_{BB} (°K)	\bar{W} (watts/m ²)
170	14.55
190	25.15
210	40.01
230	59.66
250	84.50
270	114.77
290	150.57
310	191.93
330	238.76
350	290.92
370	348.22

TABLE XI.—Changes in Blackbody Temperature and Effective Radiant Emittance Due to Differences of T_C From T_E

Channel	T_E (°C)	T_C (°C)	Side	F_{SC} (cps)	T_{BB} (°K)	ΔT_{BB}	\bar{W} (w/m ²)	\bar{W}/\bar{W}^*	$\Delta(\bar{W}/\bar{W}^*)$
1	0	0	Floor	130	247.5	0			
	5	0		130.2	248.0	0.5			
	5	5		130.2	245.5	0			
	0	5	Wall	130	245.0	0.5			
	5	0		130	254.3	0			
	5	0		130.2	254.8	0.5			
	5	5		130.2	246.1	0			
	5	5		130	245.5	0.6			
						0.52			
2	0	0	Floor	185	235.5	0			
	5	0		185.3	236.3	0.8			
	5	5		185.3	233.1	0			
	0	5	Wall	185	232.4	0.7			
	0	0		185	239.2	0			
	5	0		185.3	240.0	0.8			
	5	5		185.3	234.8	0			
	5	5		185	233.9	0.9			
						0.8			
3	0	0	Floor	248	248.1	0	232.5	.304	0
	5	0		248.1	248.1	0	233.5	.306	.002
	5	5		248.1	248.1	0	207	.271	0
	0	5	Wall	248	248	0	206	.270	.001
	0	0		248	248	0	283	.371	0
	5	0		248.1	248.1	0	284.5	.372	.001
	5	5		248.1	248.1	0	230	.301	0
	5	5		248	248	0	228	.298	.003
						0.42			.002
4	0	0	Floor	325	263.9	0			
	5	0		324.8	264.3	0.4			
	5	5		324.8	258.83	0			
	0	5	Wall	325	259.25	0.42			
	0	0		325	263.9	0			
	5	0		324.8	264.3	0.4			
	5	5		324.8	256.33	0			
	5	5		325	256.75	0.42			
						0.41			
5	0	0	Floor	386	386	0	71.4	.657	0
	5	0		385.9	385.9	0	71.2	.656	.001
	5	5		385.9	385.9	0	63.2	.582	0
	0	5	Wall	386	386	0	63.4	.584	.002
	0	0		386	386	0	75.6	.696	0
	5	0		385.9	385.9	0	75.3	.693	.003
	5	5		385.9	385.9	0	65.8	.606	0
	5	5		386	386	0	66.0	.608	.002
						0.41			.002

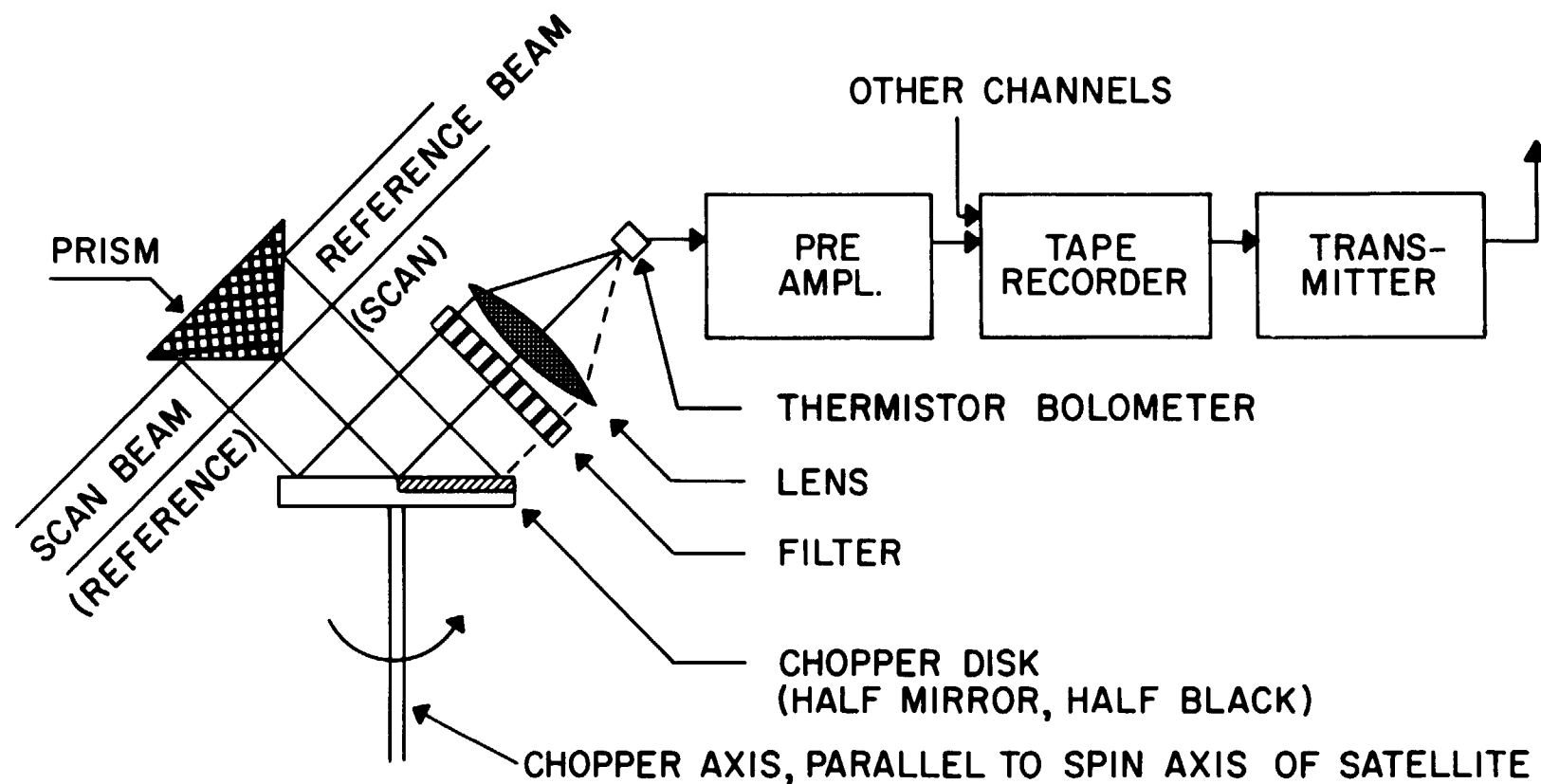


Figure 1—Block diagram of one Channel of the medium resolution scanning radiometer.

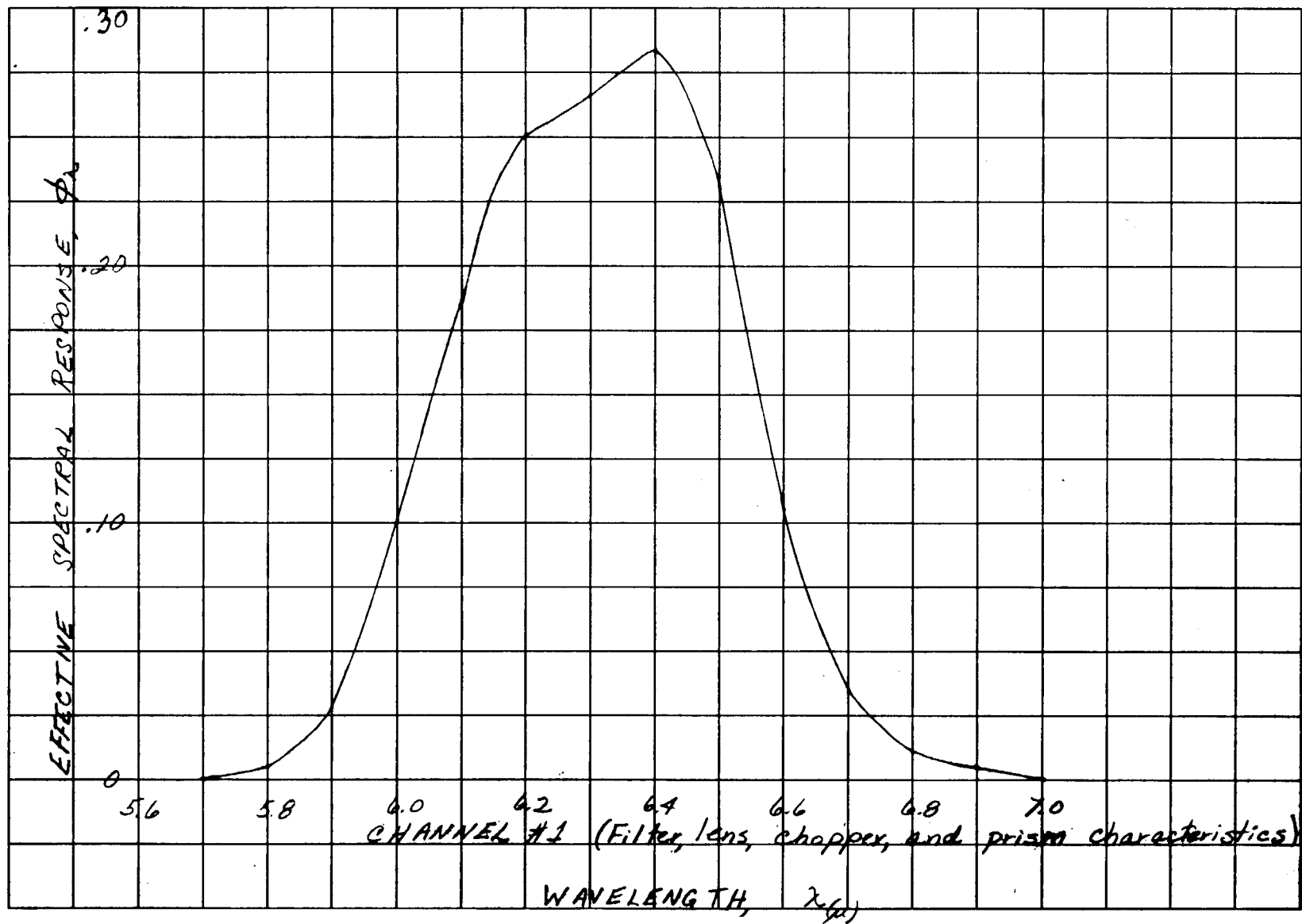


Figure 2—The effective spectral response of Channel 1 versus wavelength.

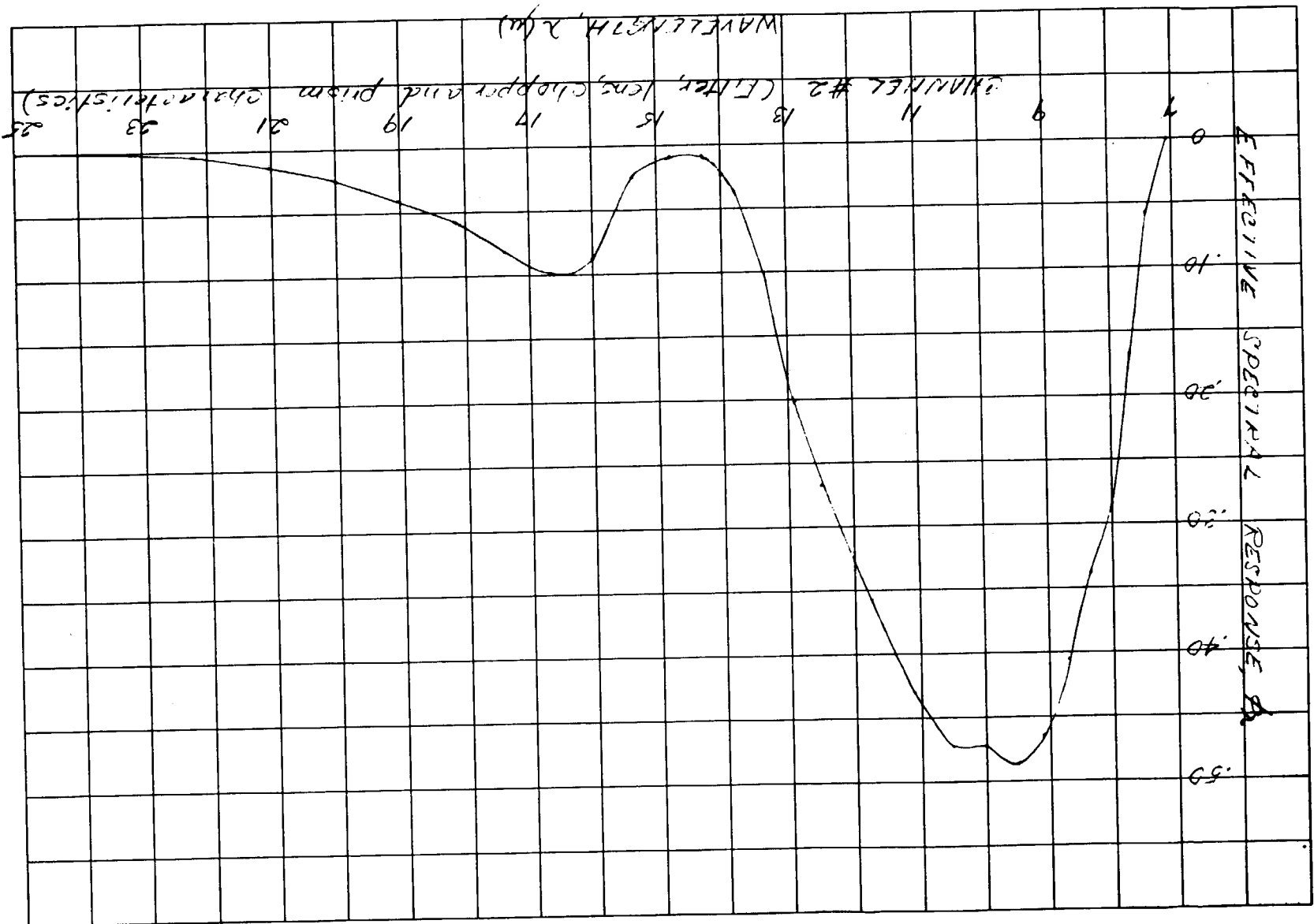


Figure 3—The effective spectral response of Channel 2 versus wavelength.

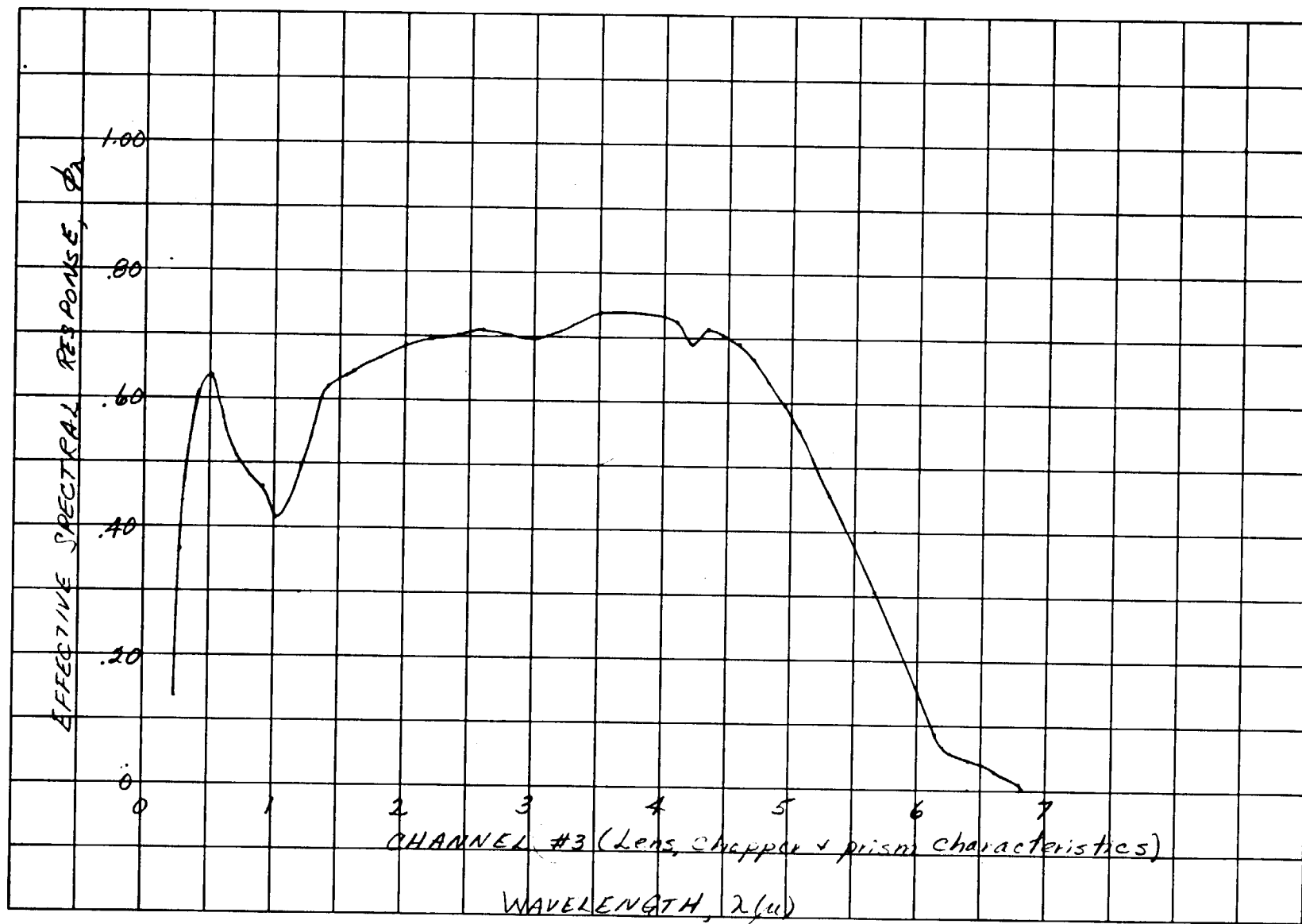
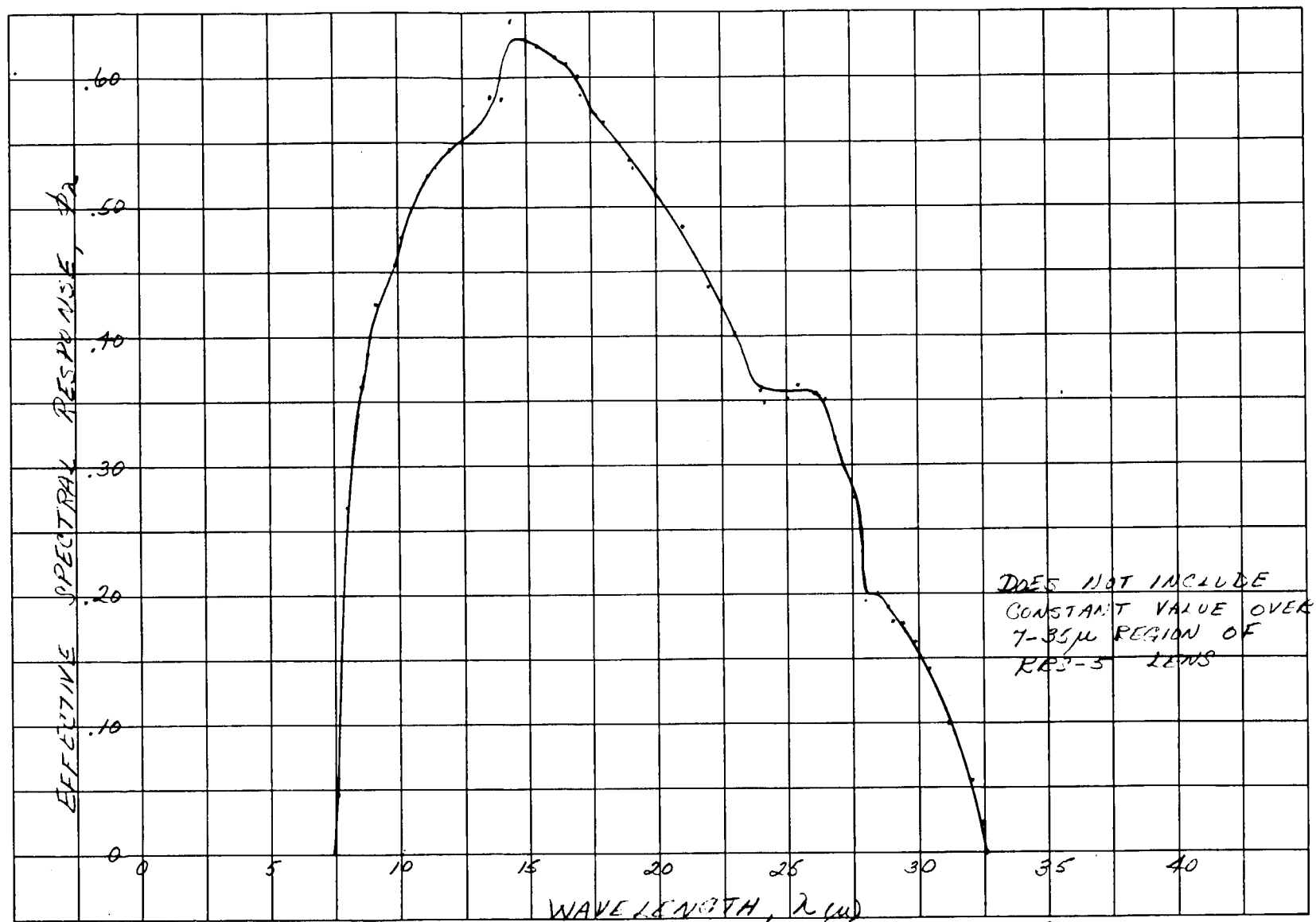


Figure 4—The effective spectral response of Channel 3 versus wavelength.



CHANNEL #4 (Filter, chopper + prism characteristics)

Figure 5—The effective spectral response of Channel 4 versus wavelength.

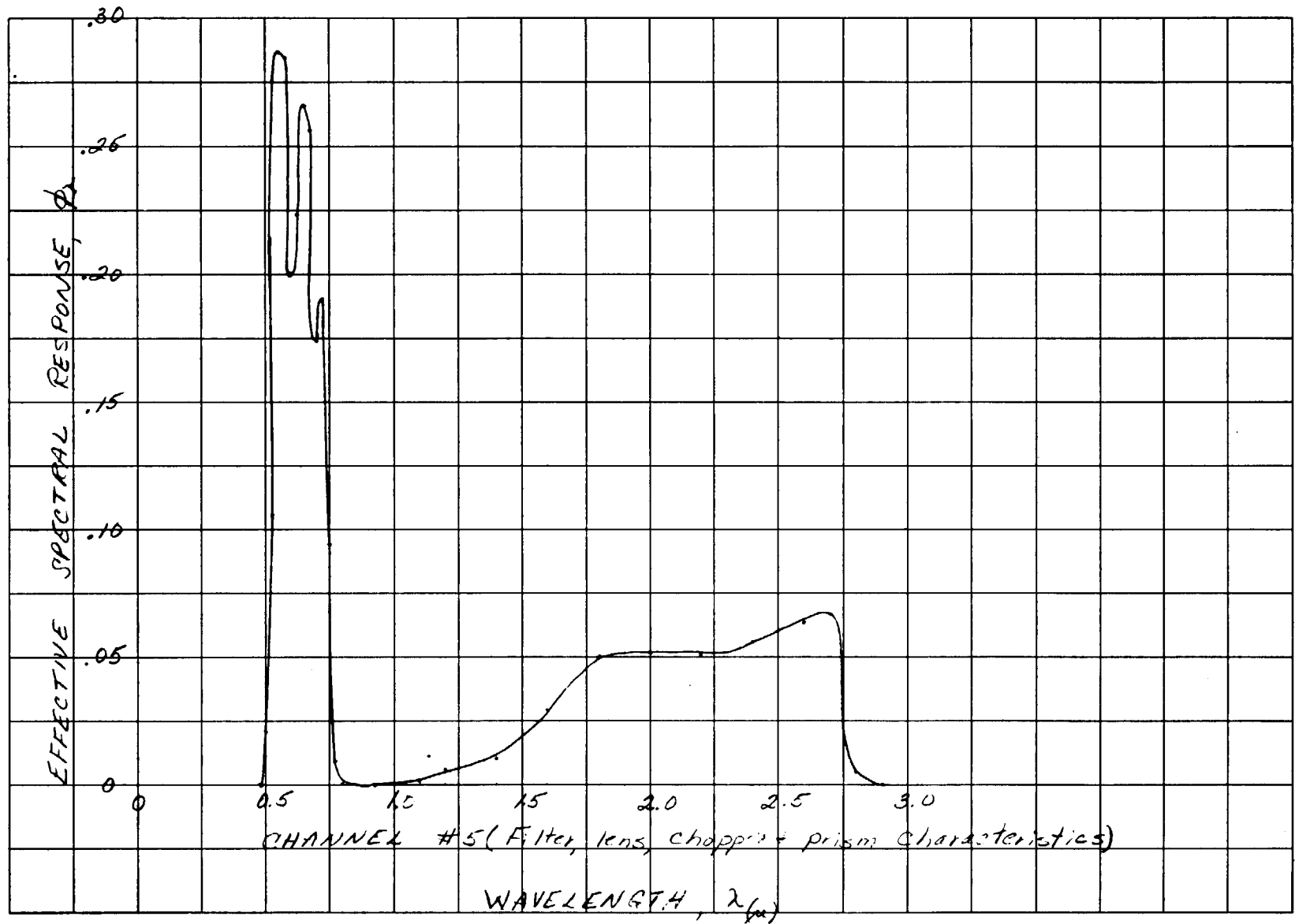
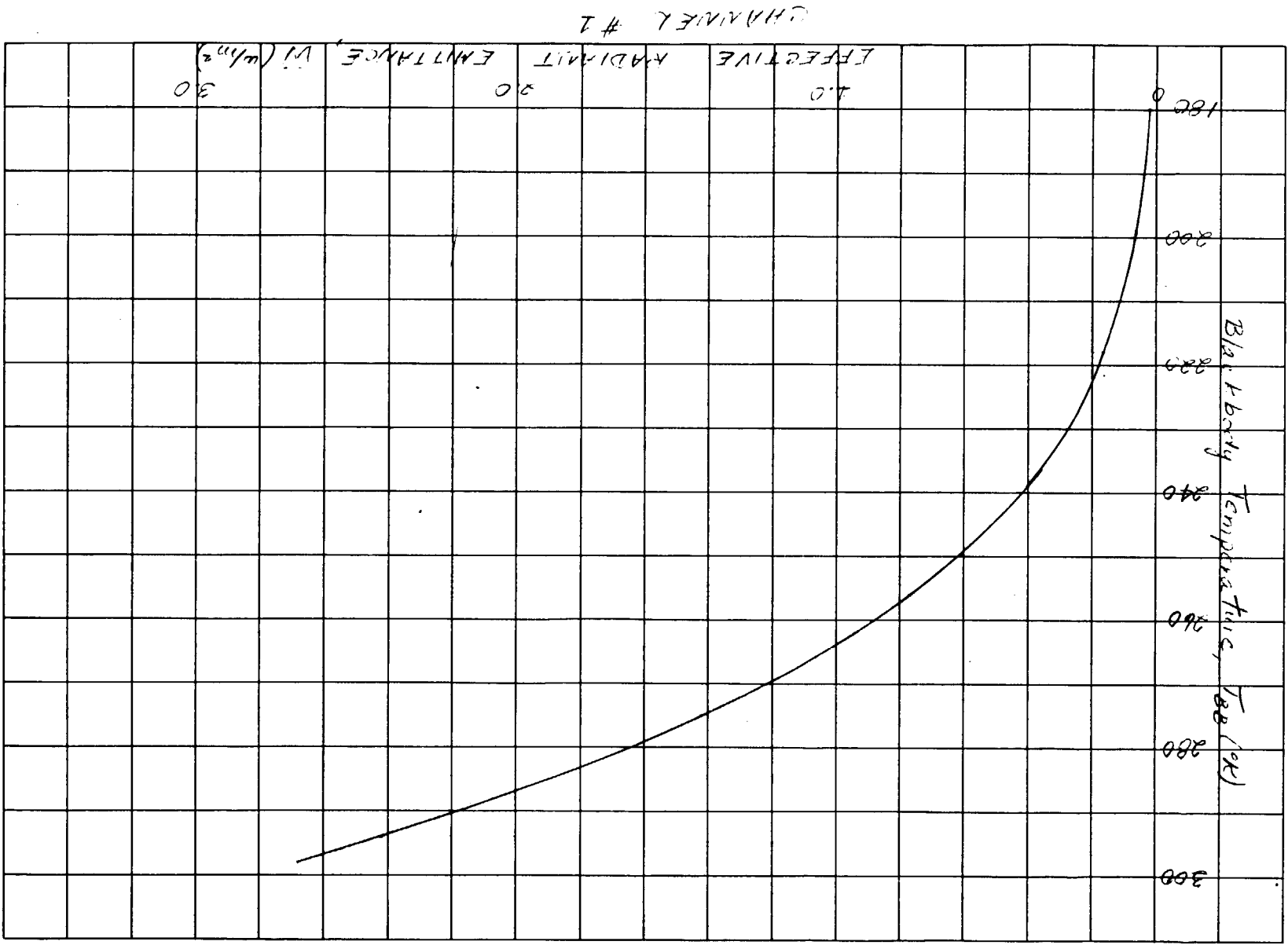


Figure 6—The effective spectral response of Channel 5 versus wavelength.

Figure 7—The effective radiant emittance of Channel 1 versus equivalent blackbody temperature.



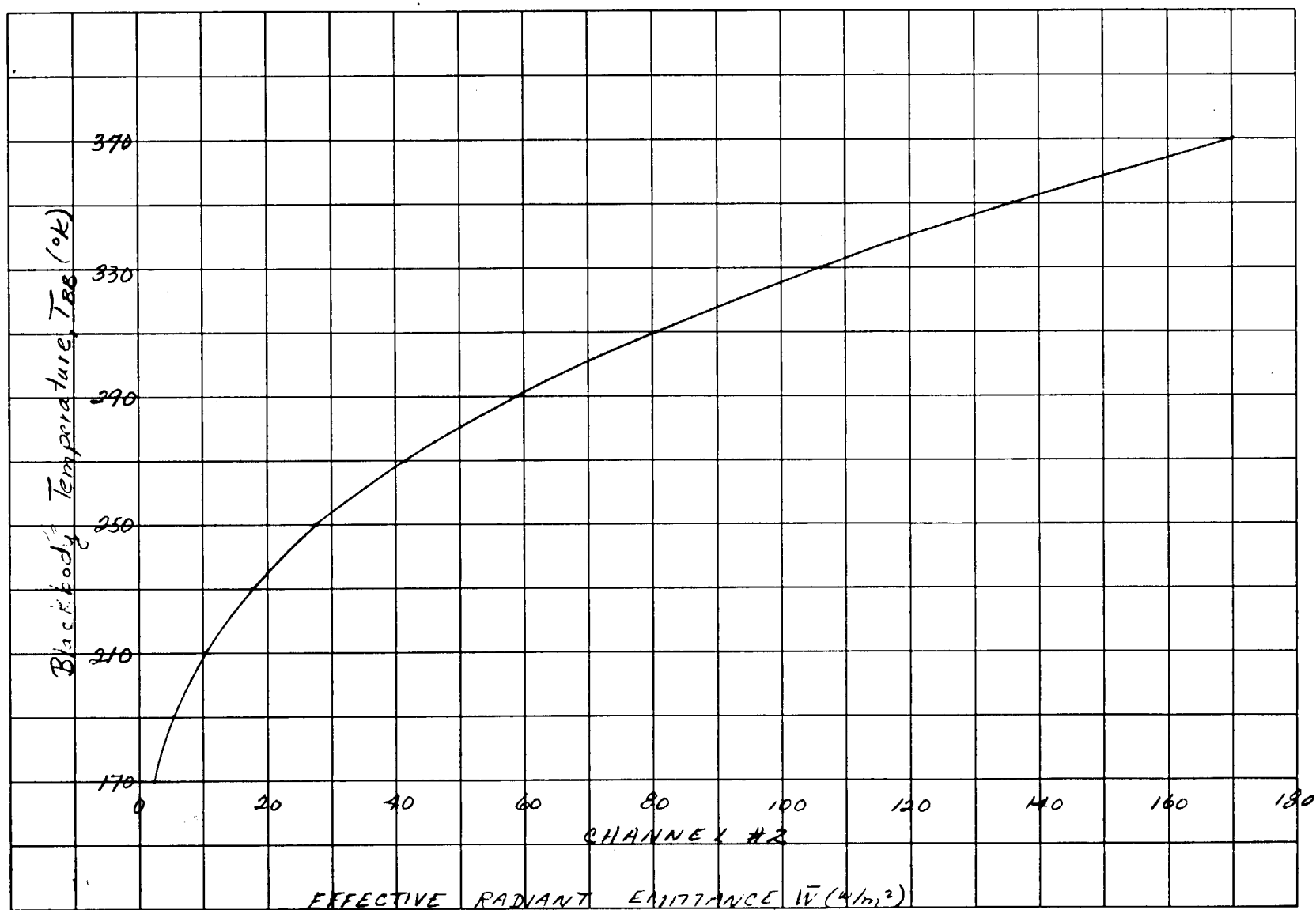


Figure 8—The effective radiant emittance of Channel 2 versus equivalent blackbody temperature.

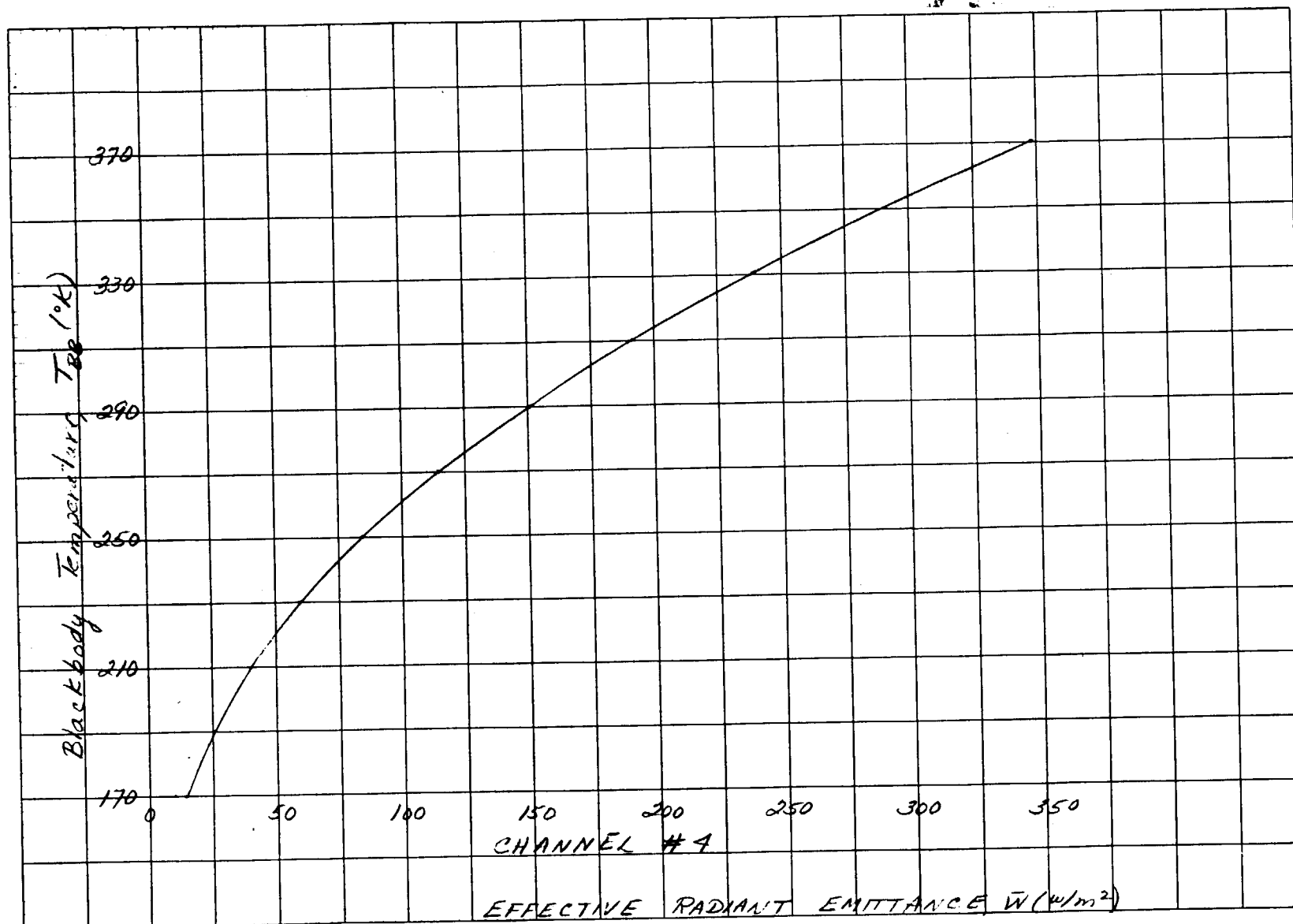


Figure 9—The effective radiant emittance of Channel 4 versus equivalent blackbody temperature.

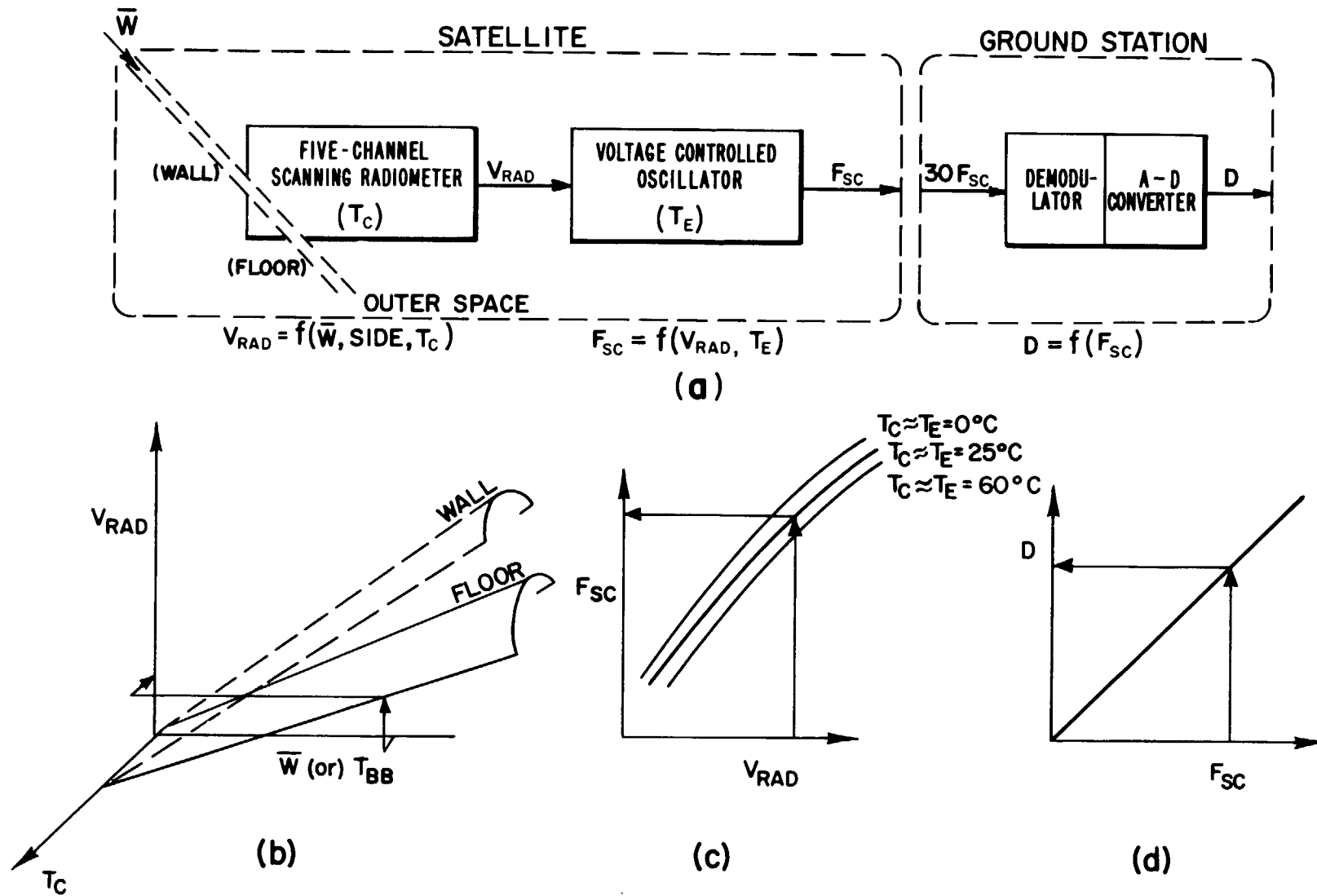


Figure 10—(a) Schematic representation of transfer functions associated with instrumentation in the satellite and at the ground station. (b) Three-dimensional representation of the response of the five-channel scanning radiometer. (c) The response of the voltage controlled oscillator shown as a parametric function of the electronics temperature T_E . (d) Conversion from subcarrier frequency to digital number.

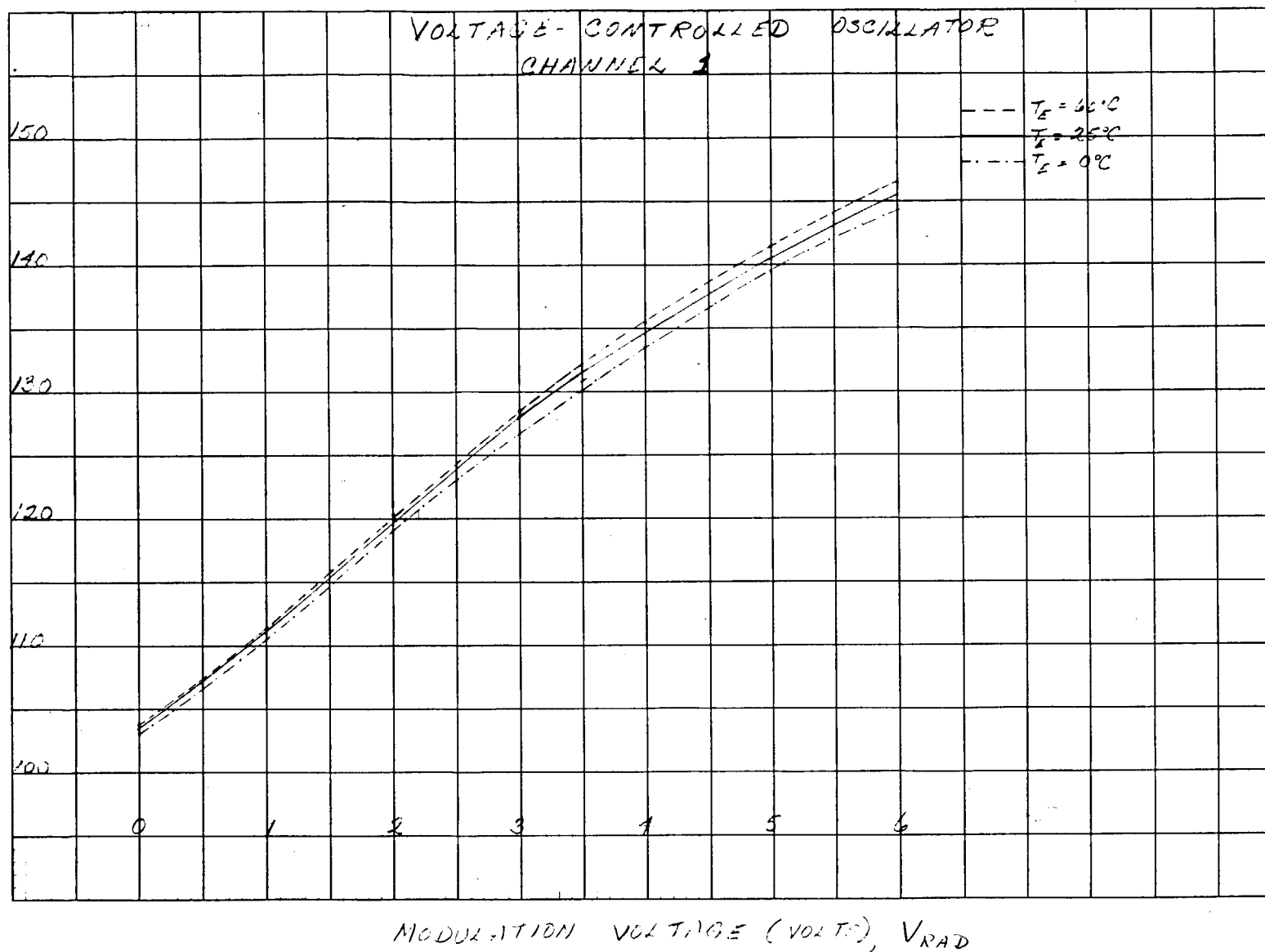


Figure 11—The response of the voltage controlled oscillator for Channel 1 shown as a parametric function of the electronics temperature, T_E .

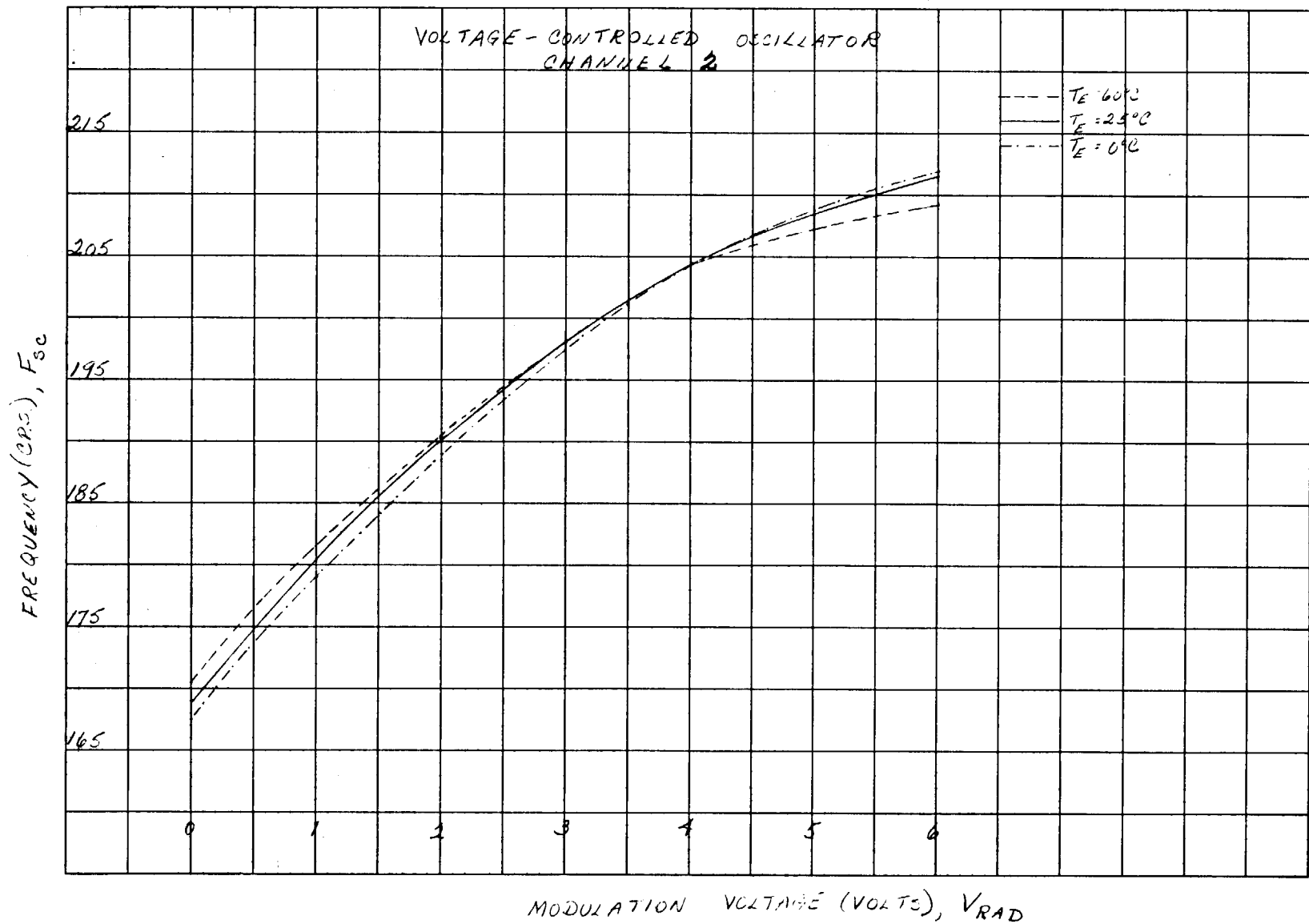


Figure 12—The response of the voltage controlled oscillator for Channel 2 shown as a parametric function of the electronics temperature, T_E .

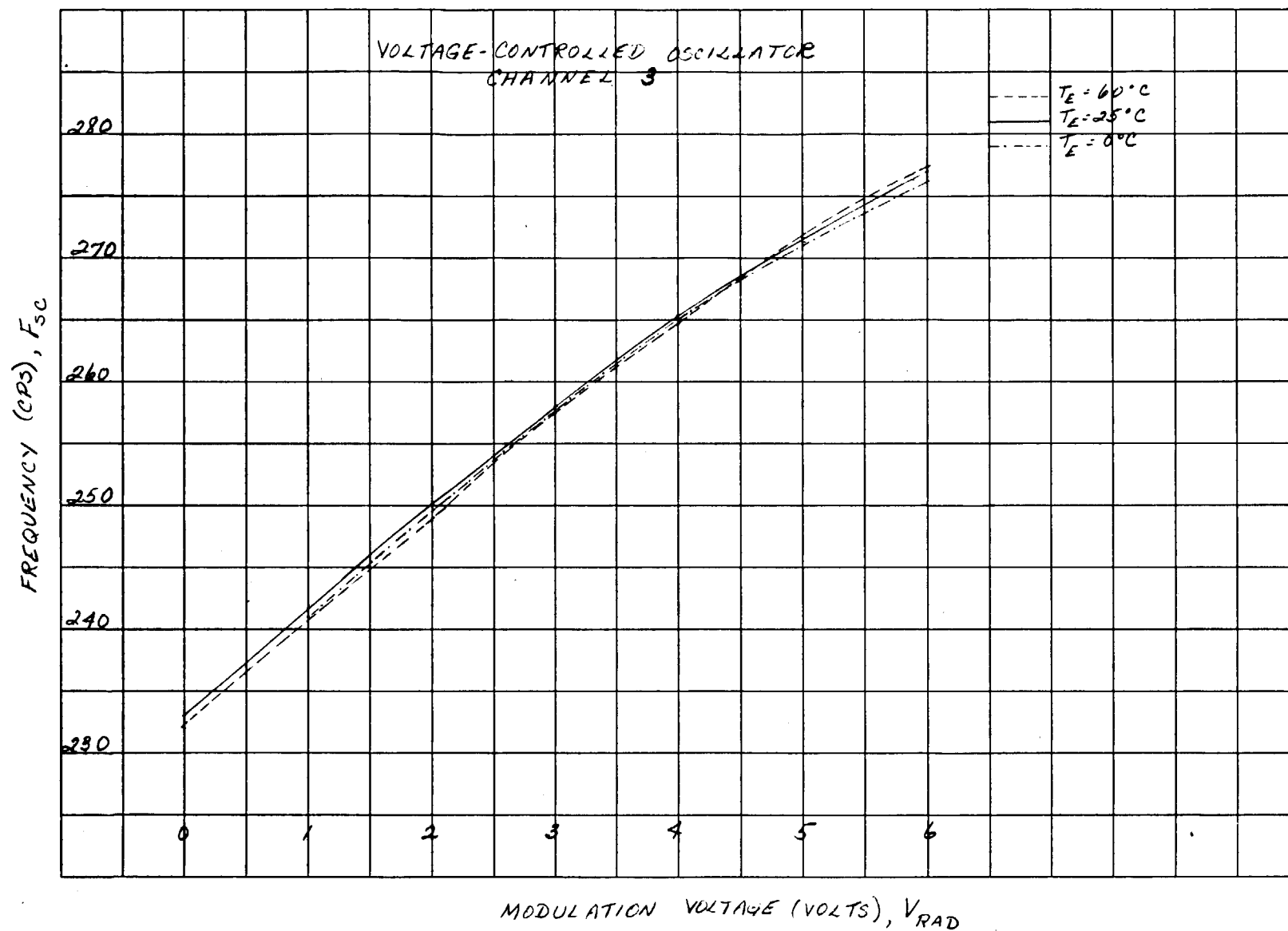


Figure 13—The response of the voltage controlled oscillator for Channel 3 shown as a parametric function of the electronics temperature, T_E .

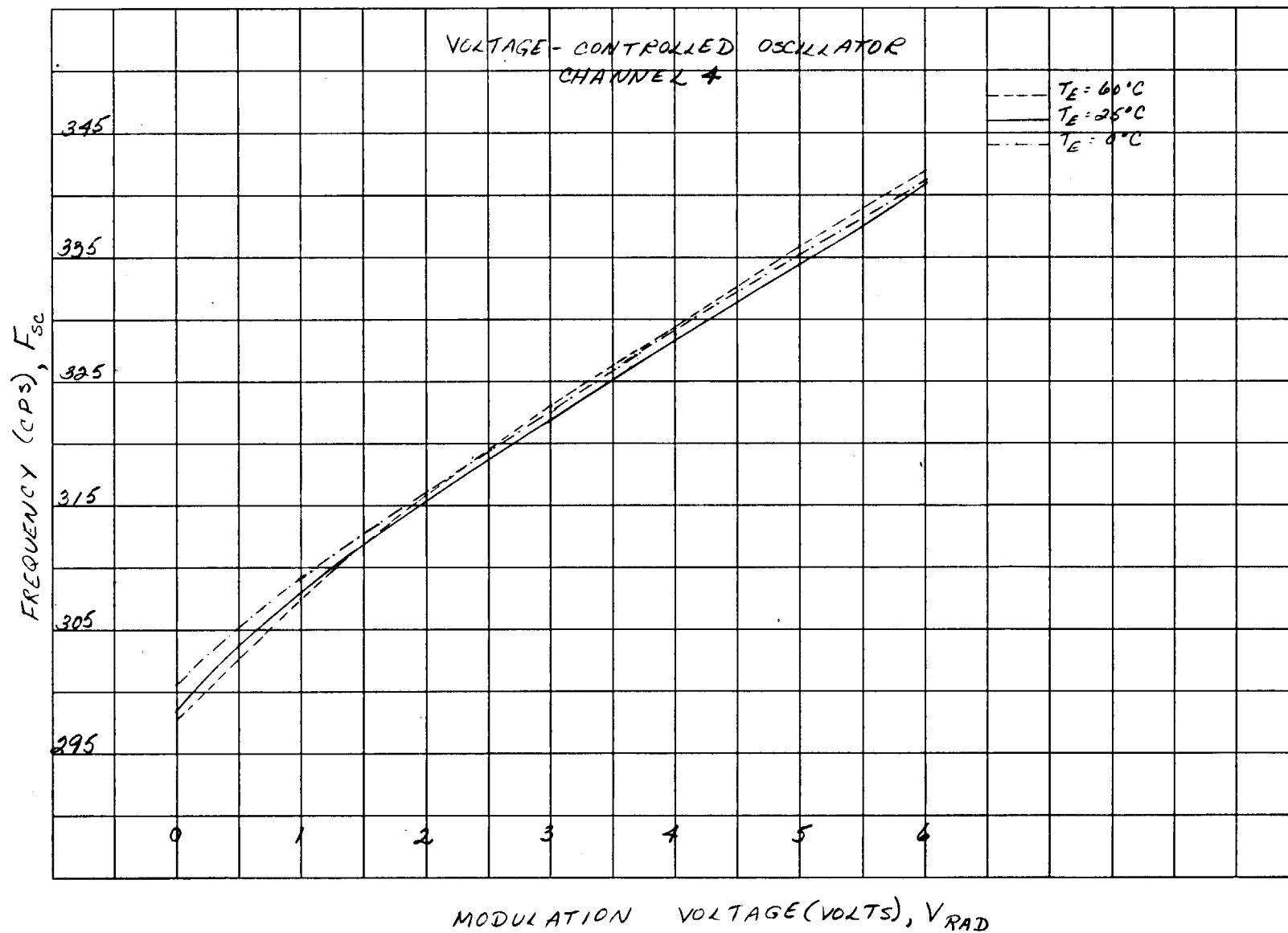


Figure 14—The response of the voltage controlled oscillator for Channel 4 shown as a parametric function of the electronics temperature, T_E .

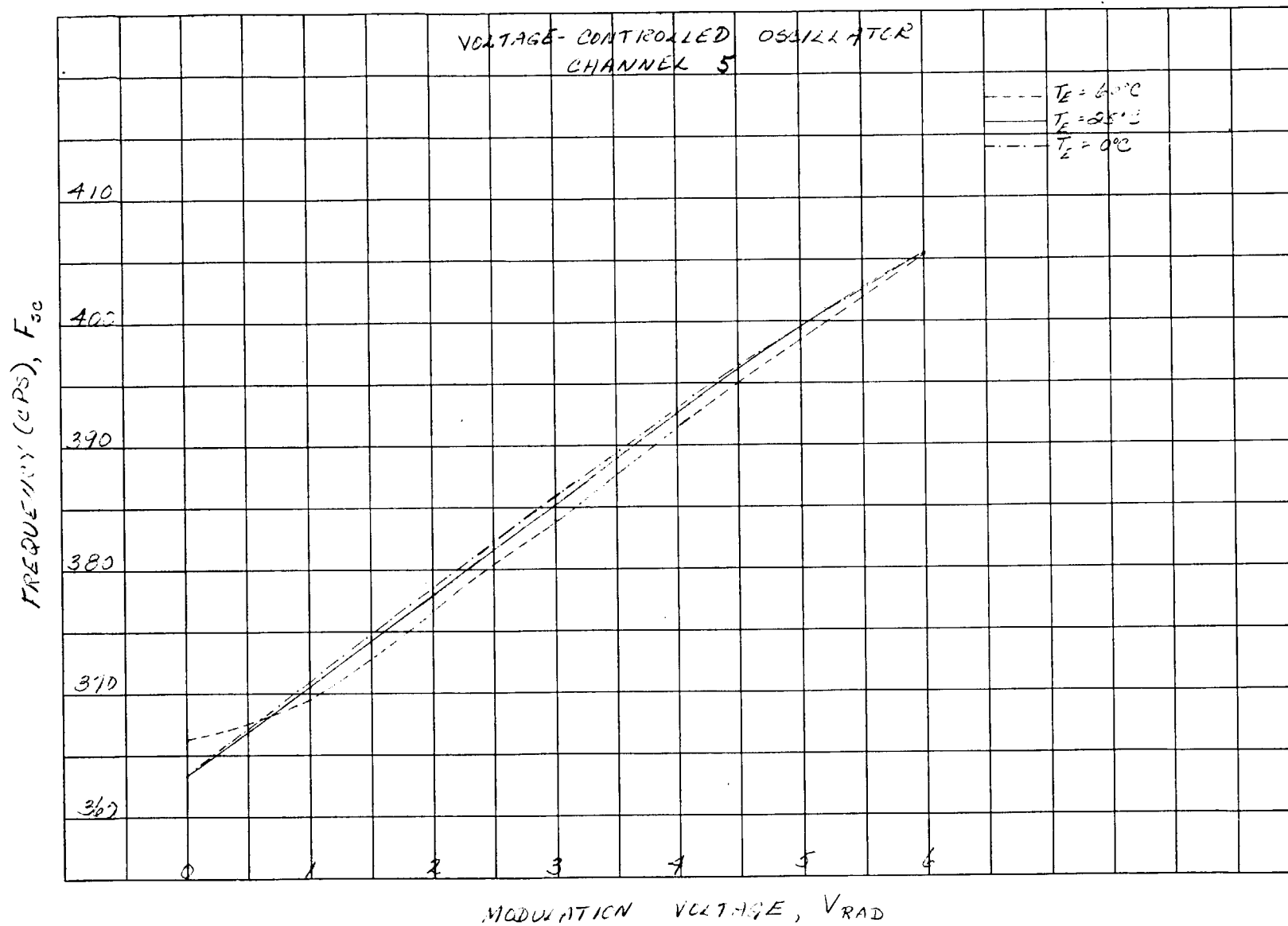


Figure 15—The response of the voltage controlled oscillator for Channel 5 shown as a parametric function of the electronics temperature, T_E .

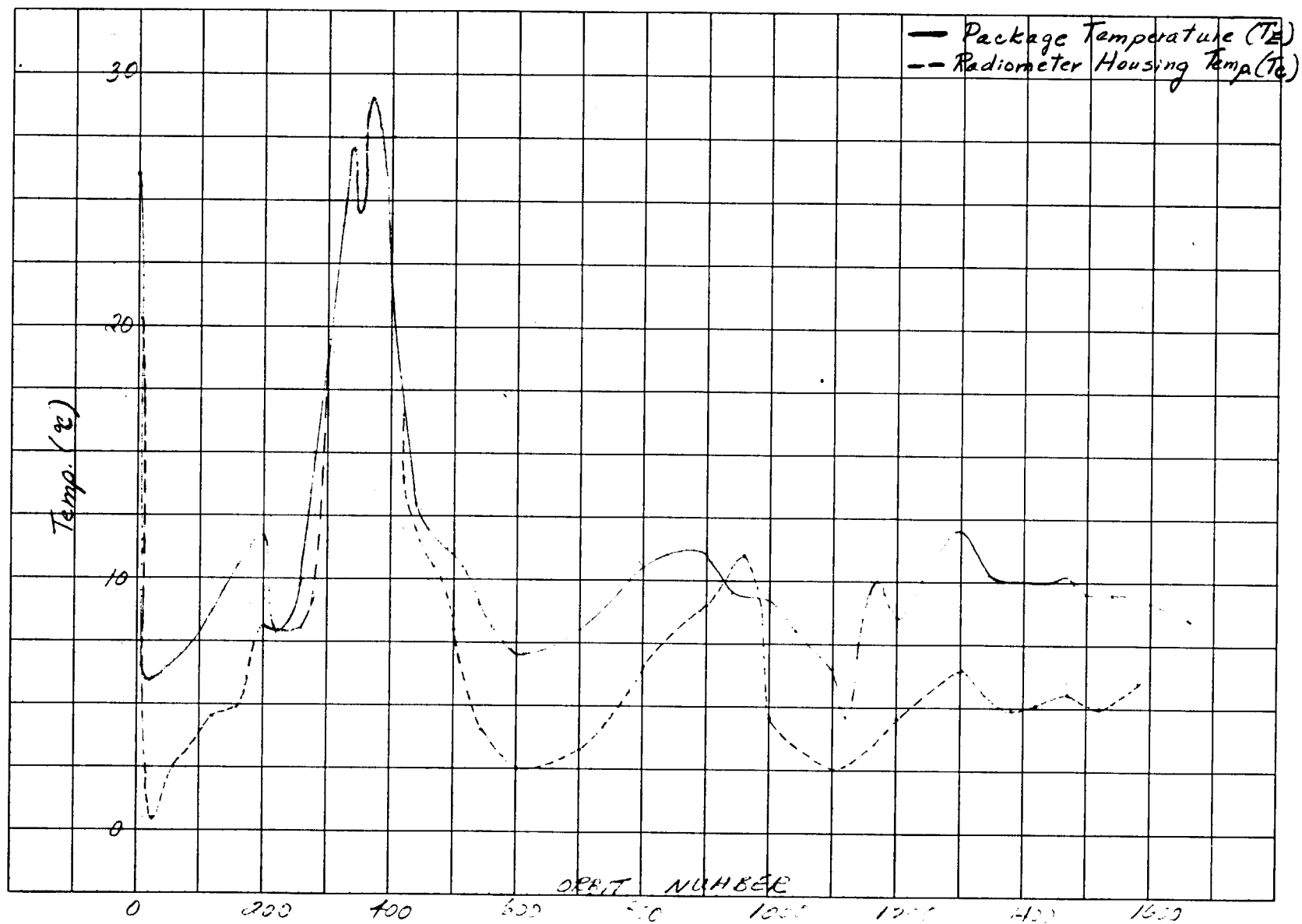


Figure 16—A temperature comparison of T_G and T_E for TIROS III.

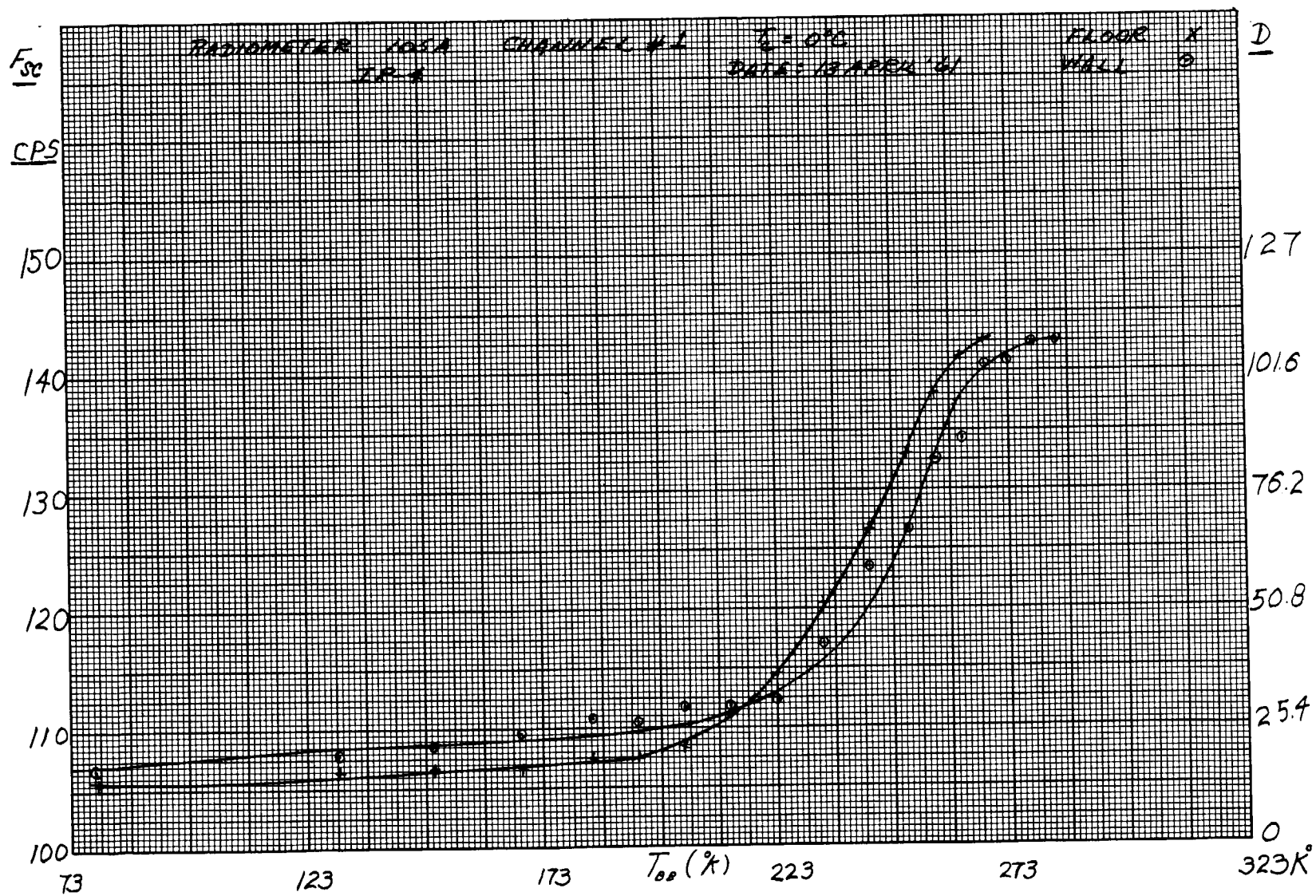


Figure 17—Subcarrier frequency and digital number versus blackbody temperature for wall and floor sides, Channel 1.
 ($T_c = 0^\circ\text{C}$)

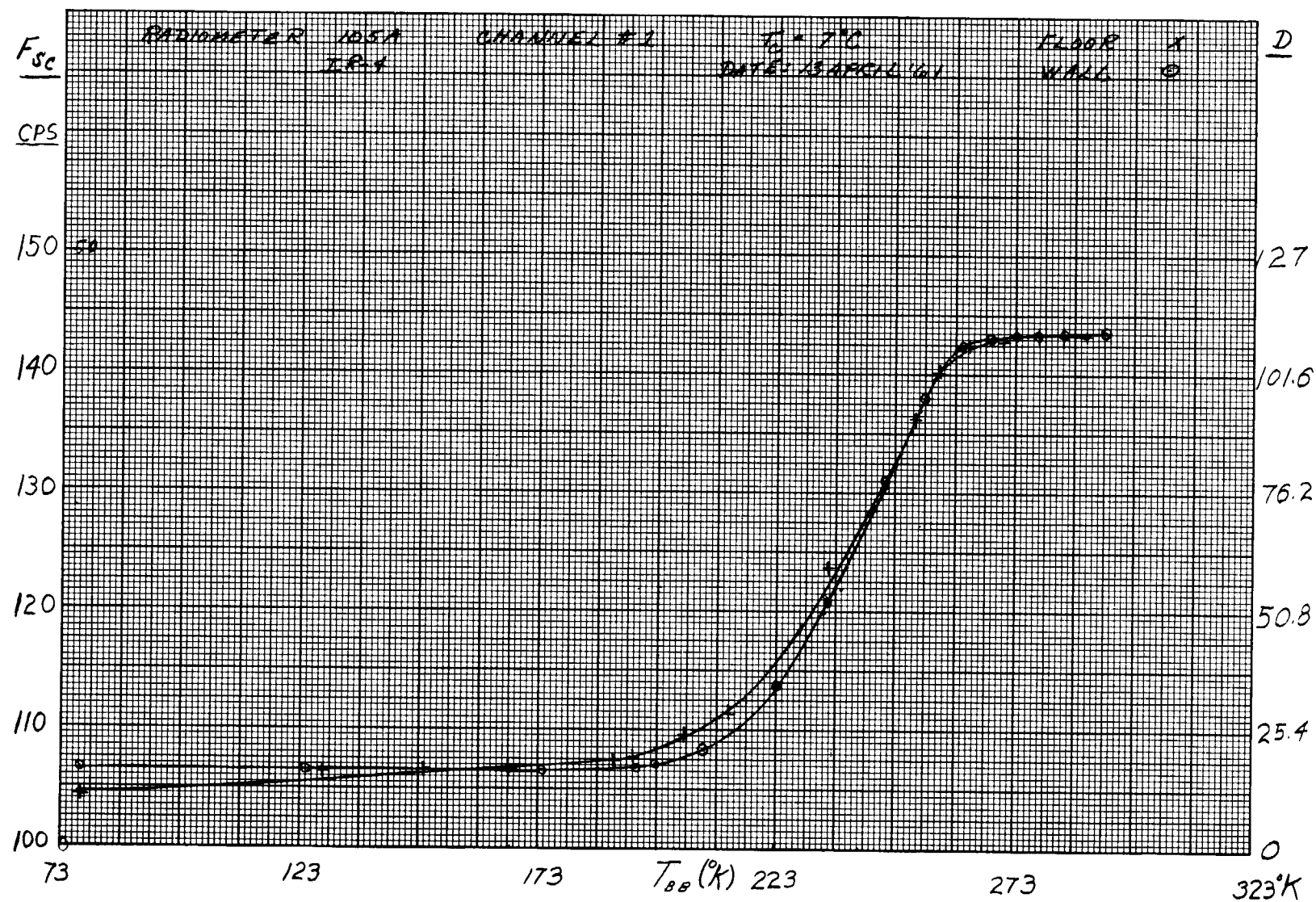


Figure 18—Subcarrier frequency and digital number versus blackbody temperature for wall and floor sides, Channel 1.
($T_c = 7^\circ\text{C}$)

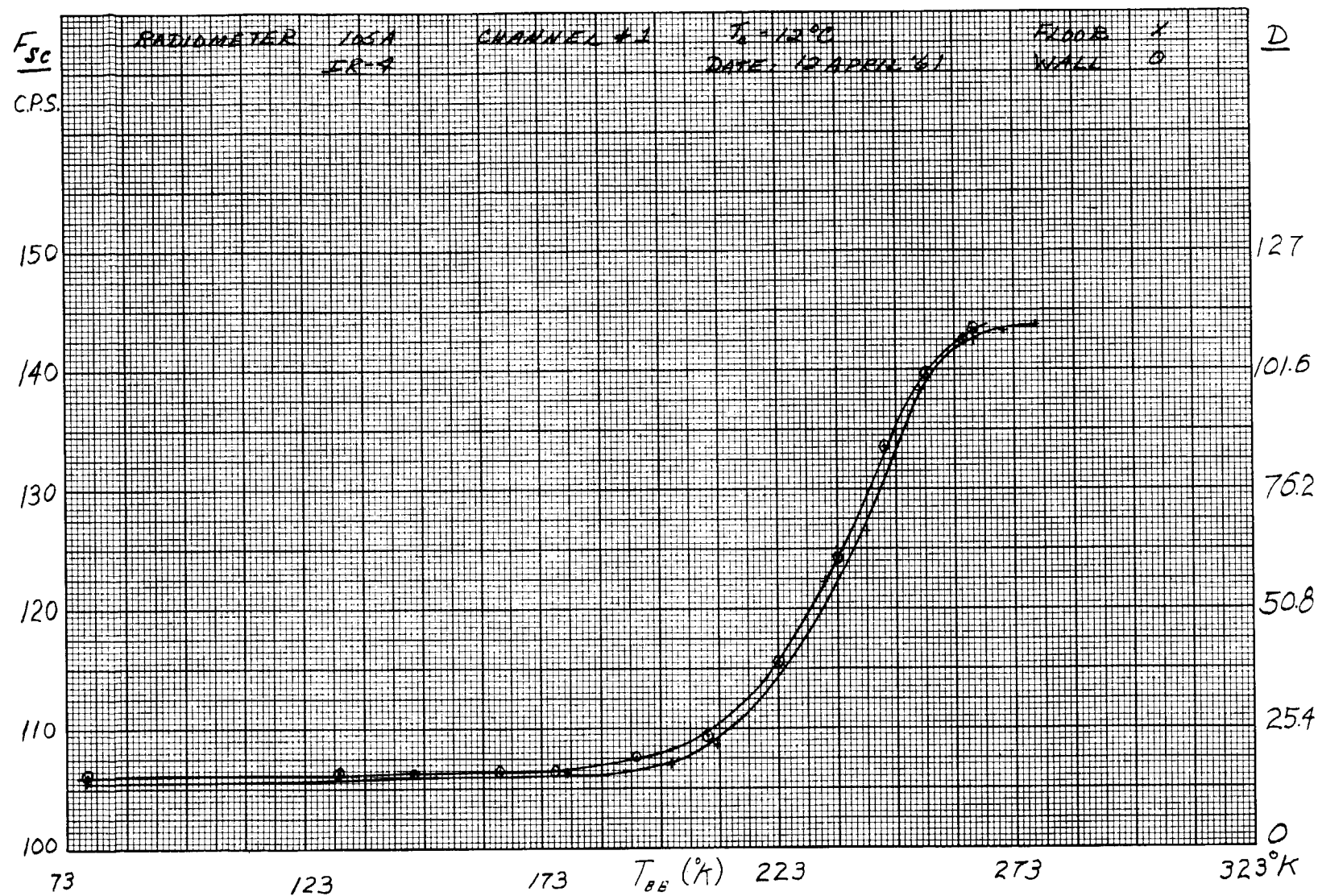


Figure 19—Subcarrier frequency and digital number versus blackbody temperature for wall and floor sides, Channel 1.
 ($T_c = 12^\circ\text{C}$)

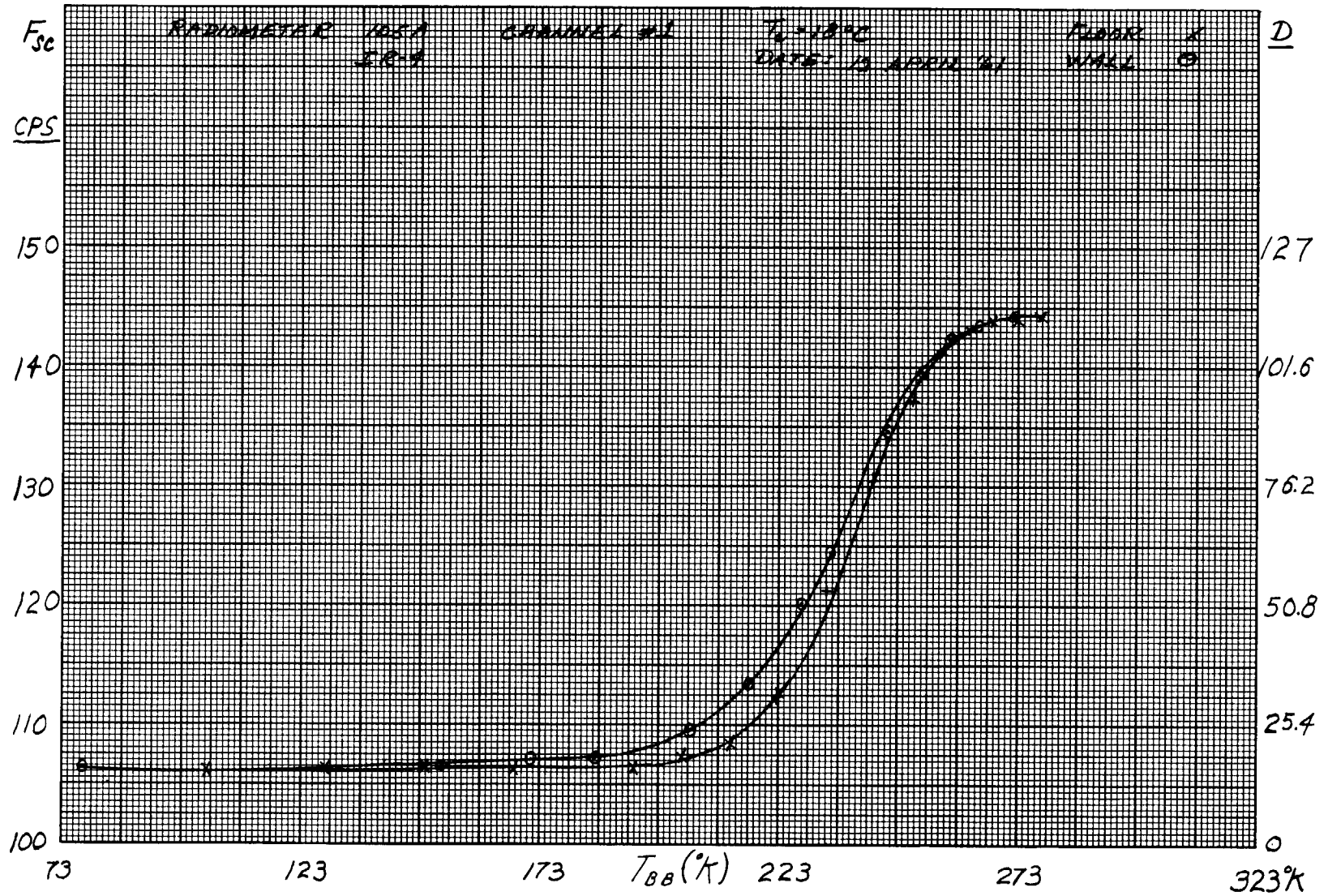


Figure 20—Subcarrier frequency and digital number versus blackbody temperature for wall and floor sides, Channel 1.
 $(T_c = 18^\circ\text{C})$

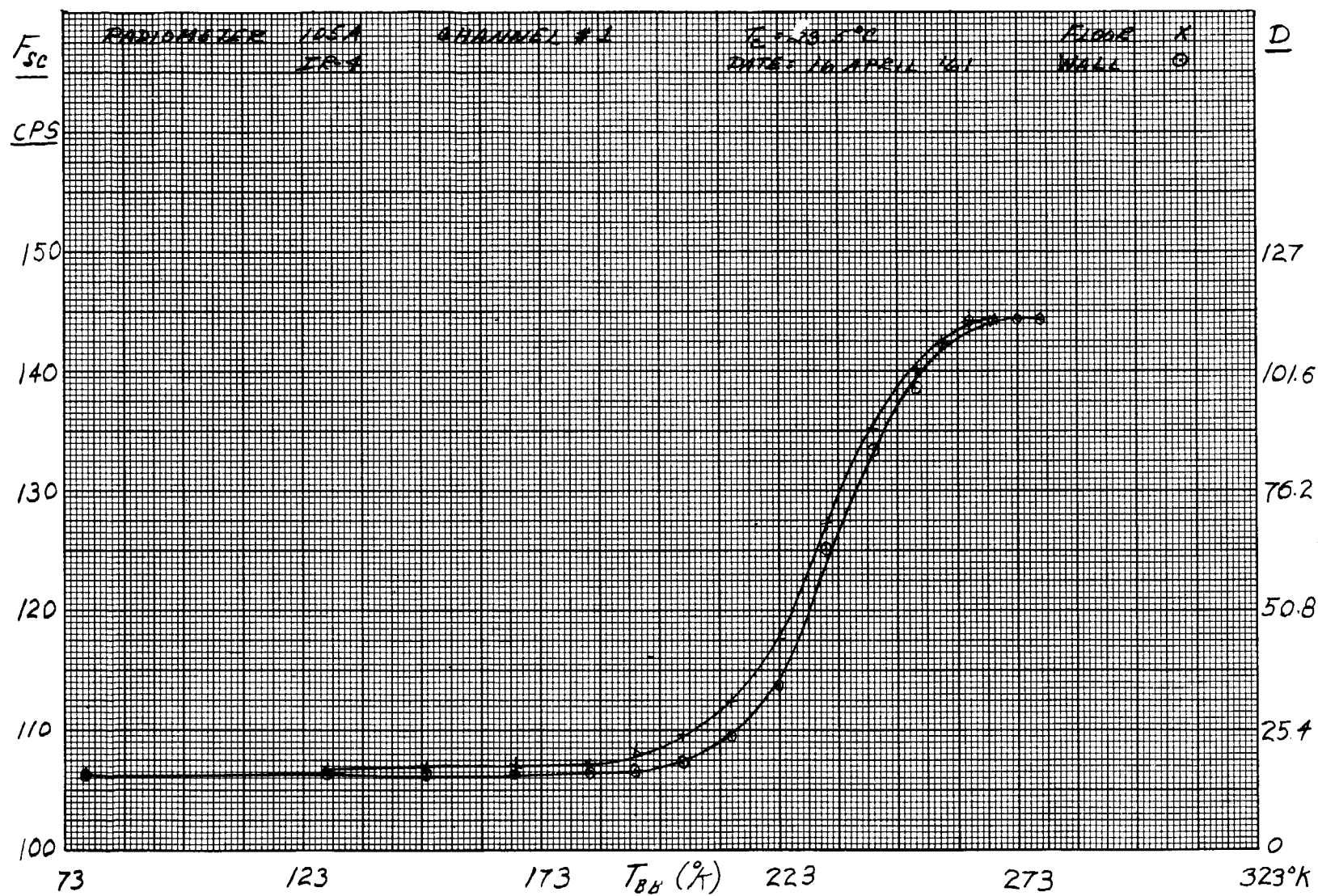


Figure 21—Subcarrier frequency and digital number vs. blackbody temperature for wall and floor sides, Channel 1.
 ($T_c = 23.5^\circ\text{C}$)

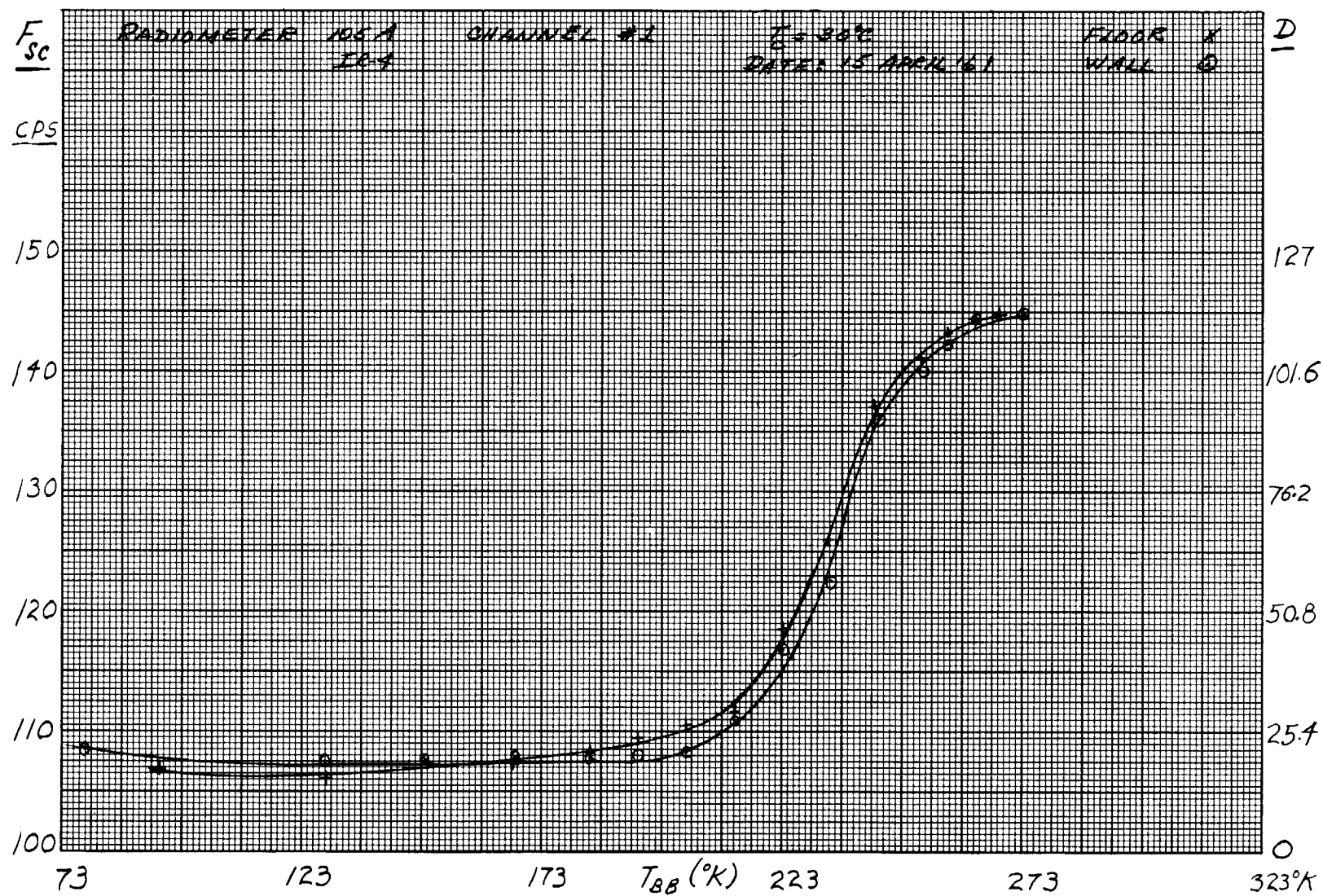


Figure 22—Subcarrier frequency and digital number vs. blackbody temperature for wall and floor sides, Channel 1.
 ($T_c = 30^\circ\text{C}$)

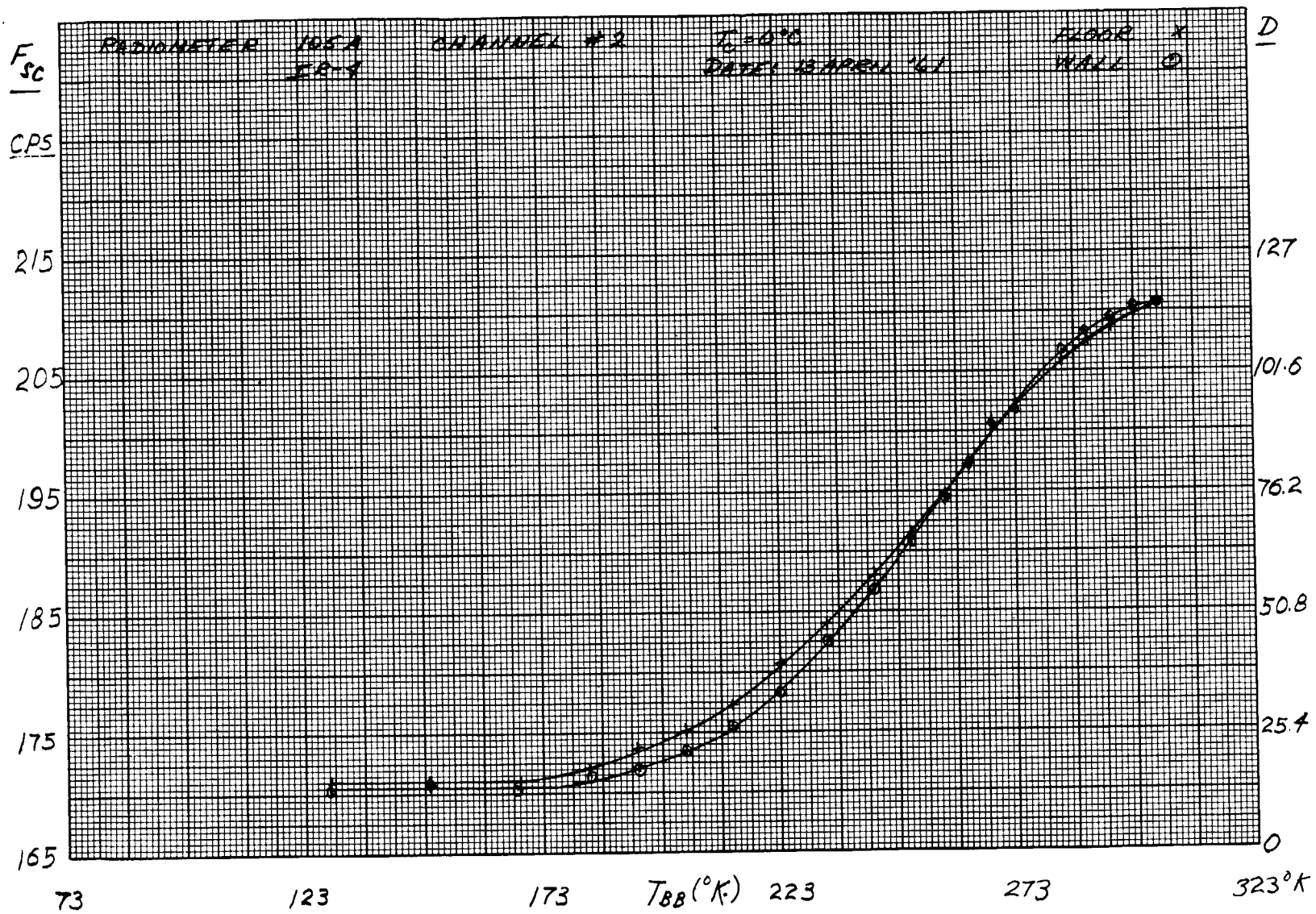


Figure 23—Subcarrier frequency and digital number vs. blackbody temperature for wall and floor sides, Channel 2.
 ($T_c = 0^\circ\text{C}$)

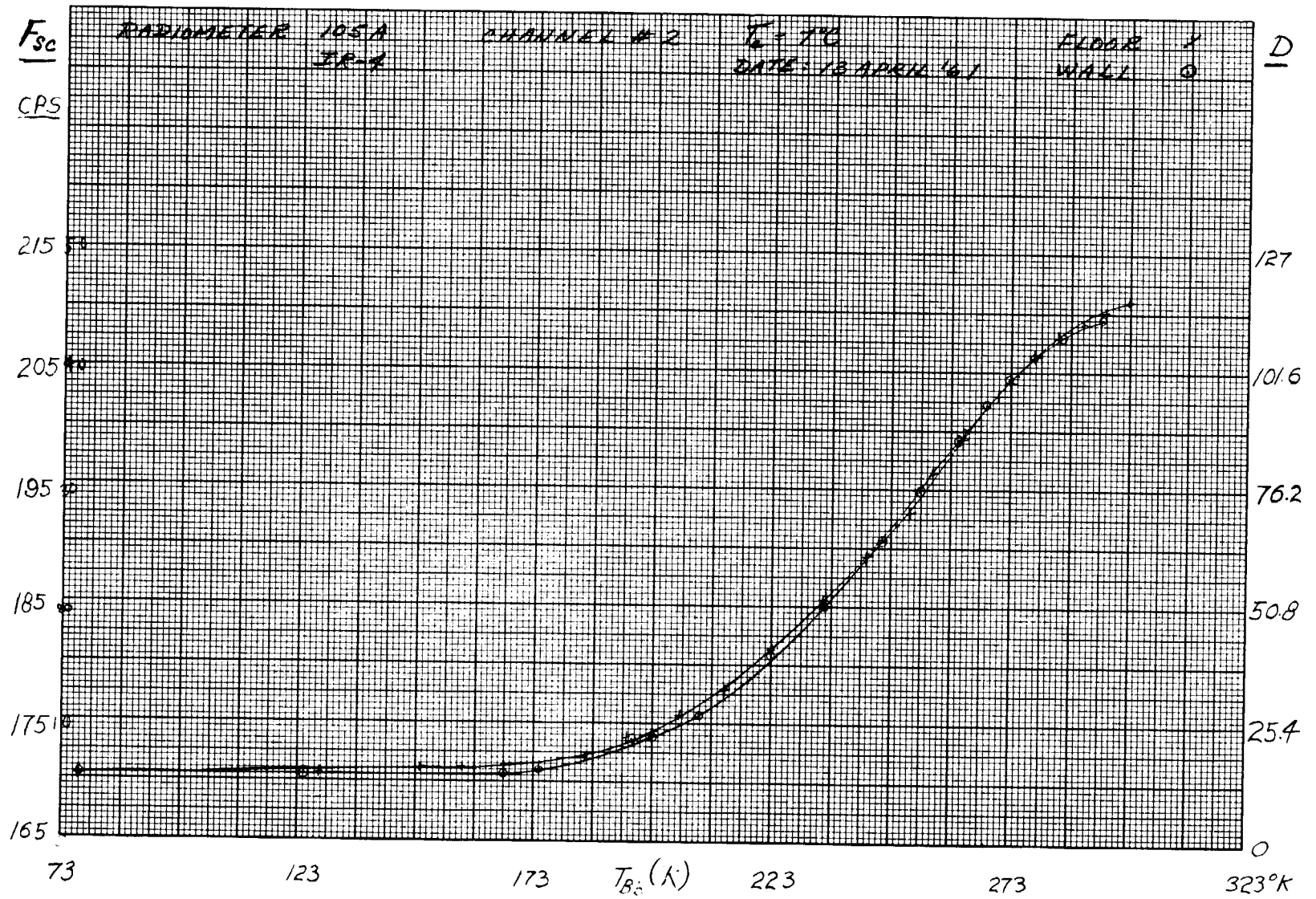


Figure 24—Subcarrier frequency and digital number vs. blackbody temperature for wall and floor sides, Channel 2.
 ($T_c = 7^\circ\text{C}$)

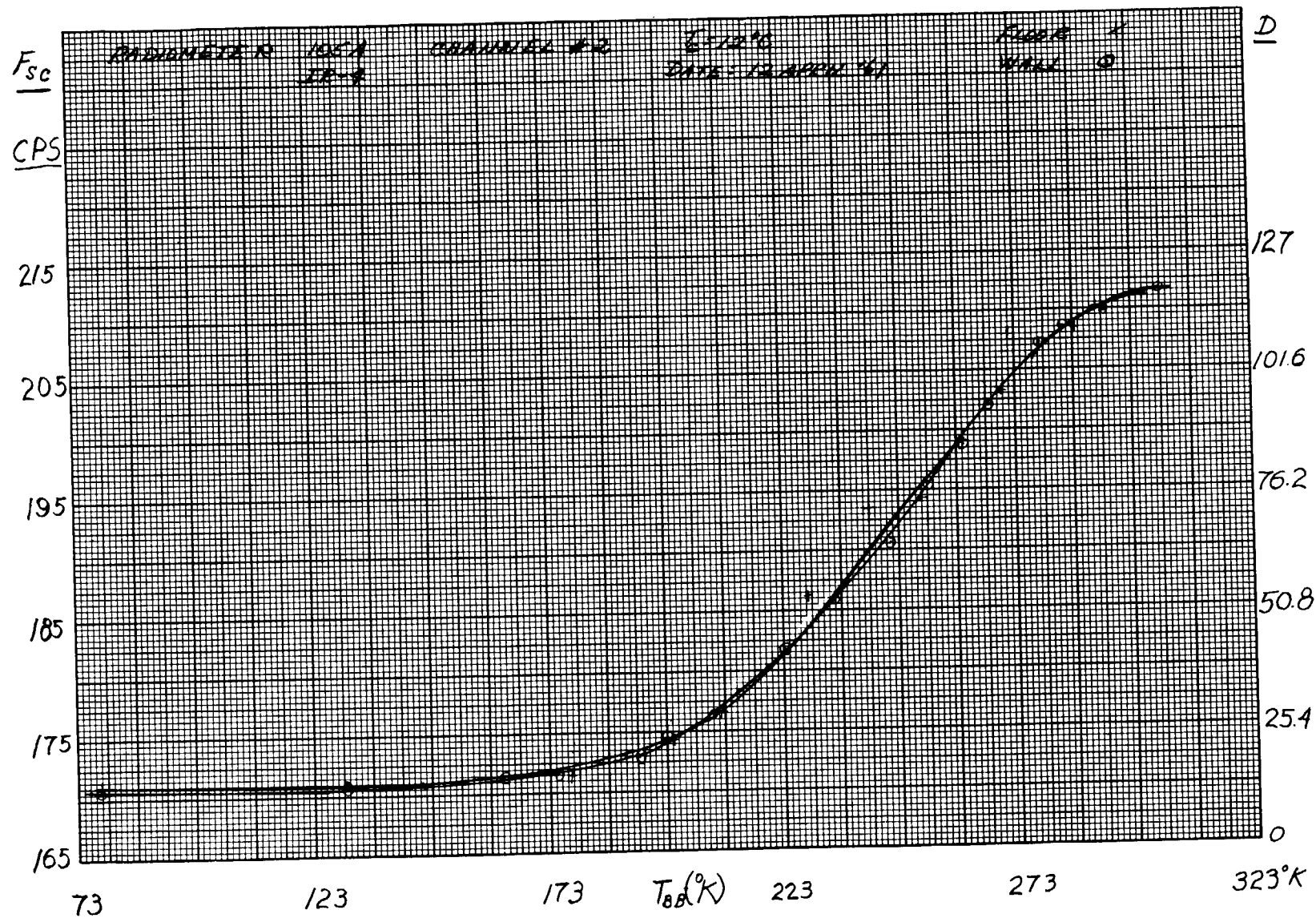


Figure 25—Subcarrier frequency and digital number vs. blackbody temperature for wall and floor sides, Channel 2.
 ($T_c = 12^{\circ}C$)

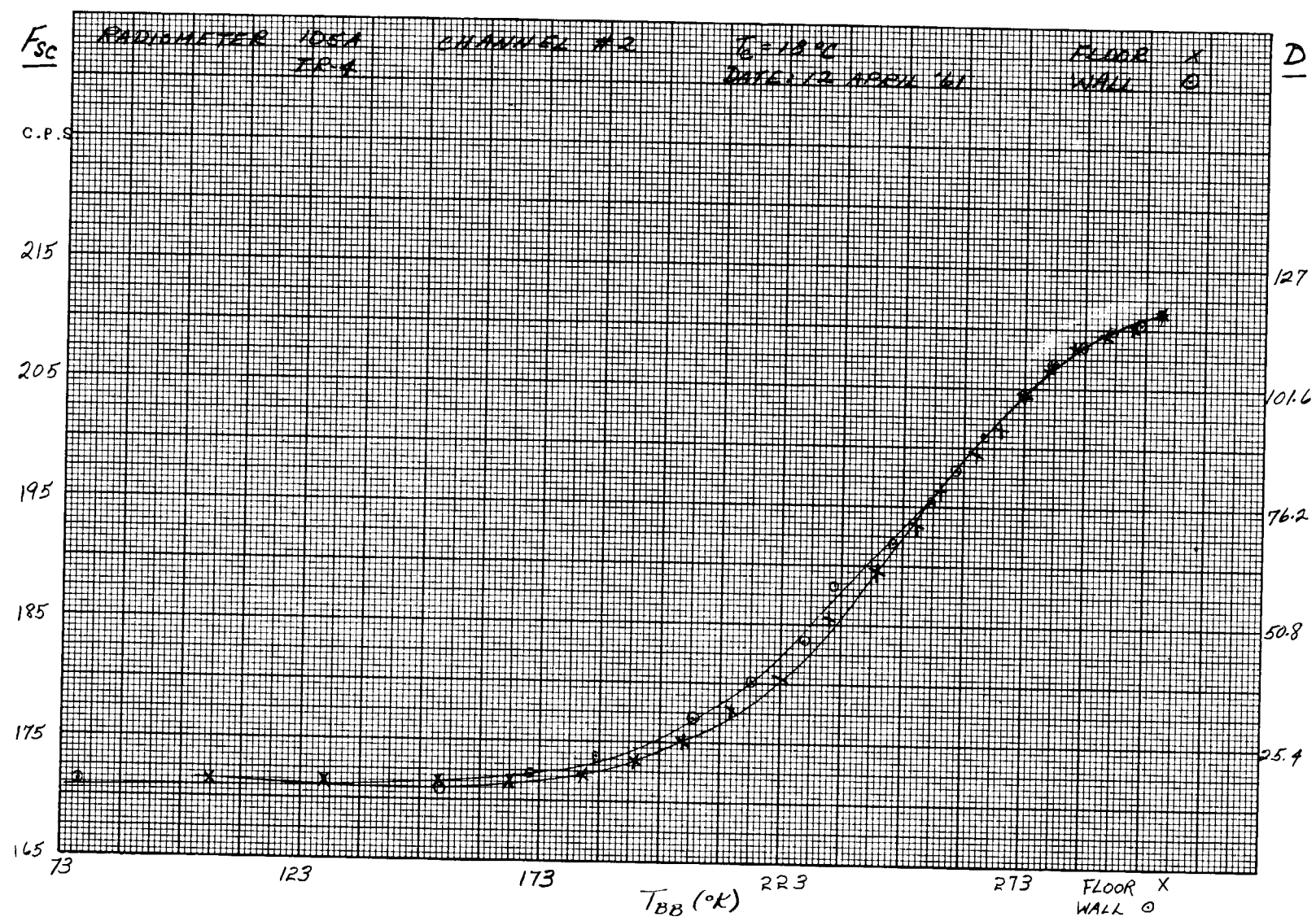


Figure 26—Subcarrier frequency and digital number vs. blackbody temperature for wall and floor sides, Channel 2.
($T_c = 18^\circ C$)

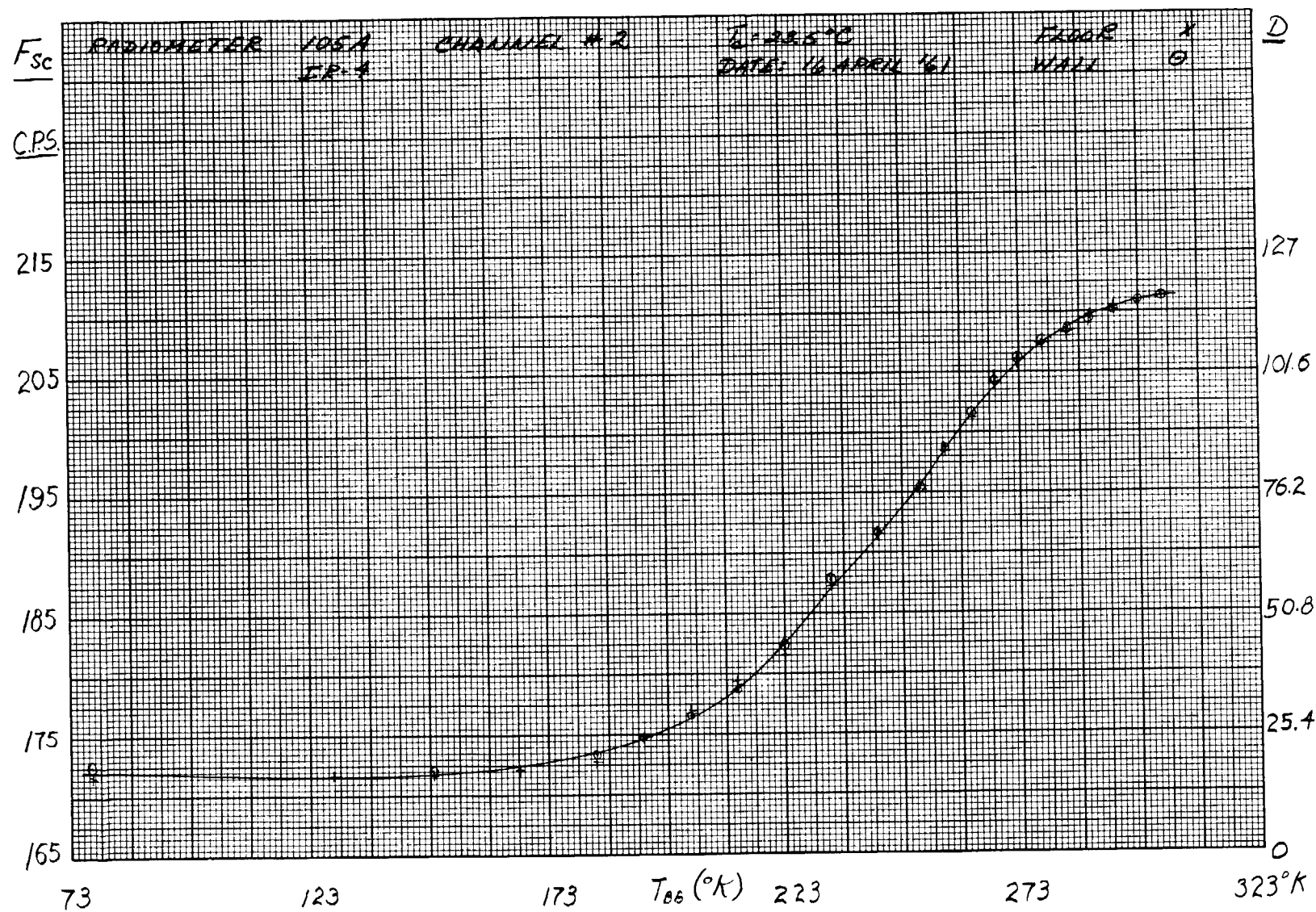


Figure 27—Subcarrier frequency and digital number vs. blackbody temperature for wall and floor sides, Channel 2.
 $(T_c = 23.5^\circ\text{C})$

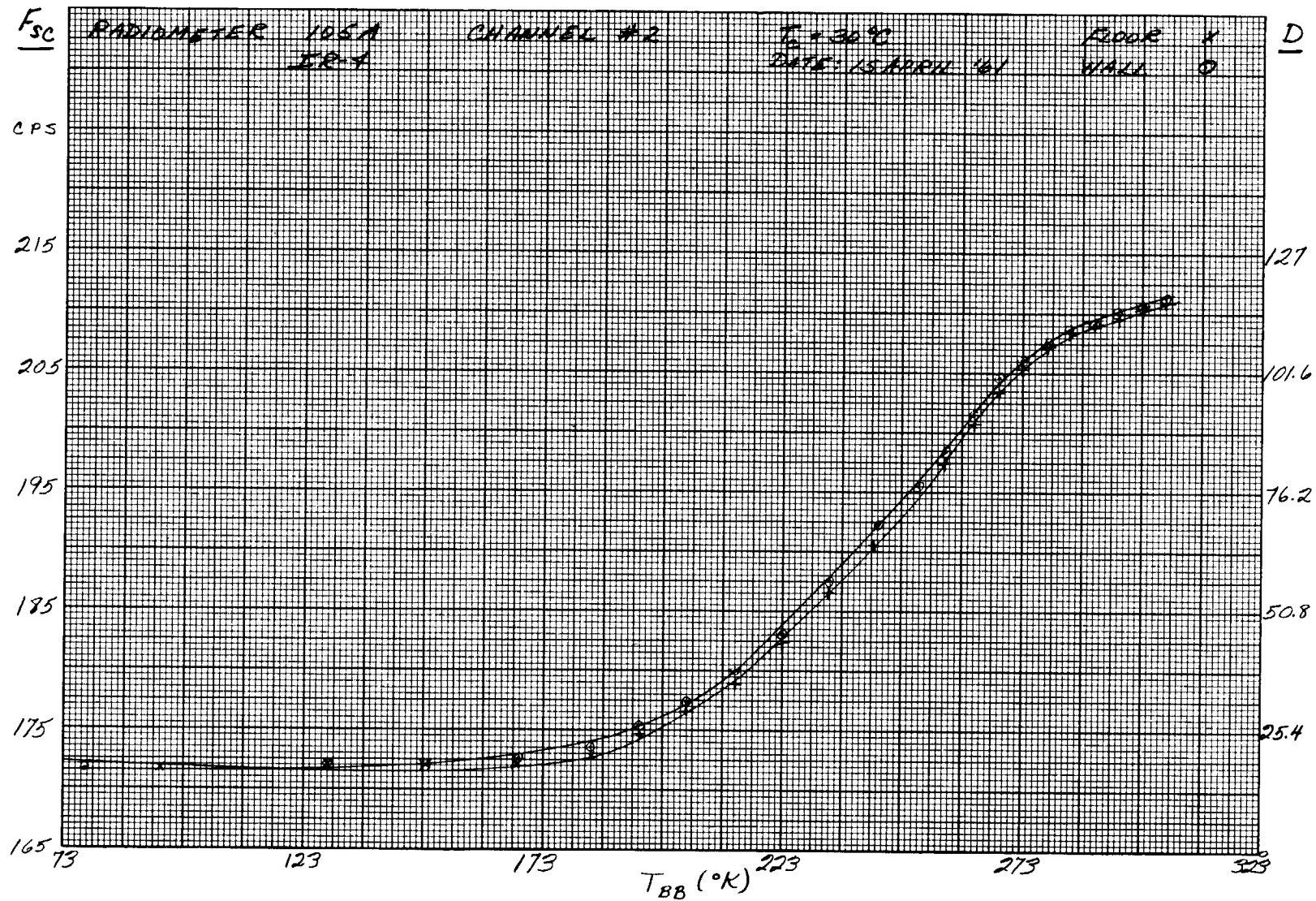


Figure 28—Subcarrier frequency and digital number vs. blackbody temperature for wall and floor sides, Channel 2.
 $(T_c = 30^\circ C)$

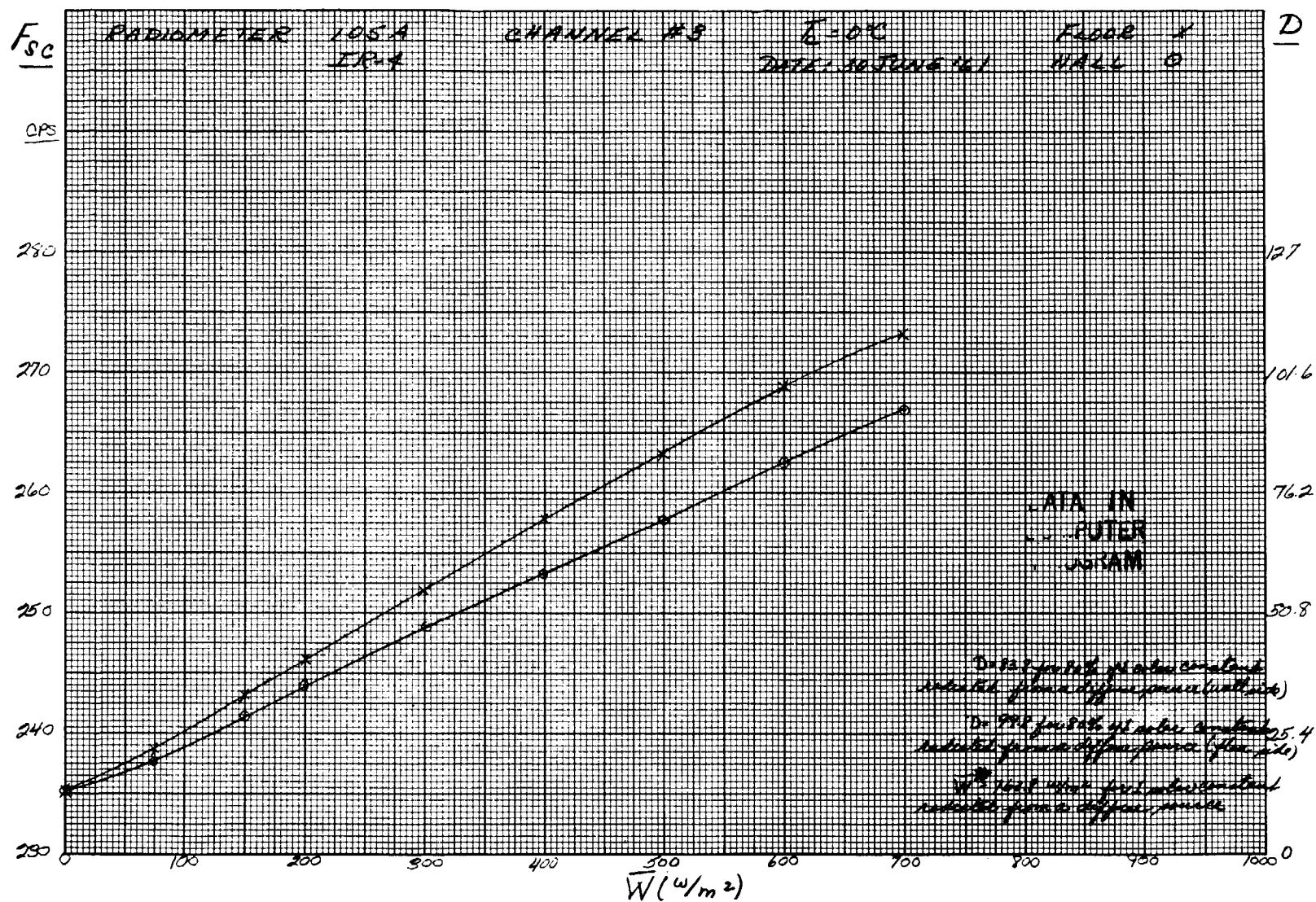


Figure 29—Subcarrier frequency and digital number vs. effective radiant emittance for wall and floor sides, Channel 3.
($T_c = 0^\circ C$)

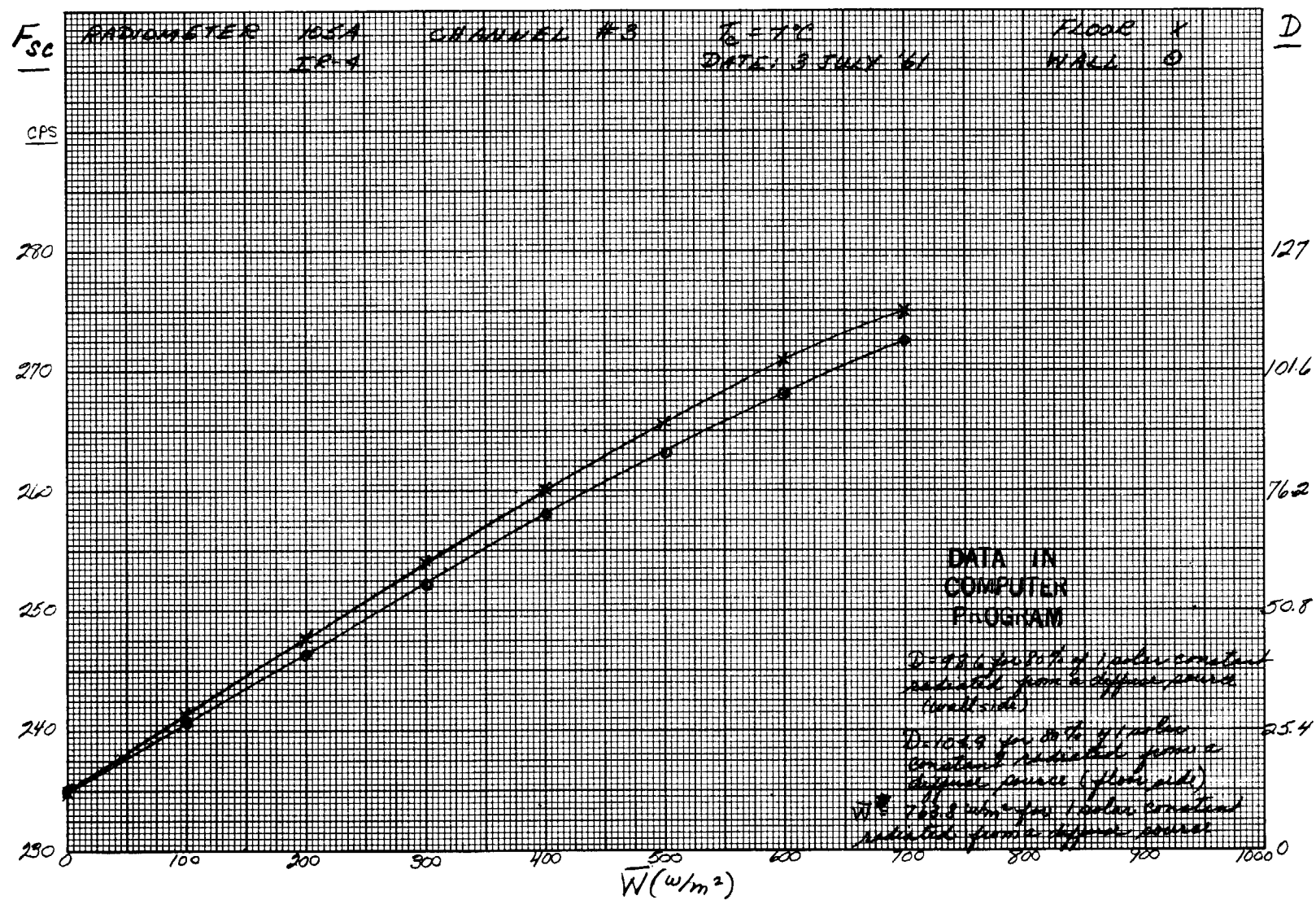


Figure 30—Subcarrier frequency and digital number vs. effective radiant emittance for wall and floor sides, Channel 3.
 $(T_c = 7^\circ\text{C})$

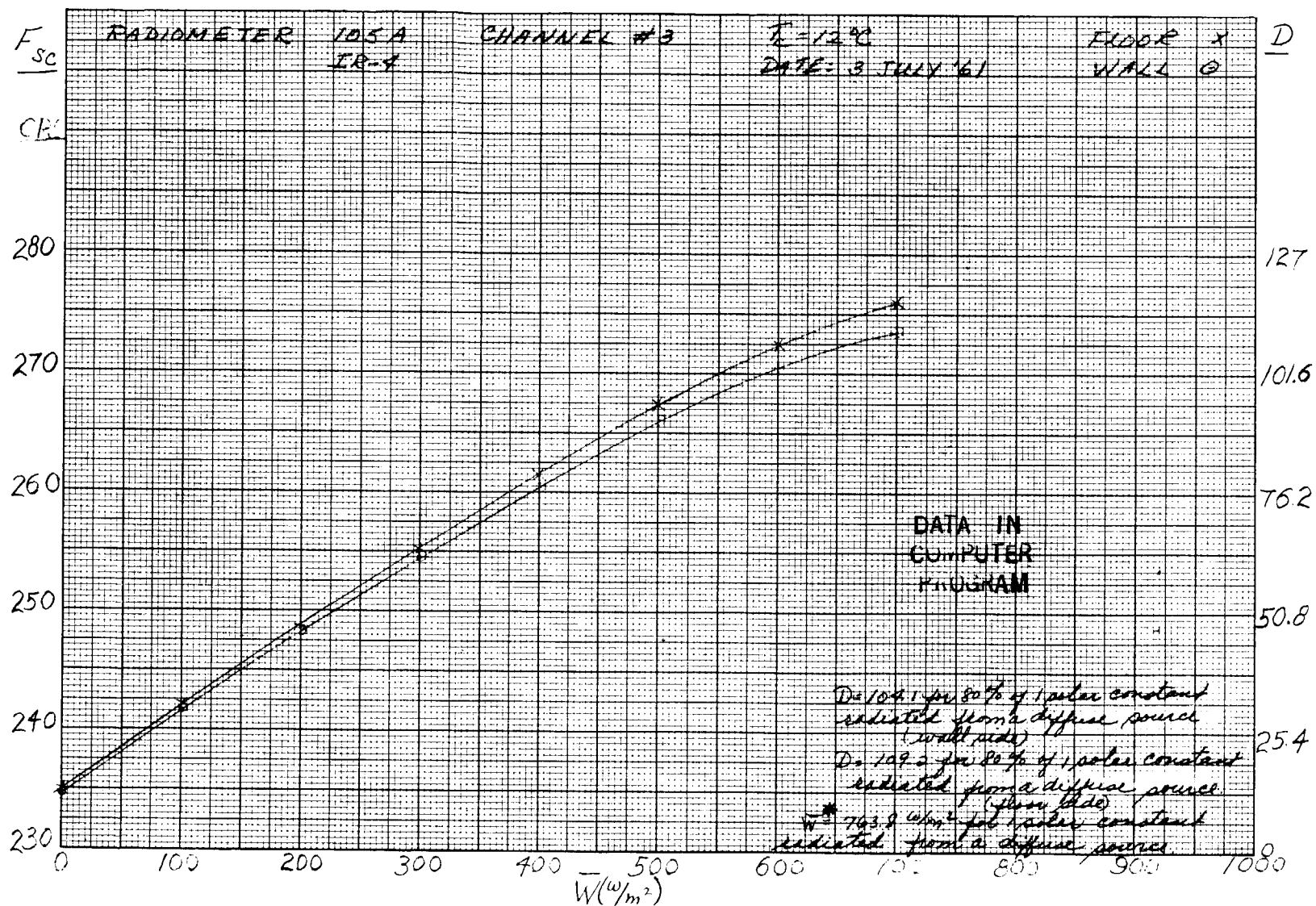


Figure 31—Subcarrier frequency and digital number vs. effective radiant emittance for wall and floor sides, Channel 3.
($T_c = 12^\circ\text{C}$)

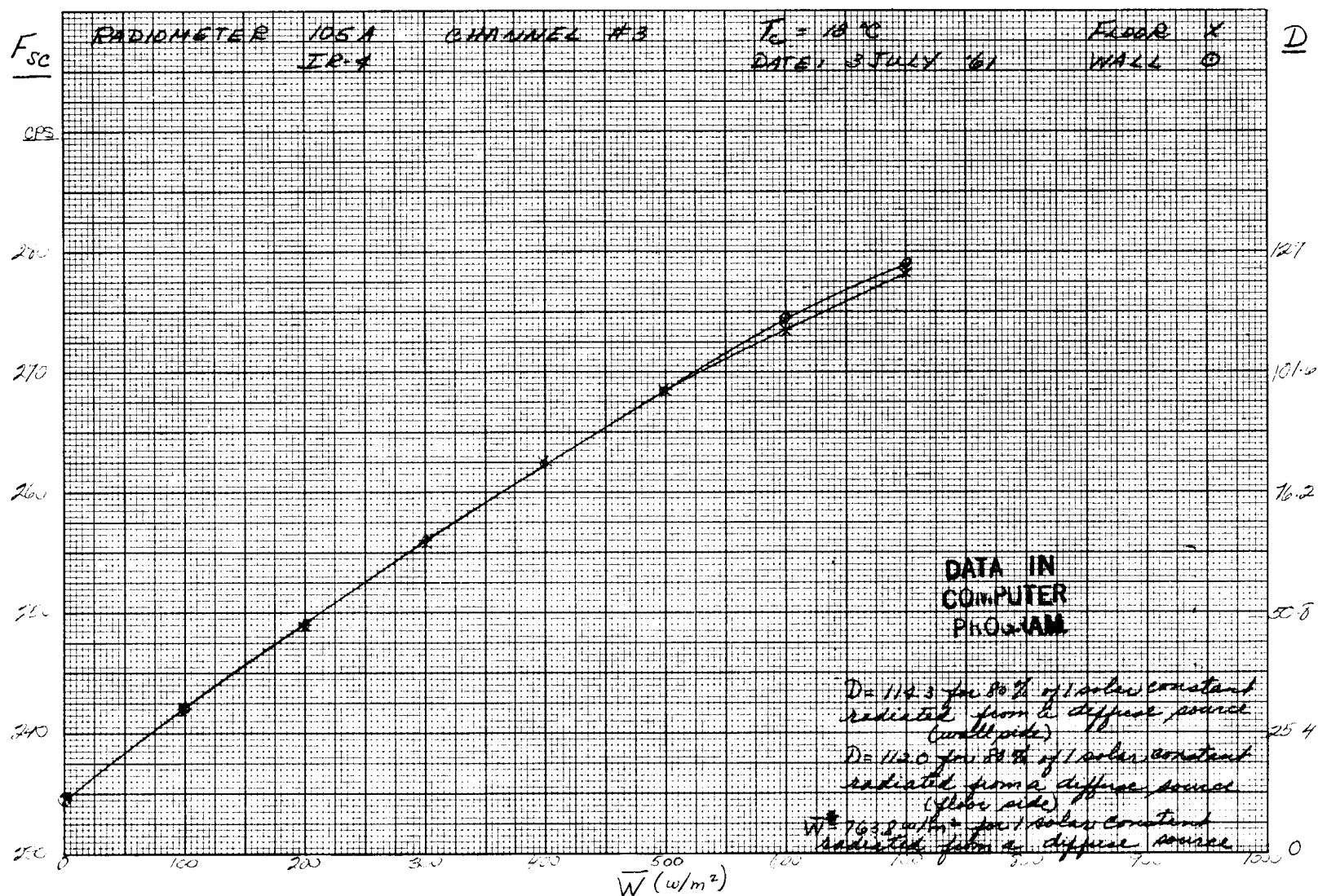


Figure 32—Subcarrier frequency and digital number vs. effective radiant emittance for wall and floor sides, Channel 3.
 $(T_c = 18^\circ\text{C})$

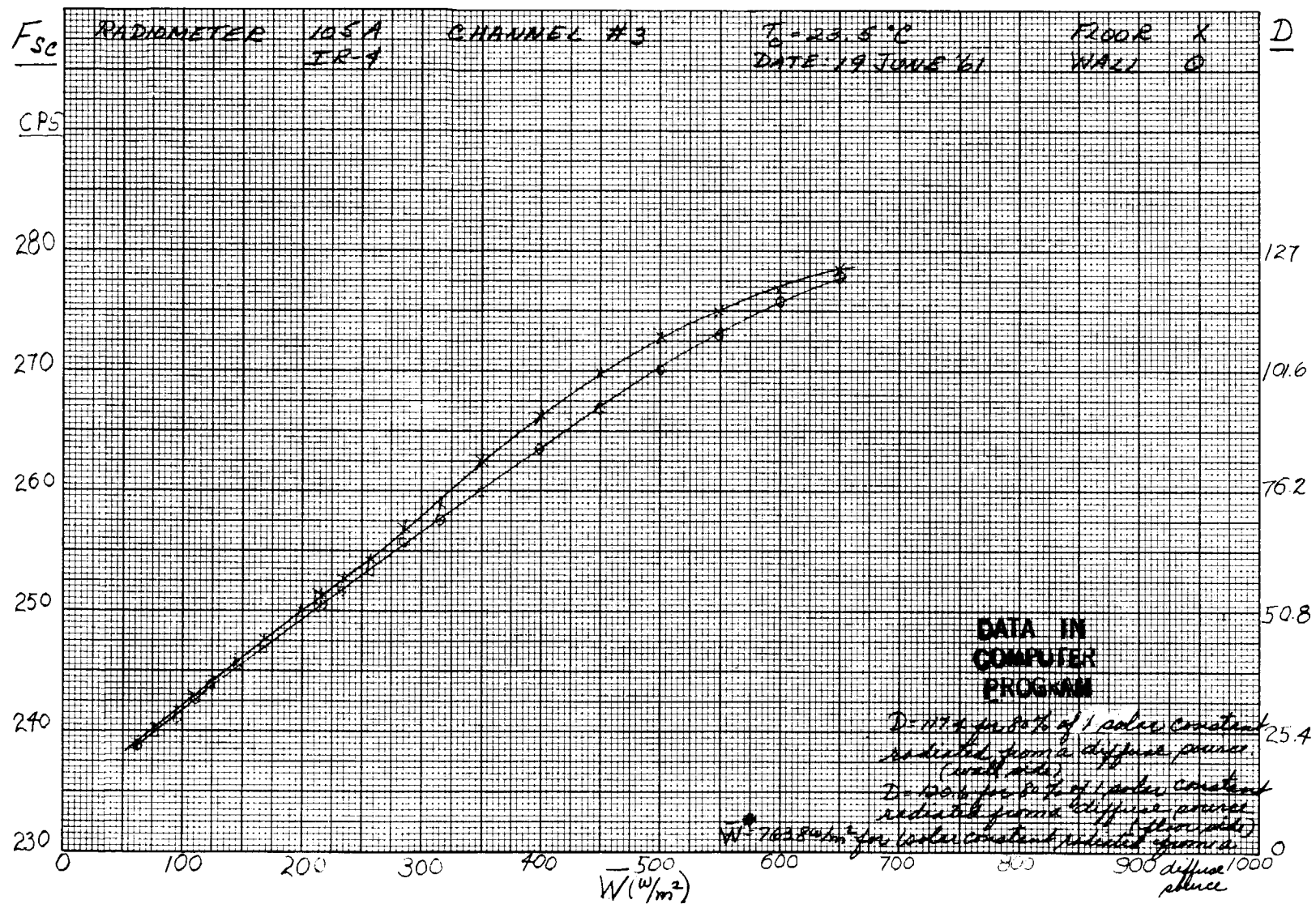


Figure 33—Subcarrier frequency and digital number vs. effective radiant emittance for wall and floor sides, Channel 3.
 $(T_c = 23.5^\circ\text{C})$

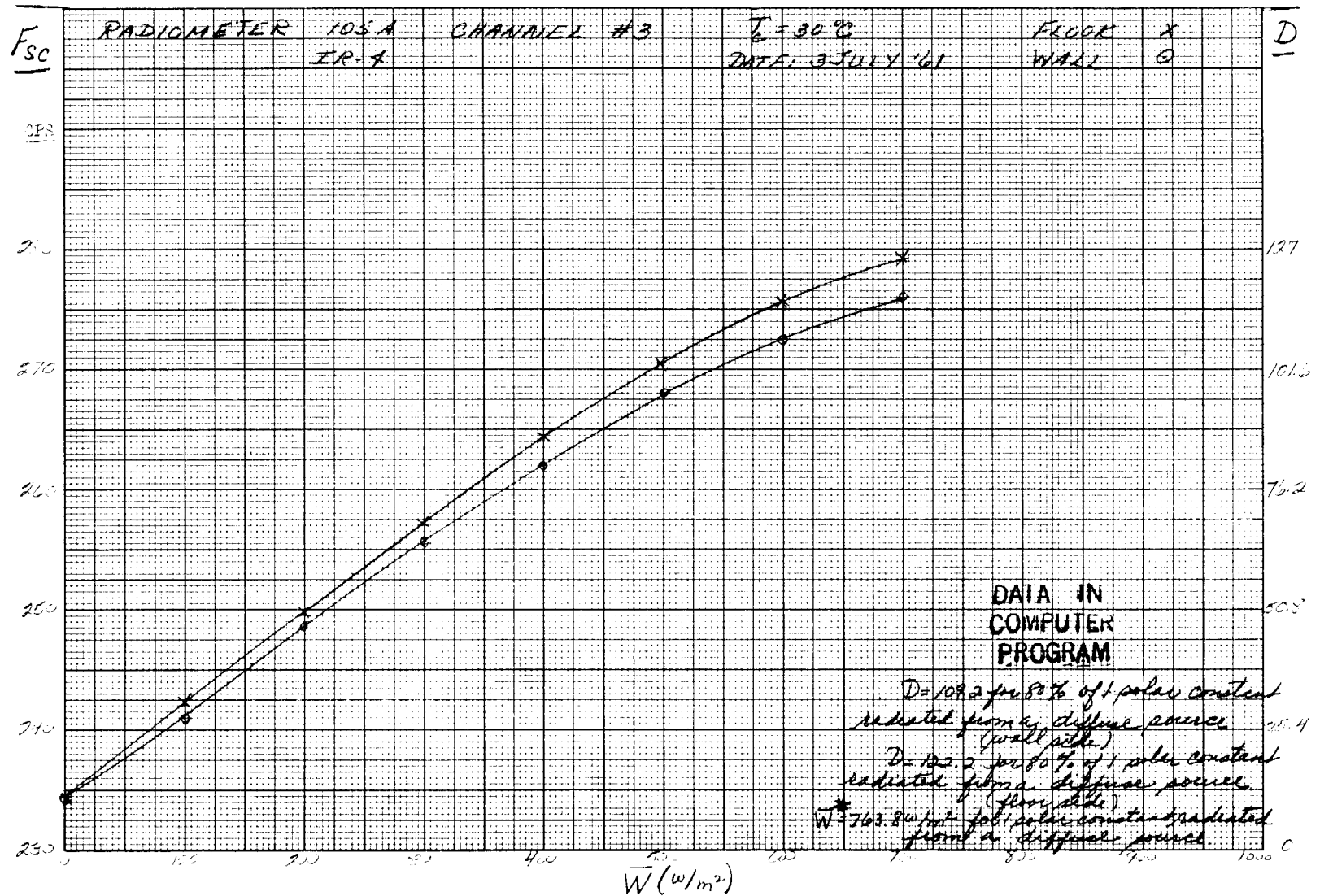


Figure 34—Subcarrier frequency and digital number vs. effective radiant emittance for wall and floor sides, Channel 3.
($T_e = 30^\circ\text{C}$)

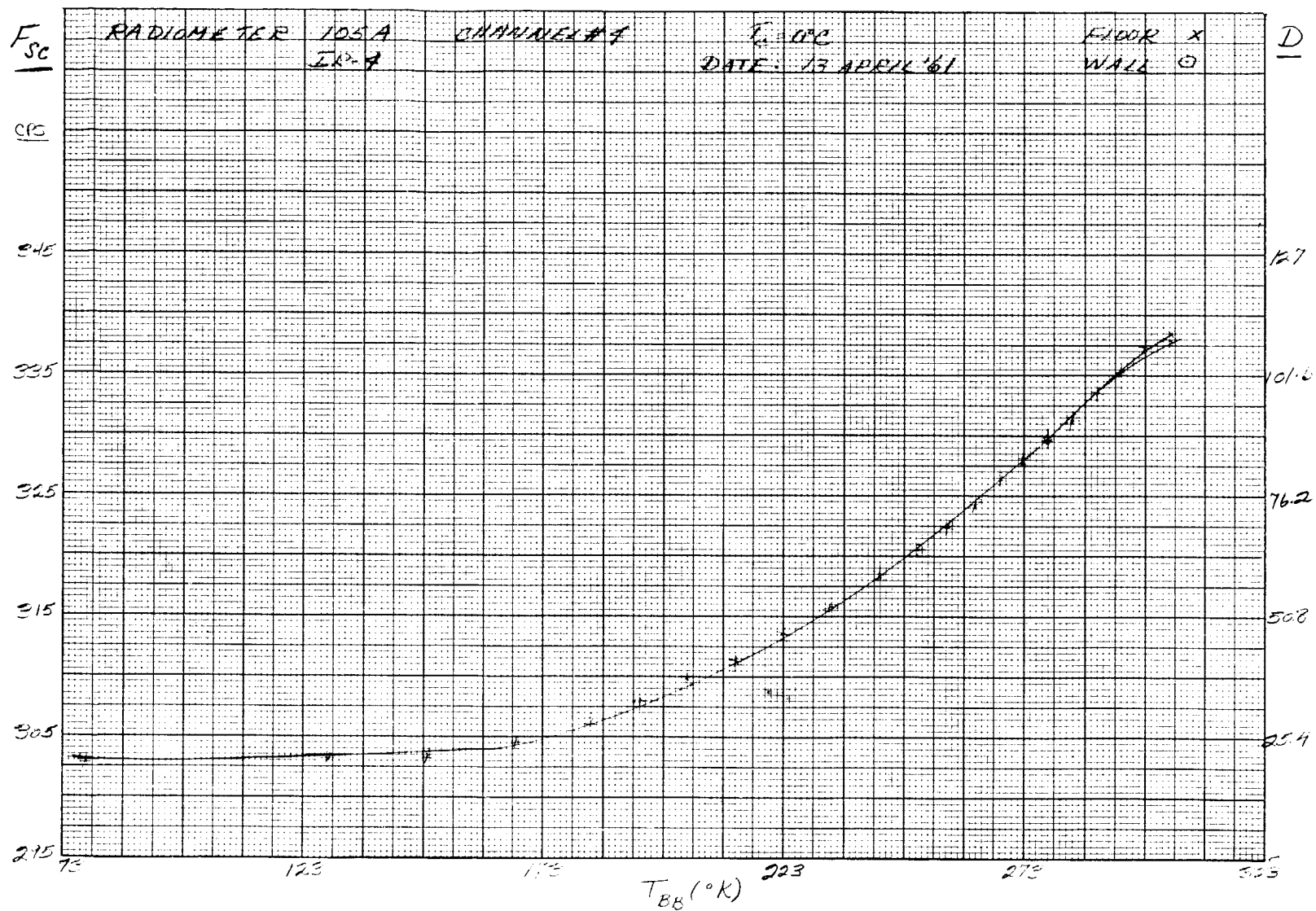


Figure 35—Subcarrier frequency and digital number vs. blackbody temperature for wall and floor sides, Channel 4.
($T_c = 0^\circ\text{C}$)

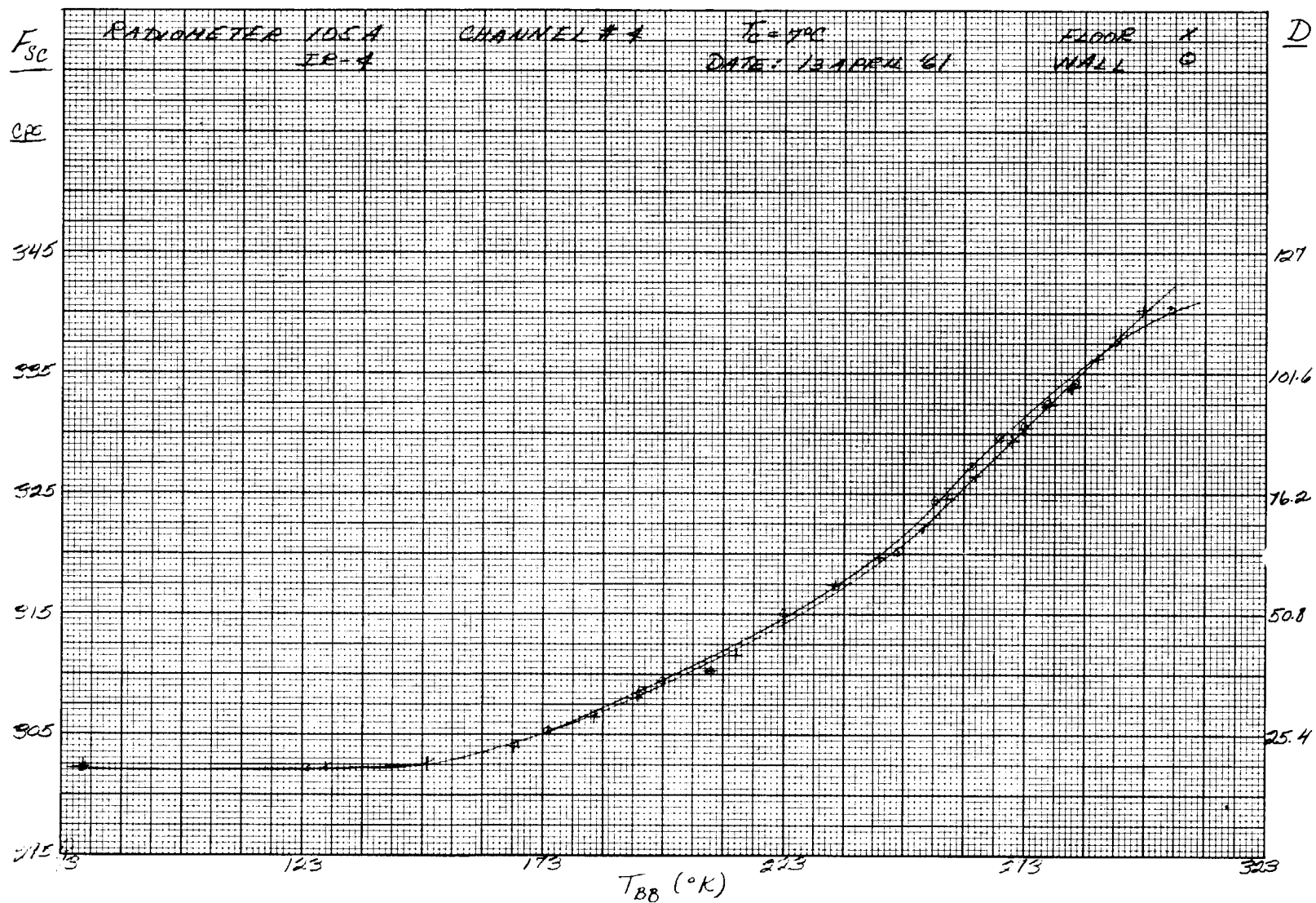


Figure 36—Subcarrier frequency and digital number vs. blackbody temperature for wall and floor sides, Channel 4.
 $(T_c = 7^{\circ}\text{C})$

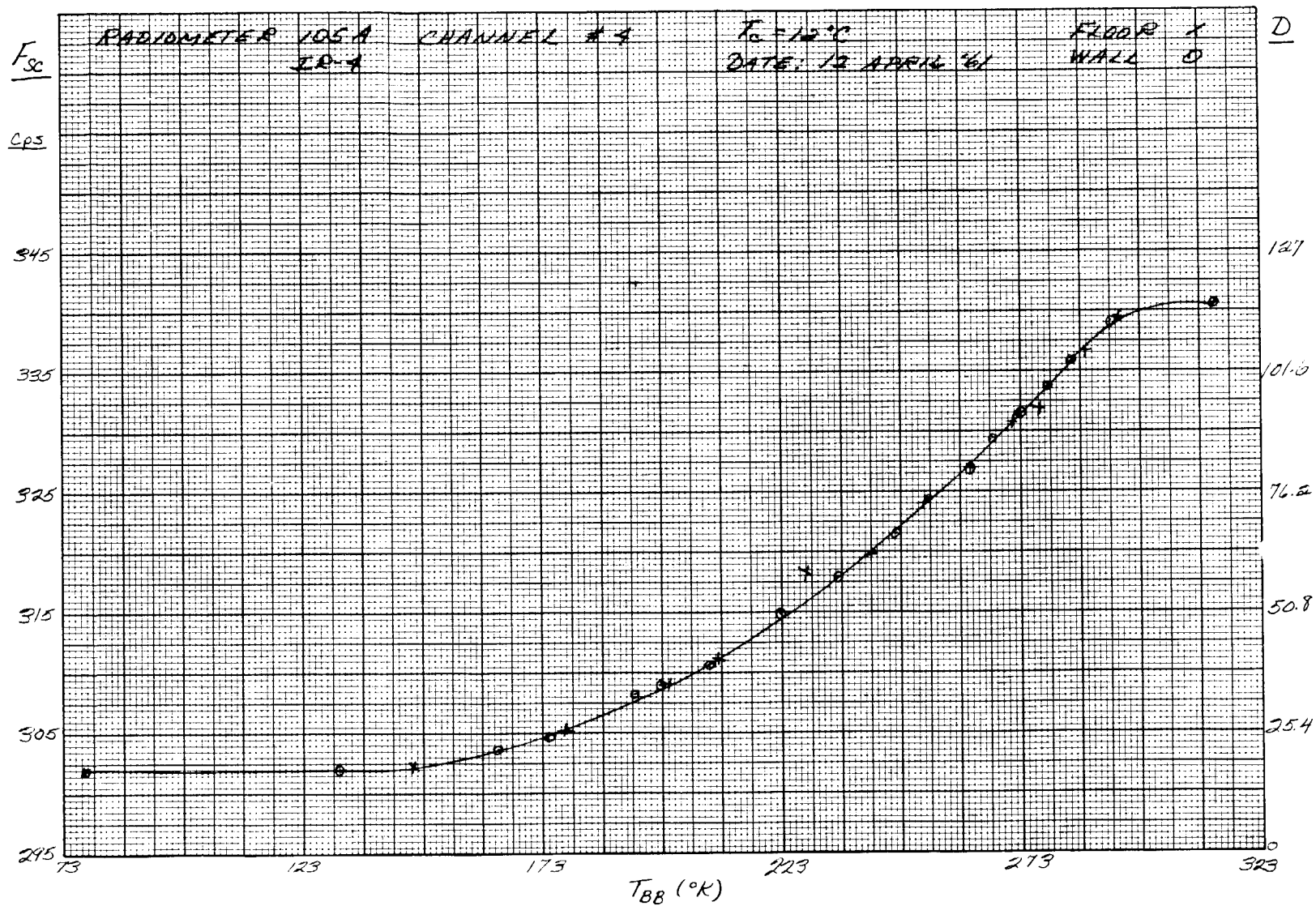


Figure 37—Subcarrier frequency and digital number vs. blackbody temperature for wall and floor sides, Channel 4.
 ($T_c = 12^\circ\text{C}$)

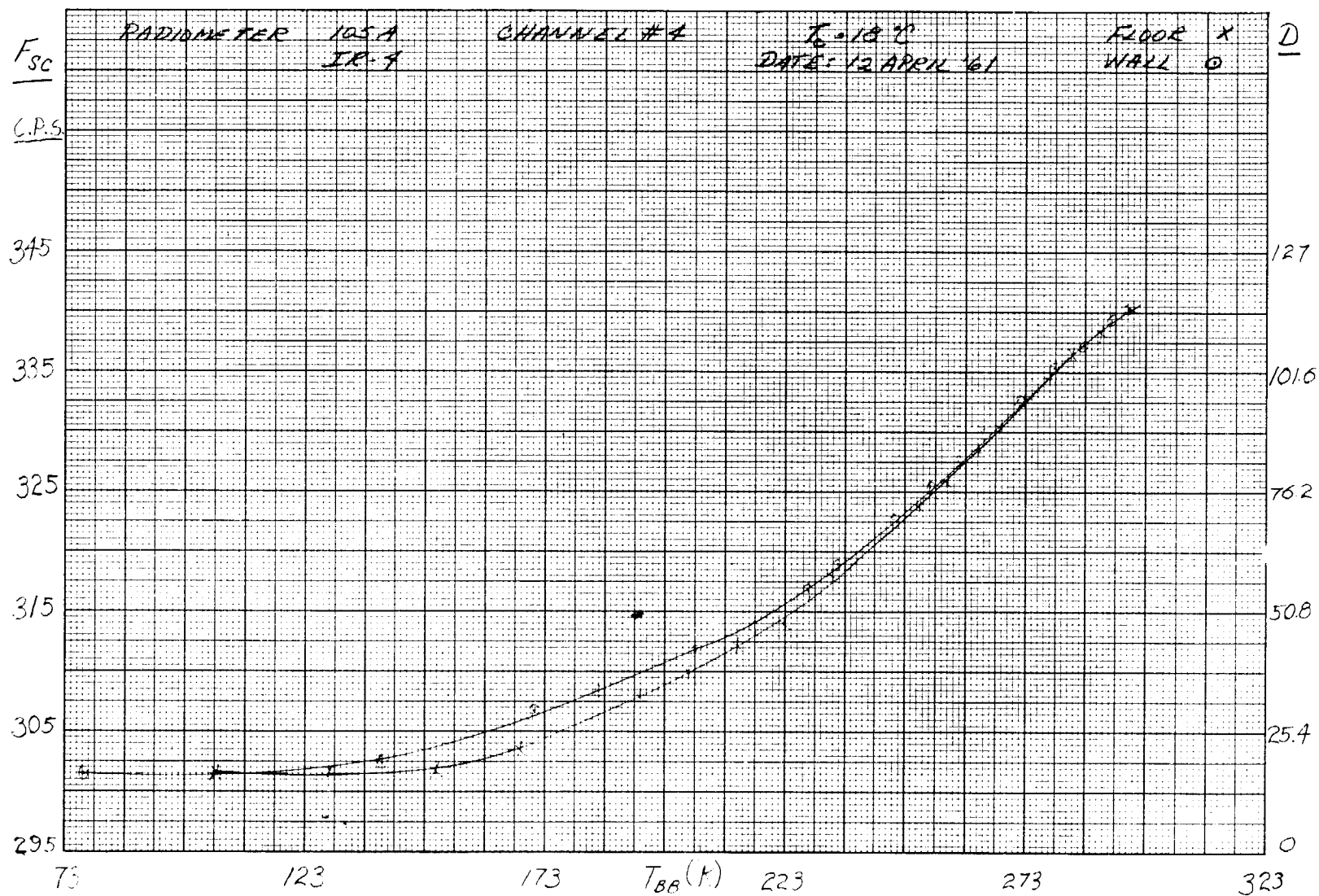


Figure 38—Subcarrier frequency and digital number vs. blackbody temperature for wall and floor sides, Channel 4.
($T_c = 18^\circ\text{C}$)

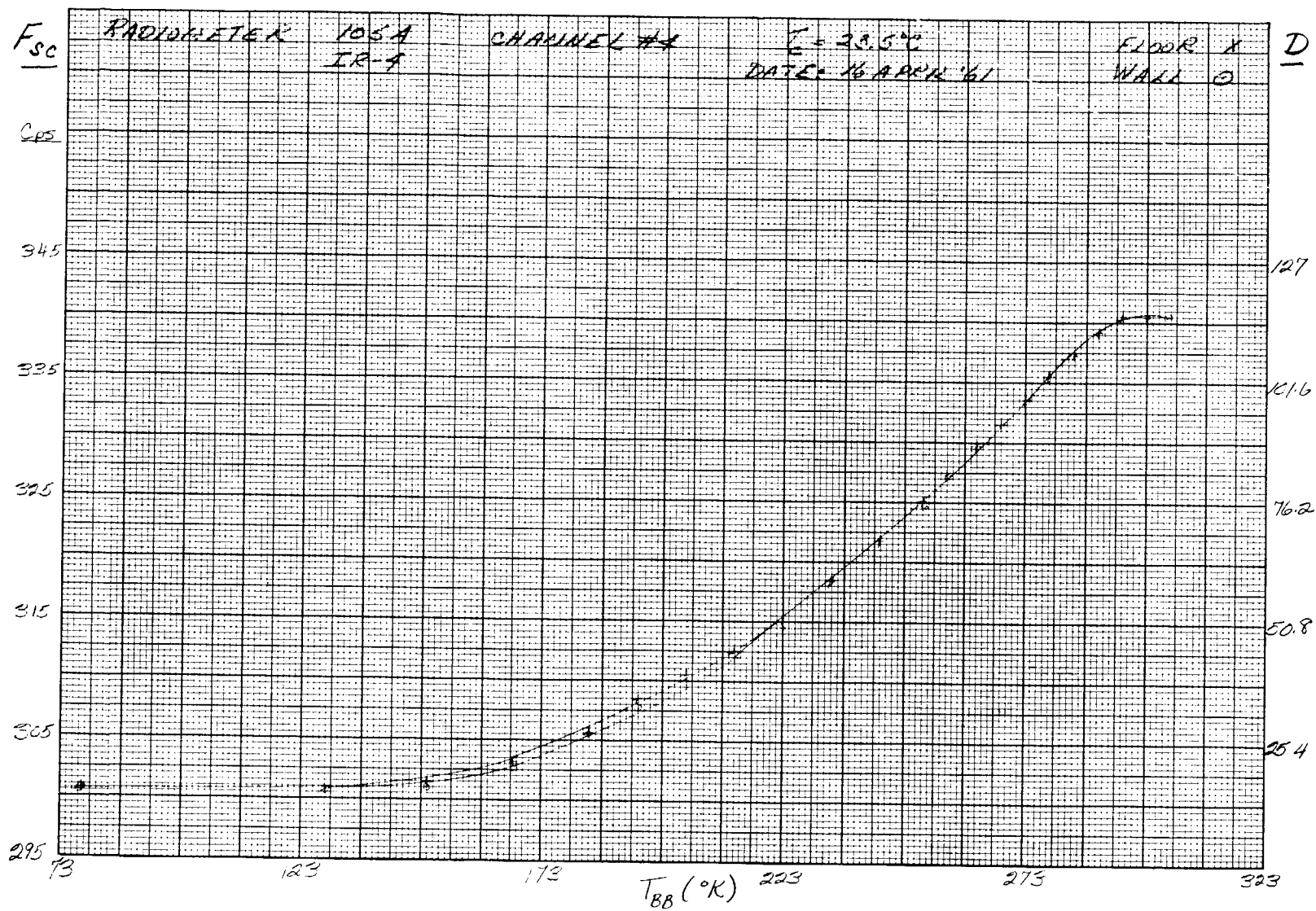


Figure 39—Subcarrier frequency and digital number vs. blackbody temperature for wall and floor sides, Channel 4.
 $(T_c = 23.5^\circ\text{C})$

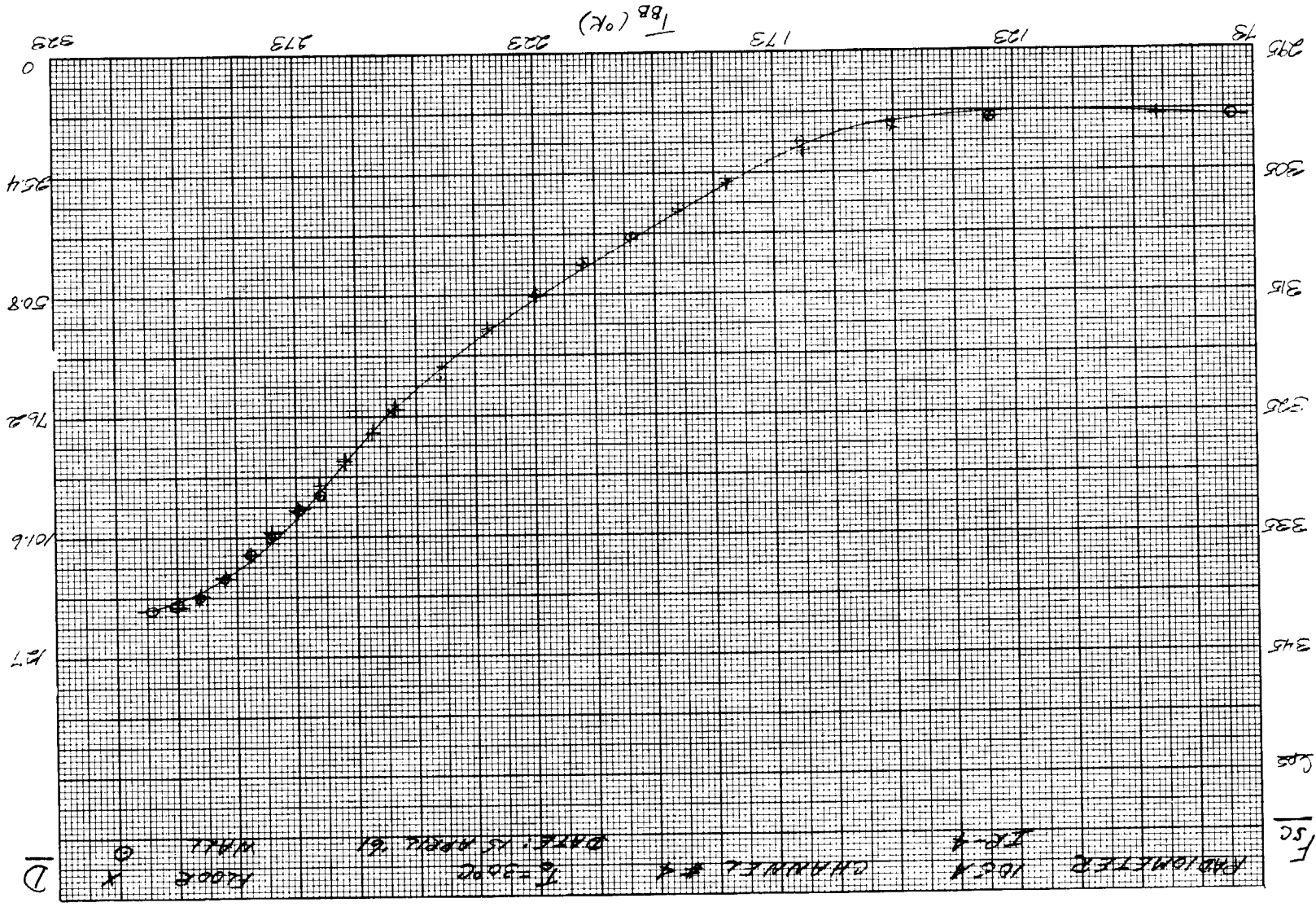


Figure #0—Subcarrier frequency and digital number vs. blackbody temperature for wall and floor sides, Channel 4.
 $(T_c = 30^{\circ}C)$

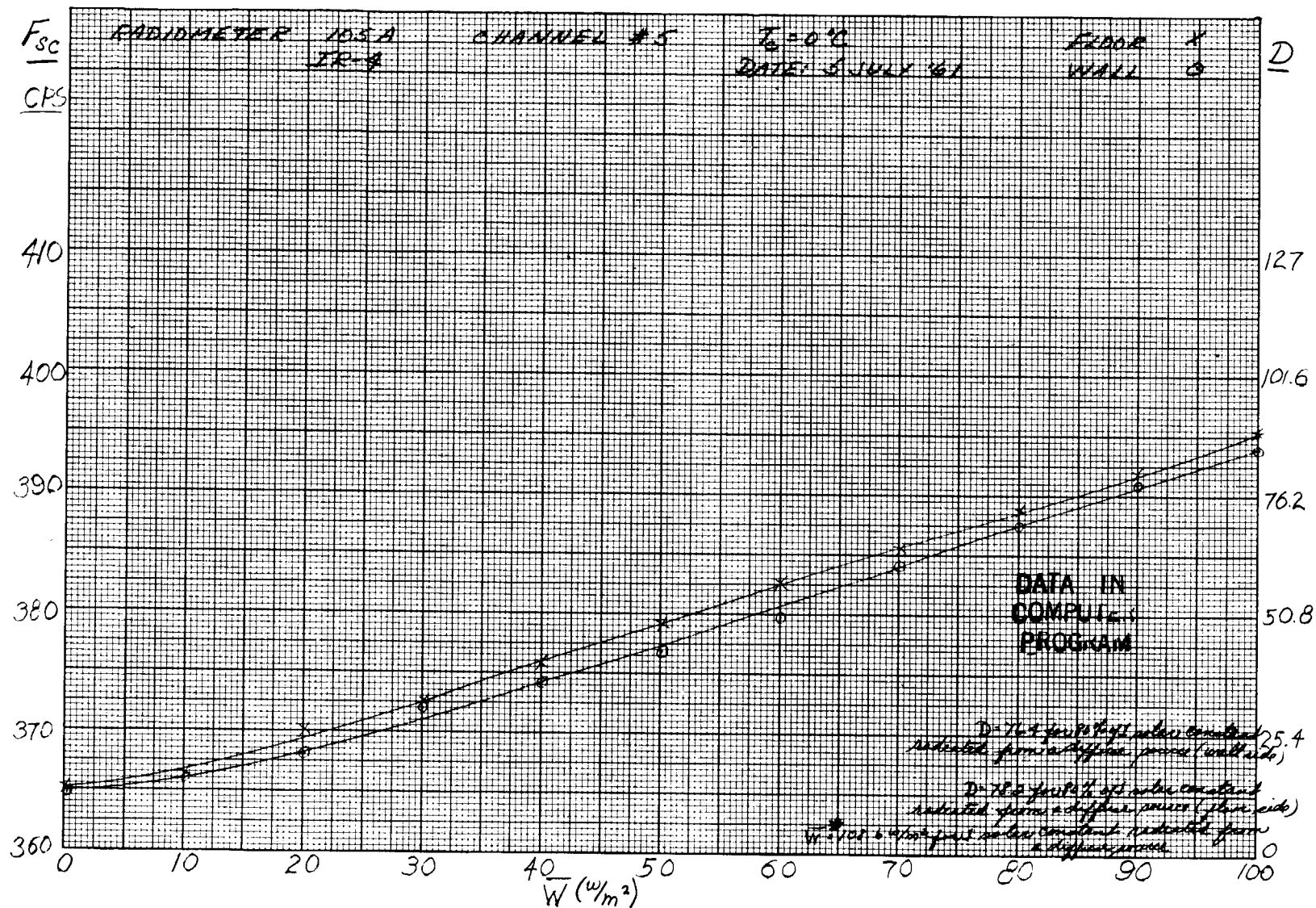


Figure 41—Subcarrier frequency and digital number vs. effective radiant emittance for wall and floor sides, Channel 5.
 ($T_c = 0^\circ C$)

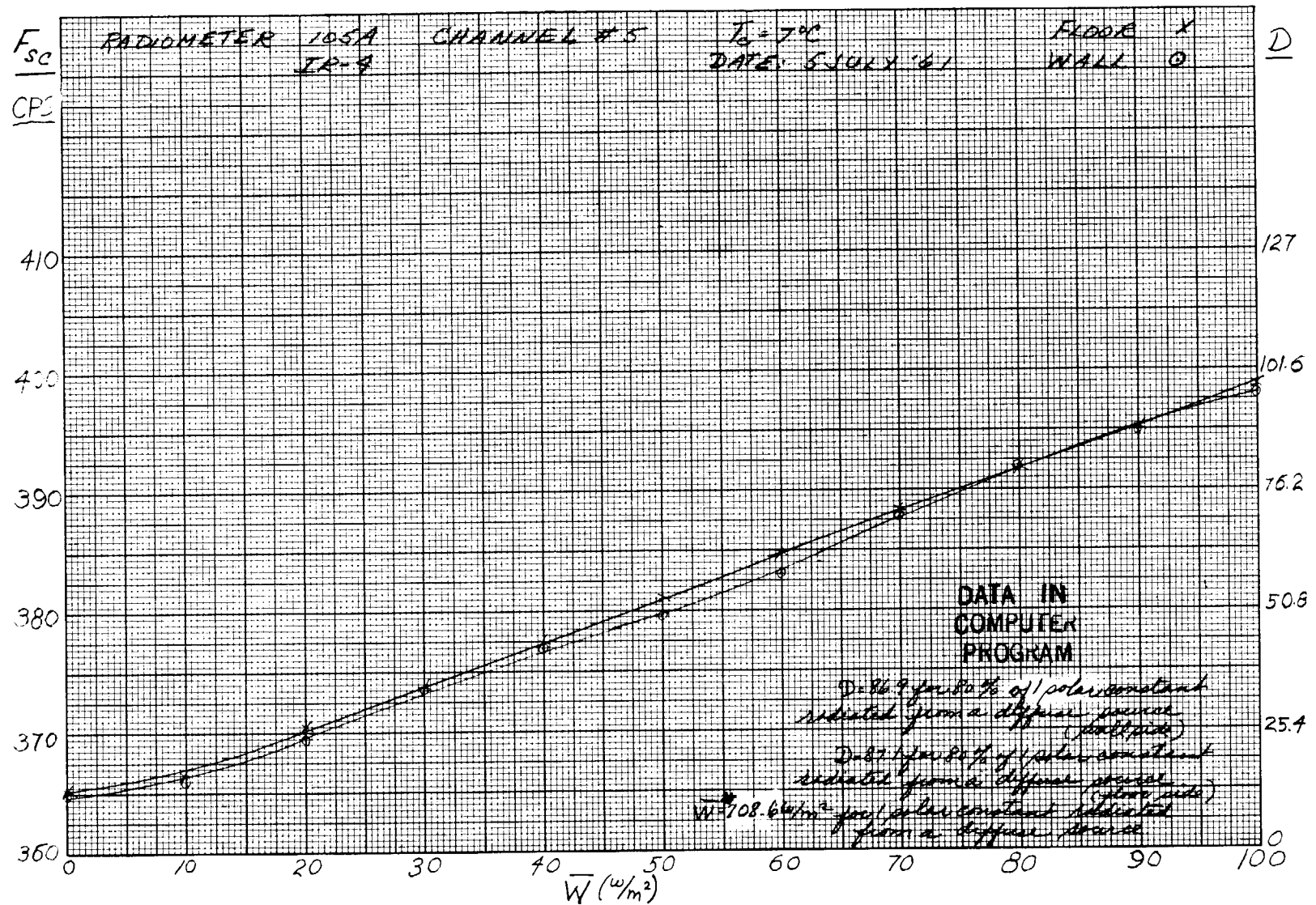
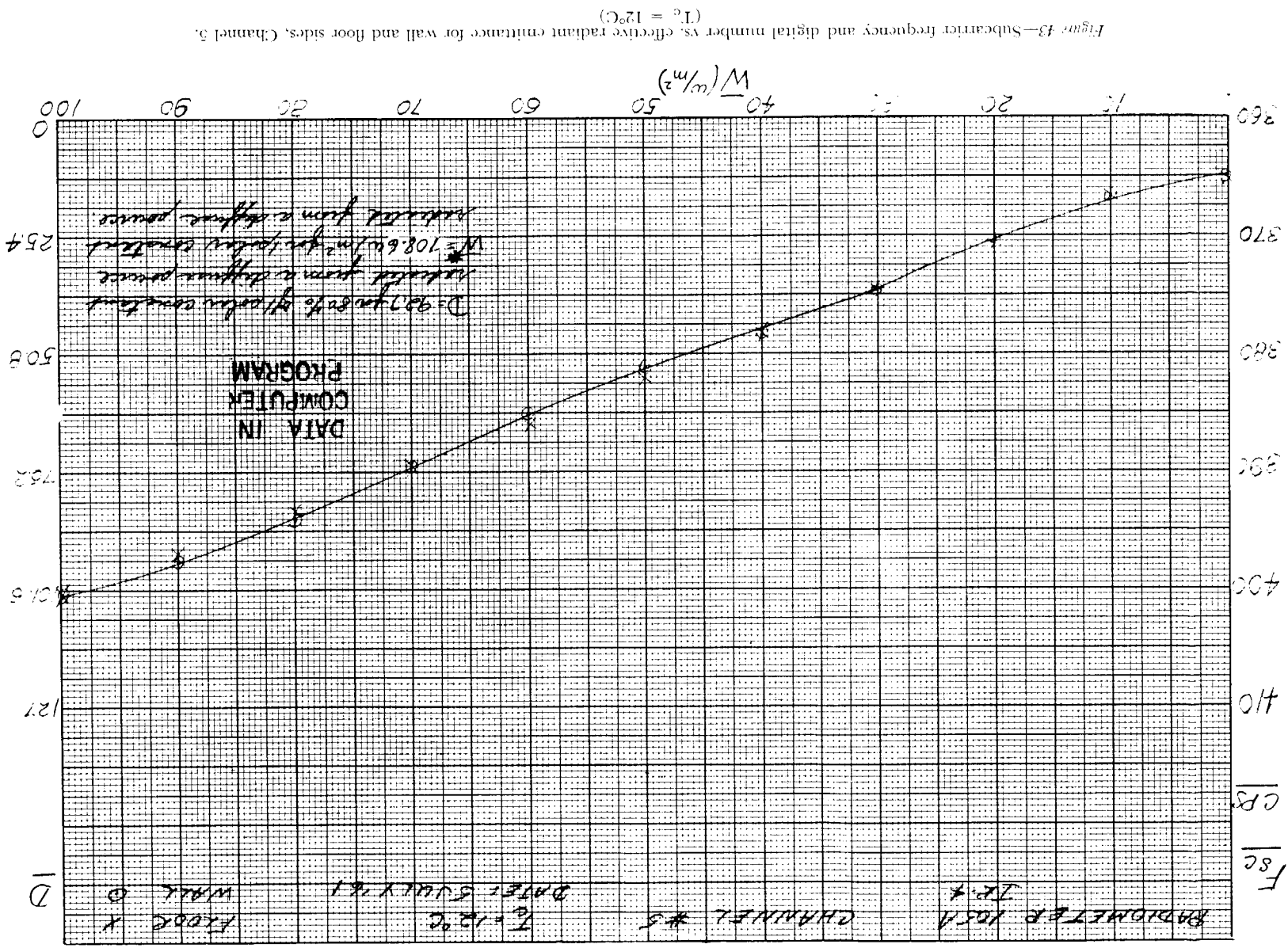


Figure 42—Subcarrier frequency and digital number vs. effective radiant emittance for wall and floor sides, Channel 5.
 $(T_0 = 7^\circ\text{C})$



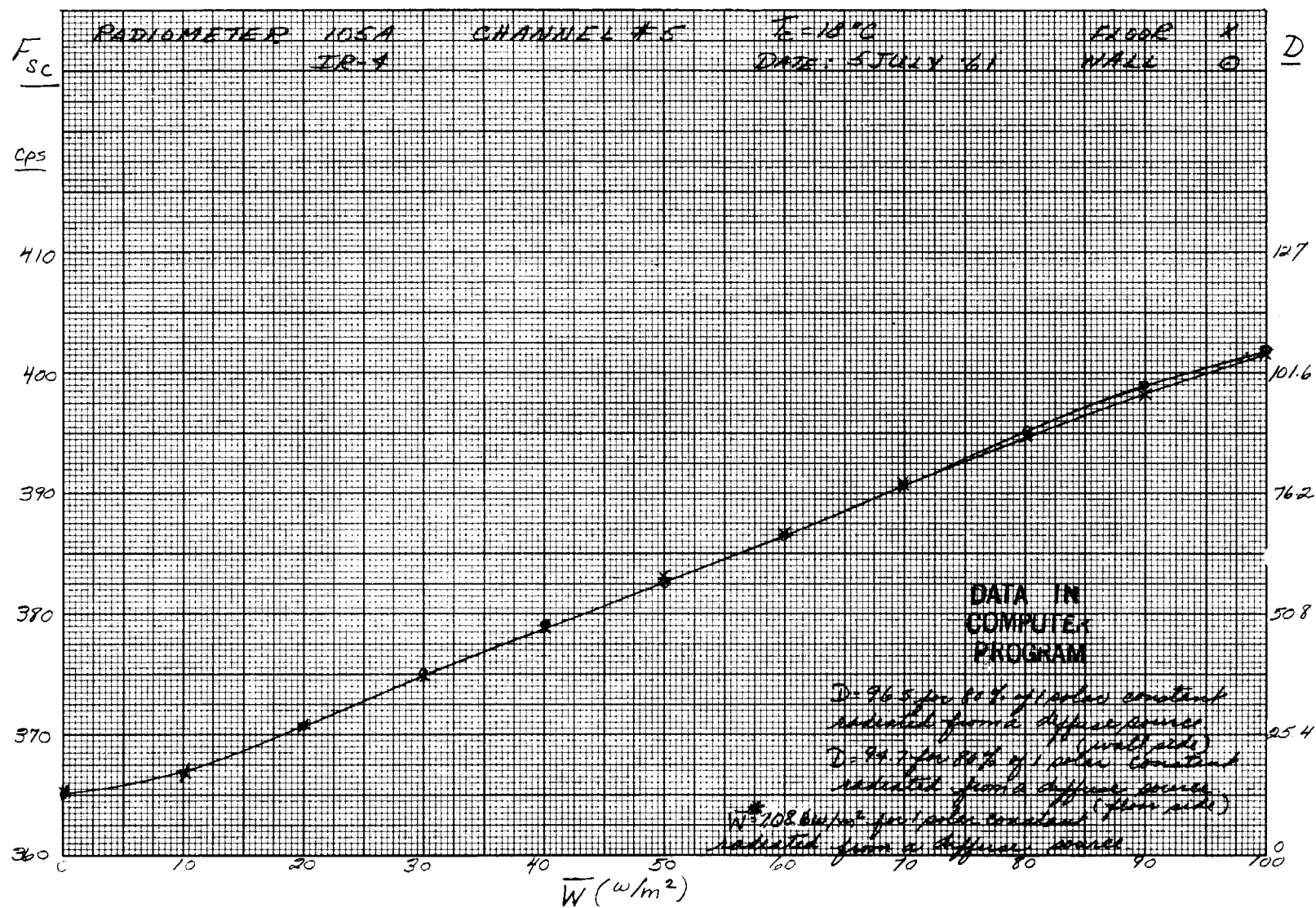


Figure 44—Subcarrier frequency and digital number vs. effective radiant emittance for wall and floor sides, Channel 5.
 $(T_c = 18^\circ\text{C})$

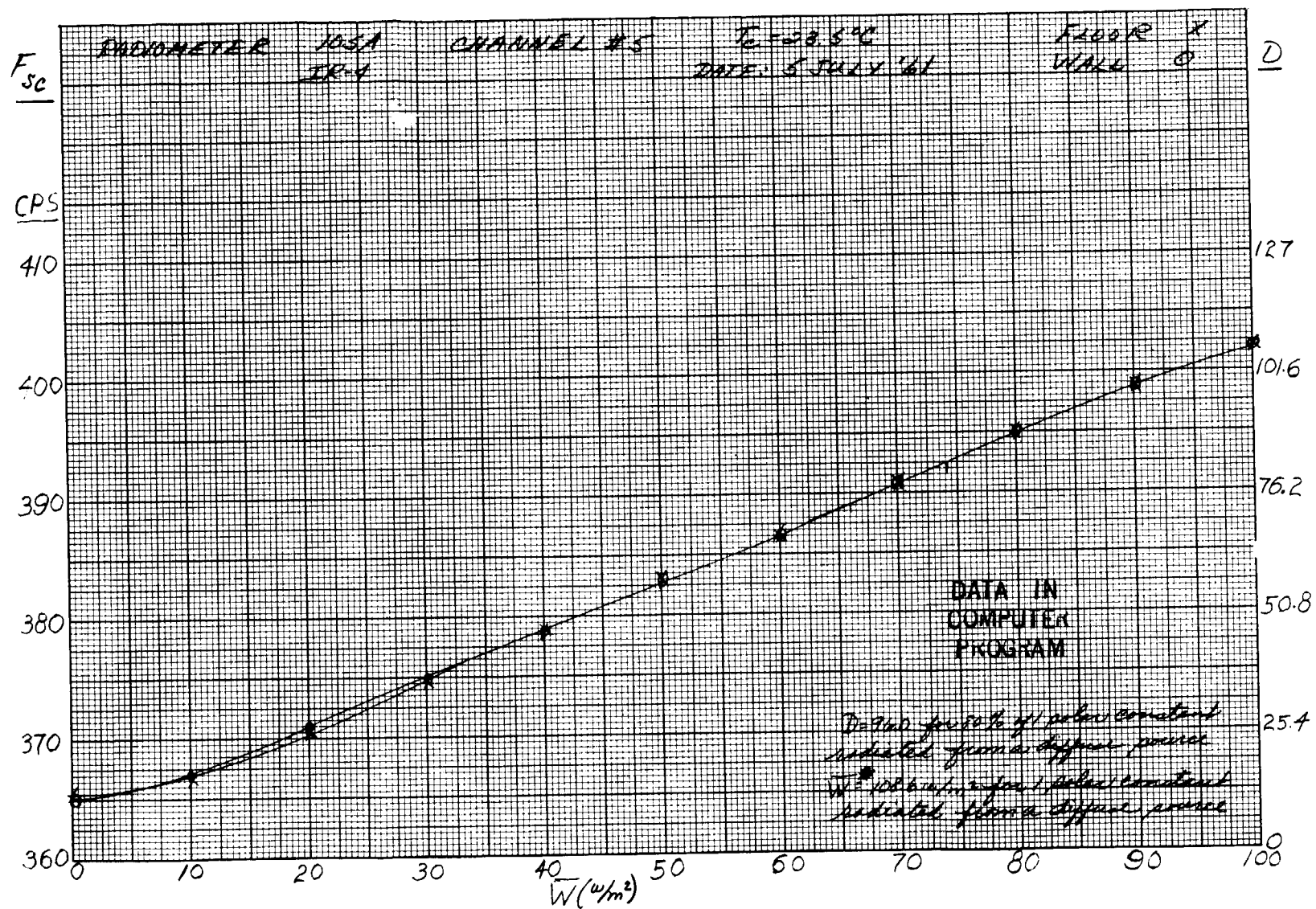


Figure 45—Subcarrier frequency and digital number vs. effective radiant emittance for wall and floor sides, Channel 5.
($T_c = 23.5^\circ\text{C}$)

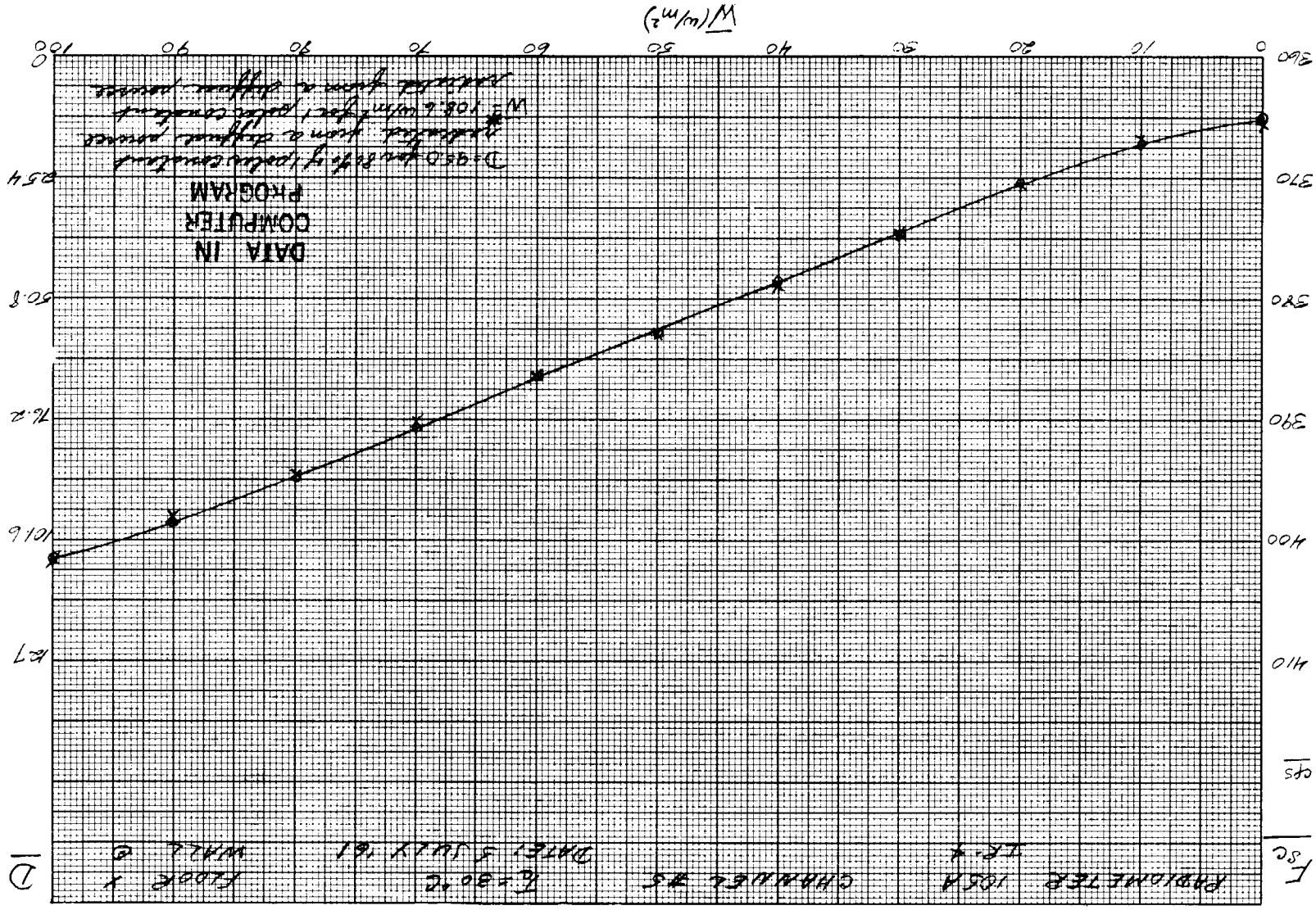
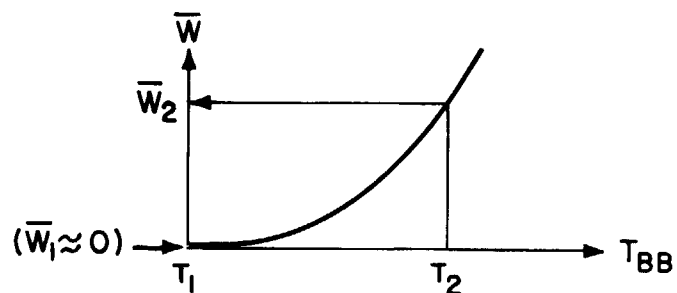


Figure 46—Subcarrier frequency and digital number vs. effective radiant emittance for wall and floor sides, Channel 5.
 $(T_c = 30.2^\circ C)$

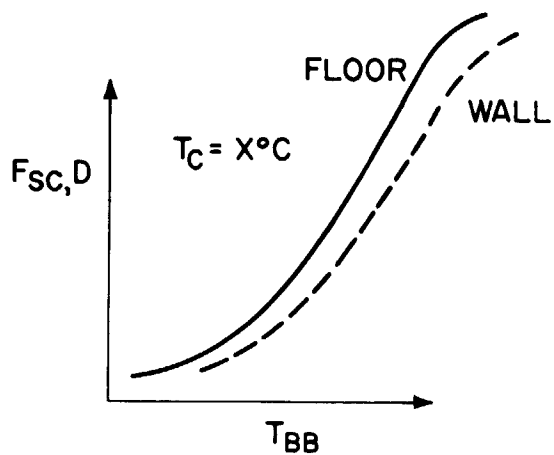
THERMAL CHANNELS 1, 2, AND 4



REFERENCE TARGET AT TEMPERATURE

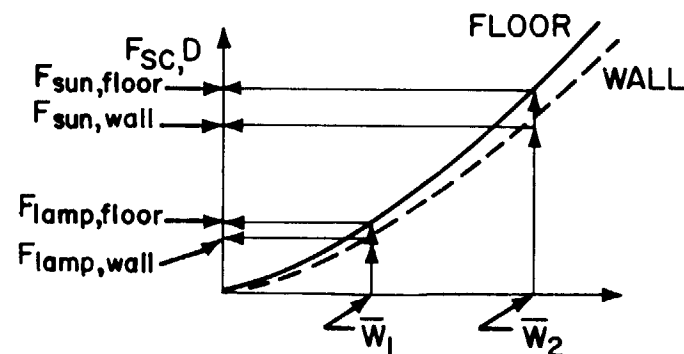
T_1 (-196°C)

"HOT" TARGET AT TEMPERATURE T_2



(a)

VISIBLE CHANNELS 3 AND 5



DIFFUSE SOURCE :

$$\bar{W} = \frac{\cos \gamma}{R^2} \int_0^\infty J_\lambda \phi_\lambda r_\lambda d\lambda$$

SUN AT NORMAL INCIDENCE ON
SURFACE OF UNIT REFLECTIVITY

$$\bar{W}^* = \frac{\Omega}{\Pi} \int_0^\infty W_\lambda (T=5800^\circ\text{K}) \phi_\lambda d\lambda$$

(b)

Figure 47—(a) Calibration of the thermal Channels 1, 2, and 4.
(b) Calibration of the visible Channels 3 and 5.

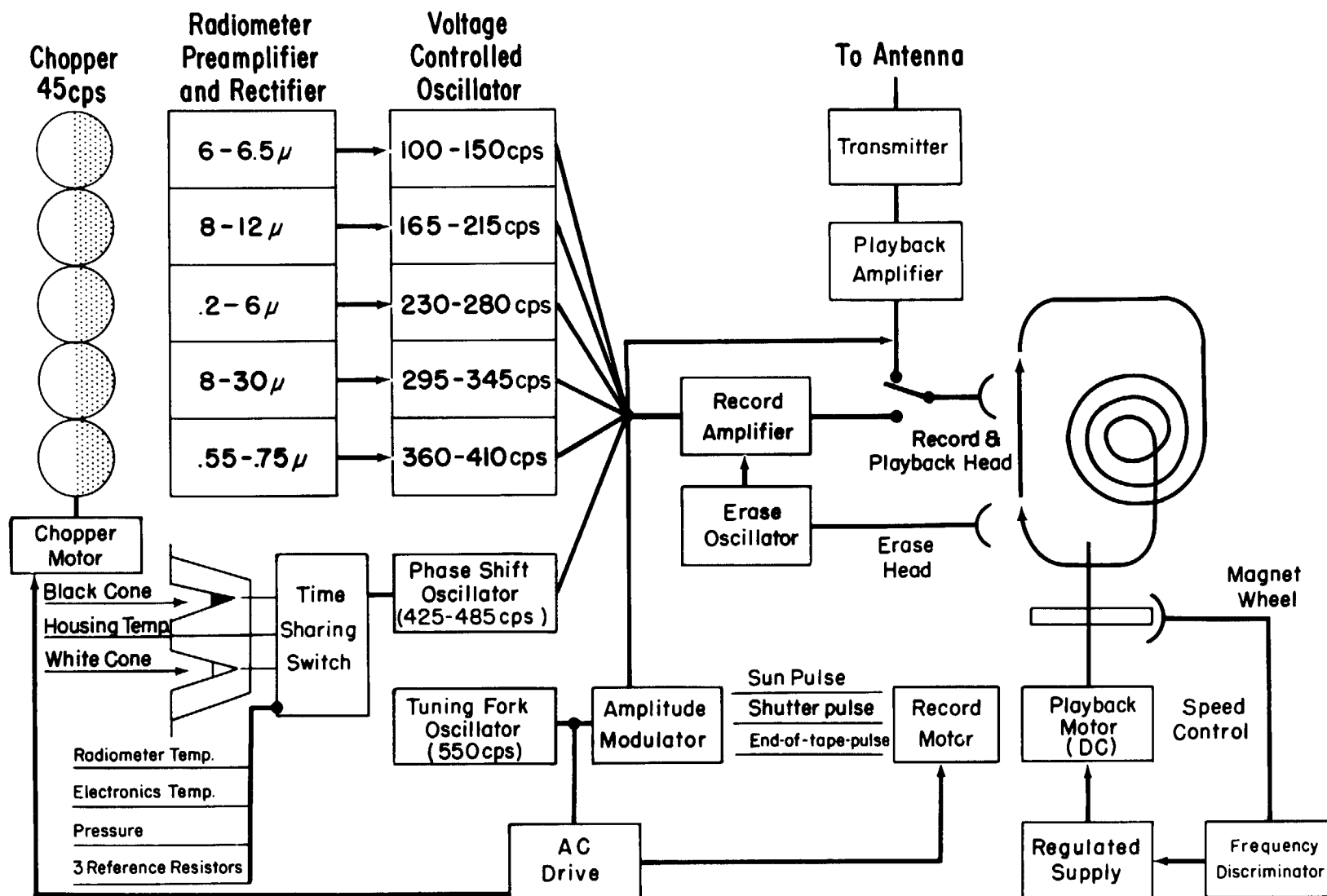
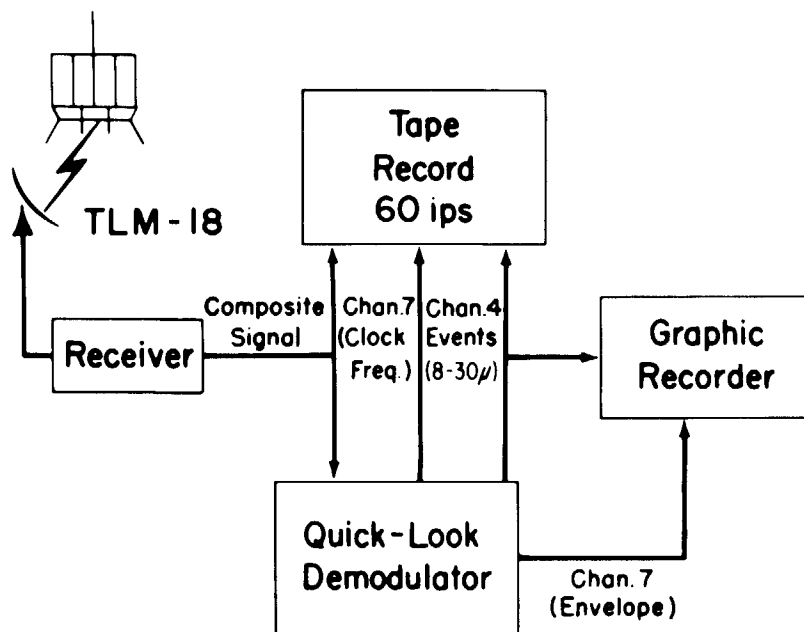
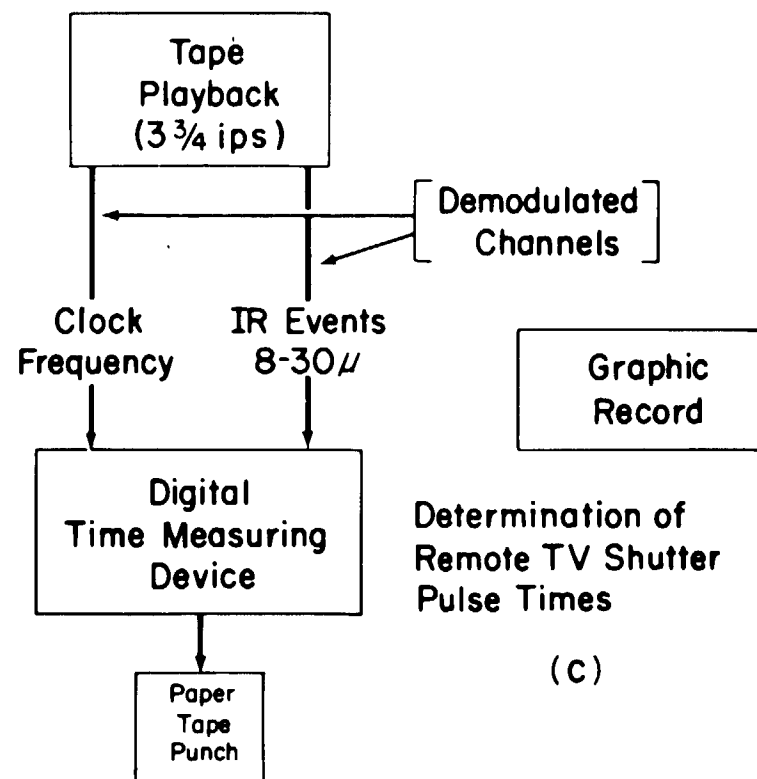


Figure 48—Block diagram of the radiation experiment in the satellite.



(a)



(b)

Attitude Data Transmitted
via Teletypewriter to Tiro's
Control Center, Wash., D.C.

Figure 49—Block diagram of information flow at a data acquisition station including auxiliary uses of the radiation data.

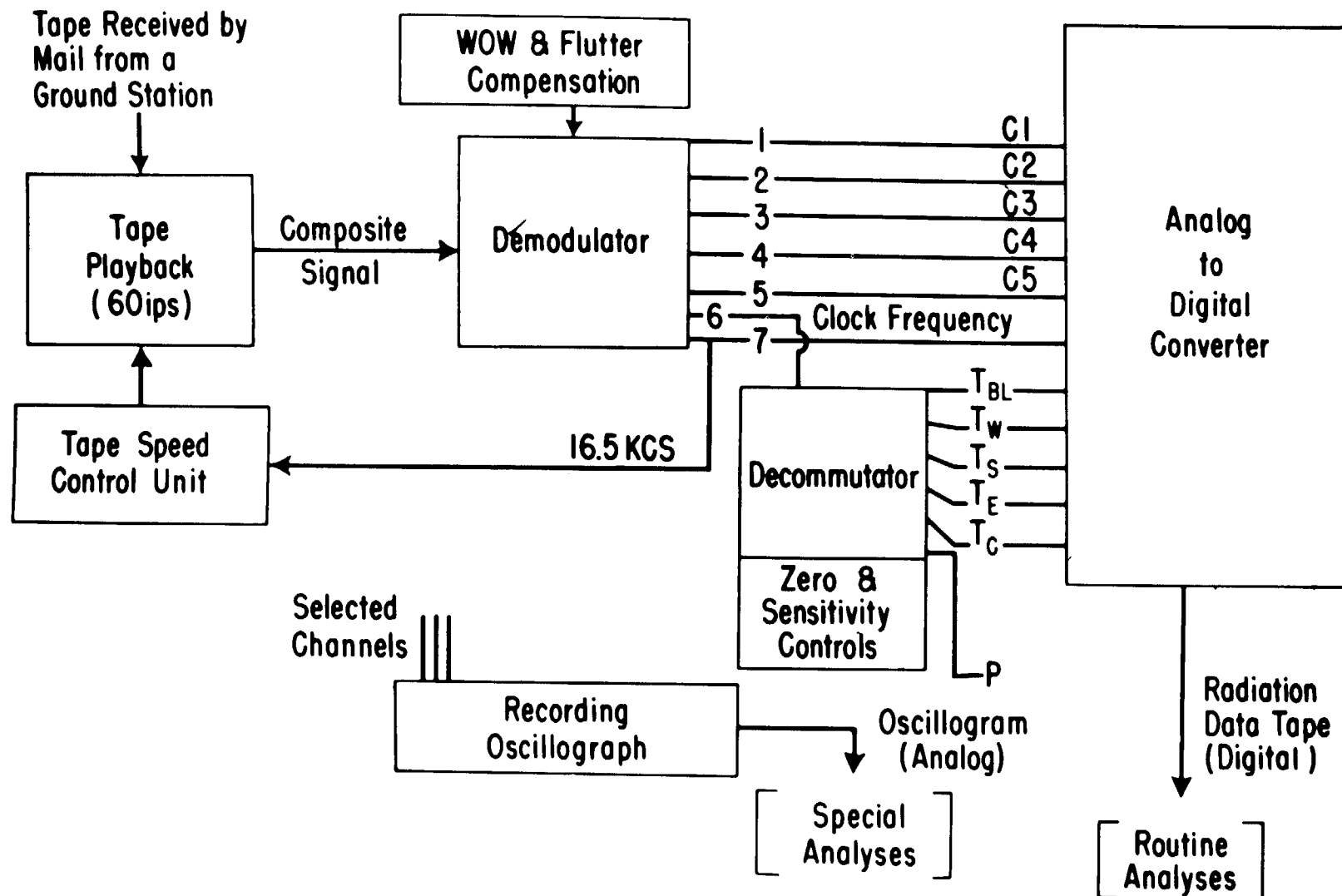


Figure 50—Block diagram of information flow at the data reduction center in producing a digital magnetic tape for computer input.

ONE FILE (ONE ORBIT)

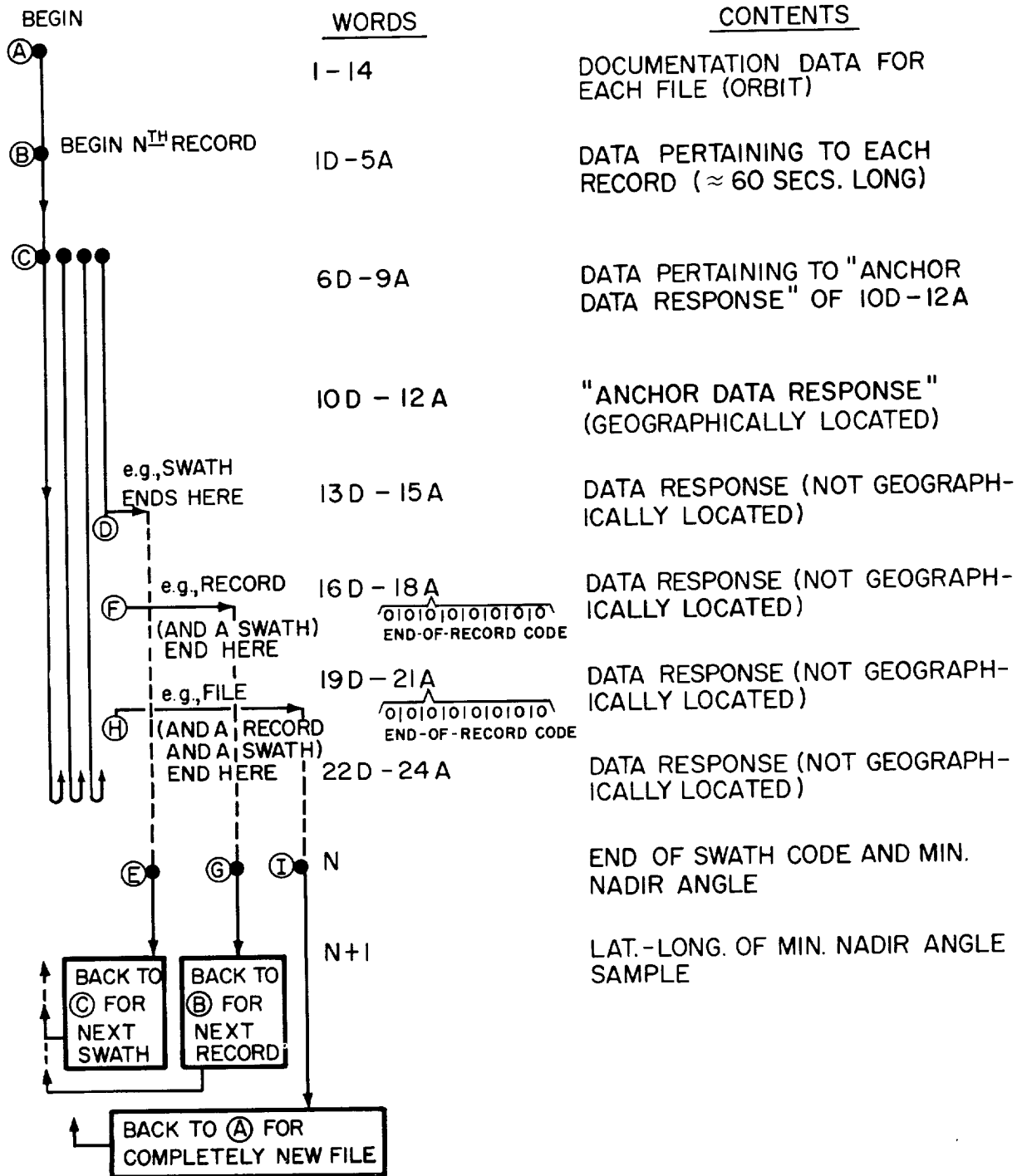


Figure 51—Diagram for interpretation of FMR tape format.

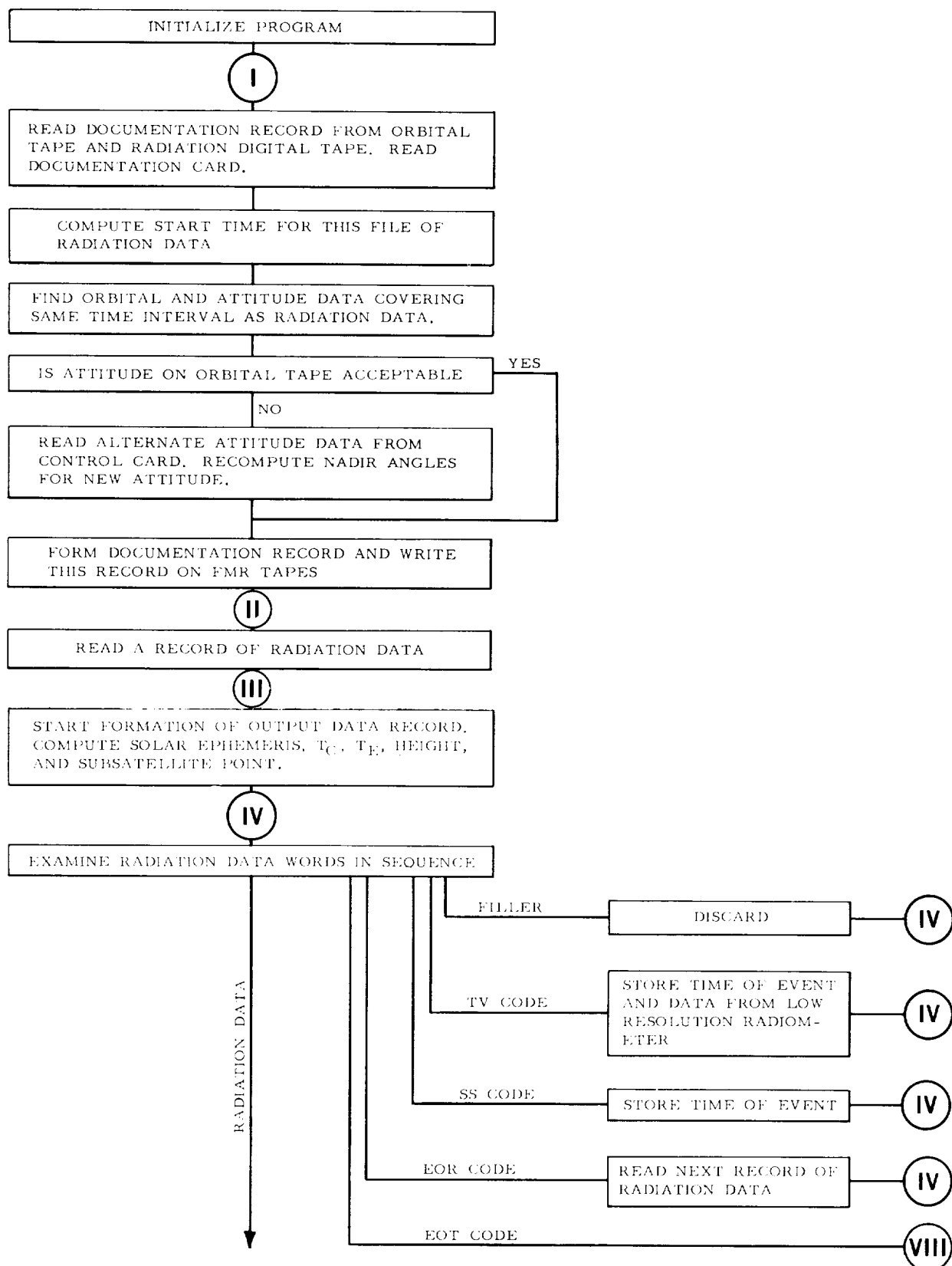
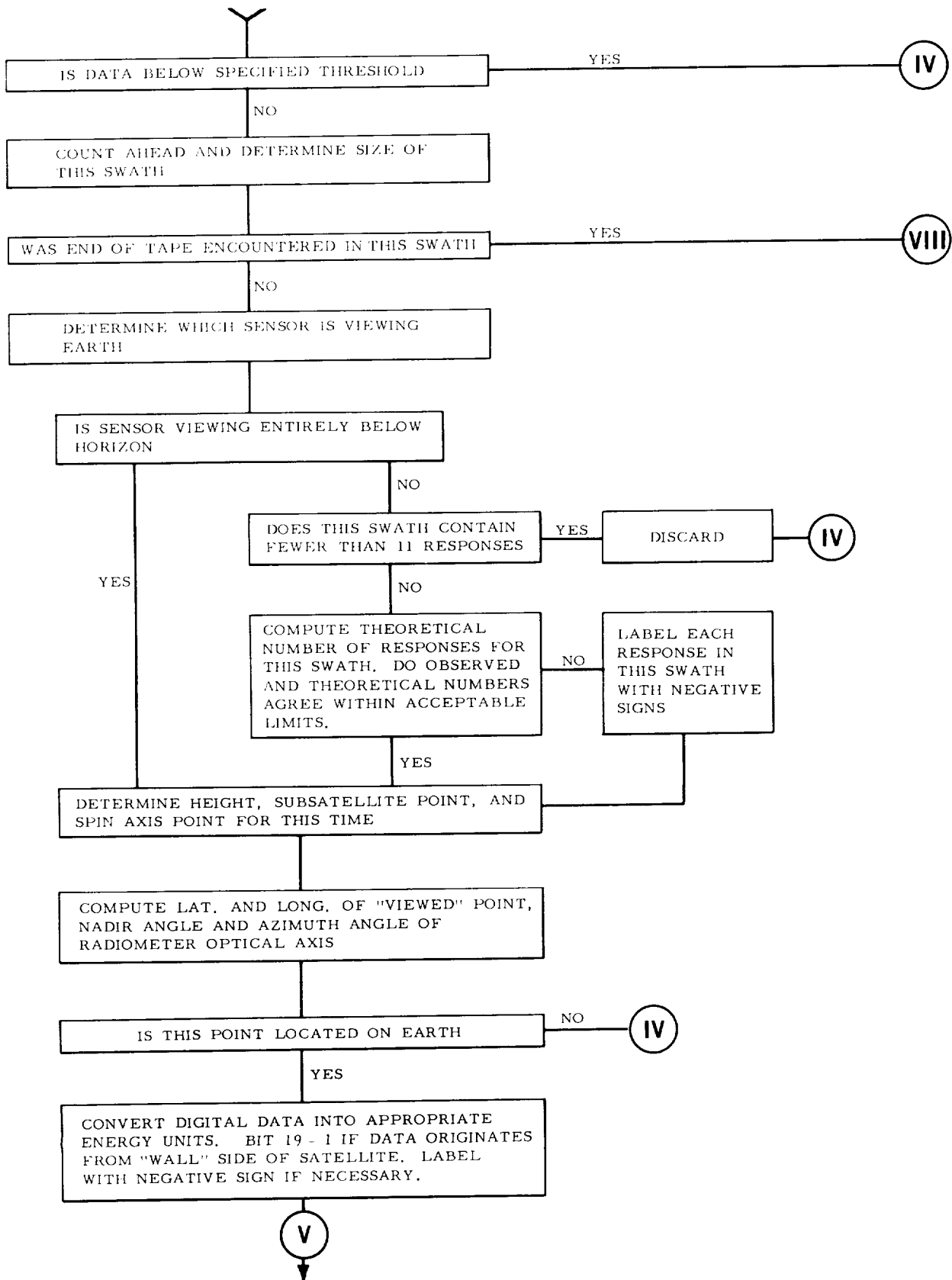
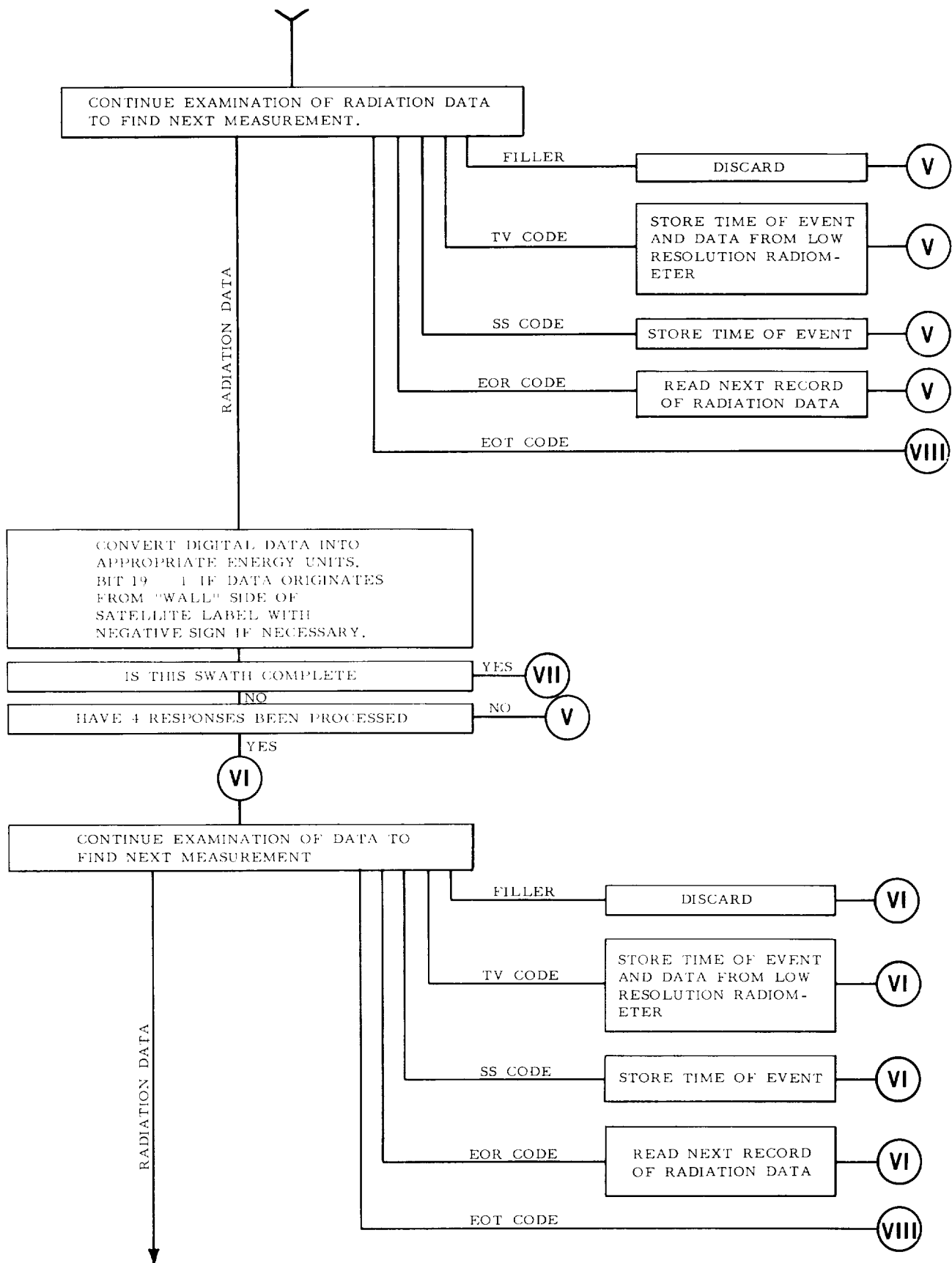
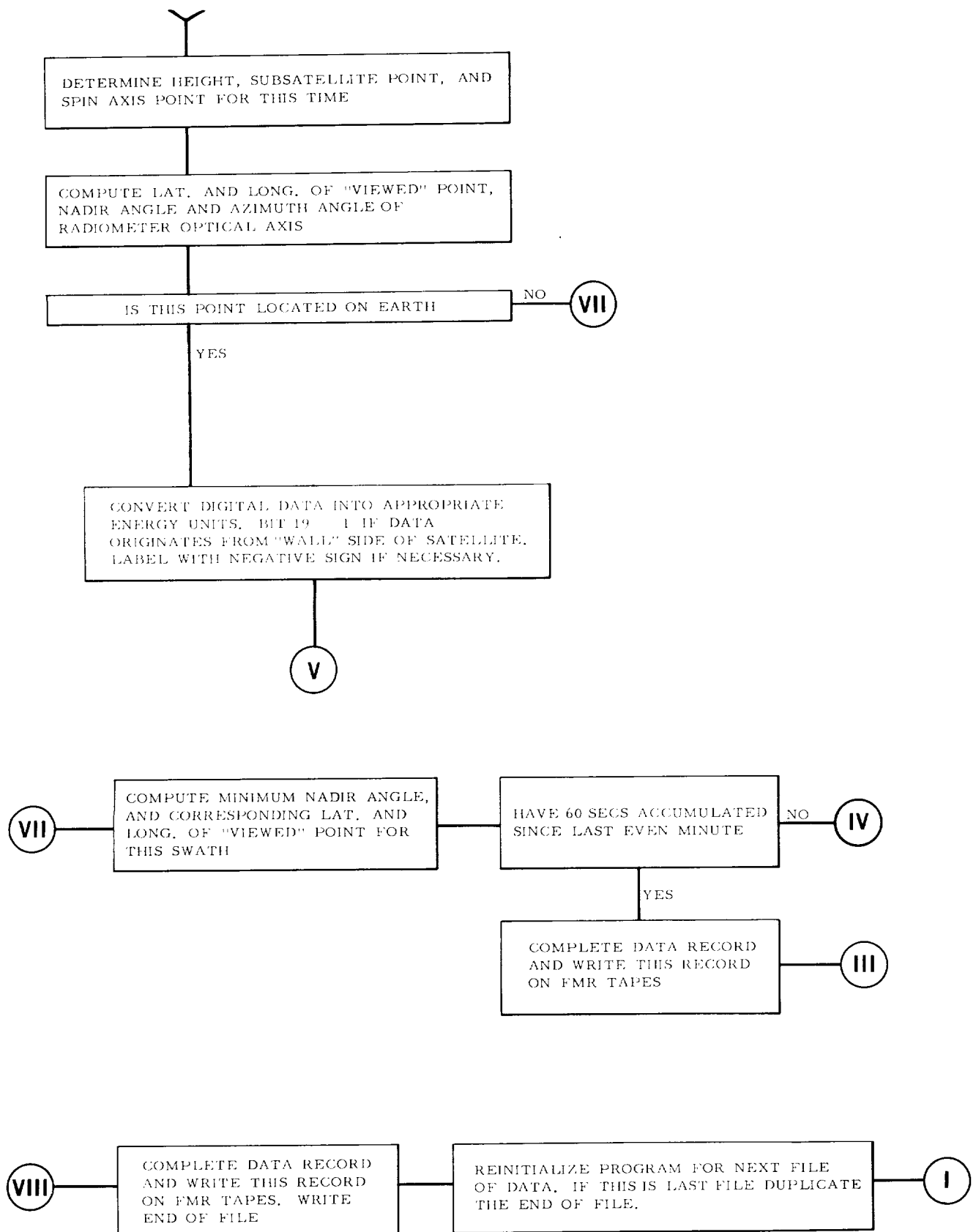
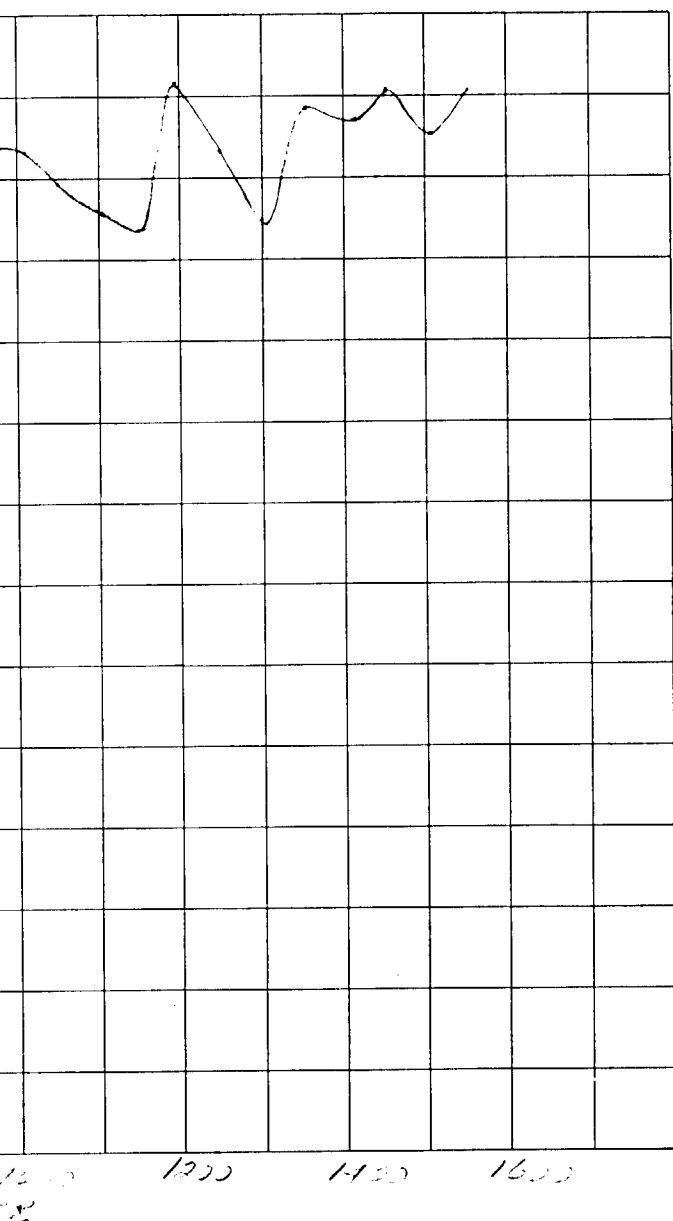


Figure 52—(a, b, c, & d)—Flow diagram for the IBM 7090 computer program used in reducing the radiation data.









Level vs. orbit number, Channel 1.

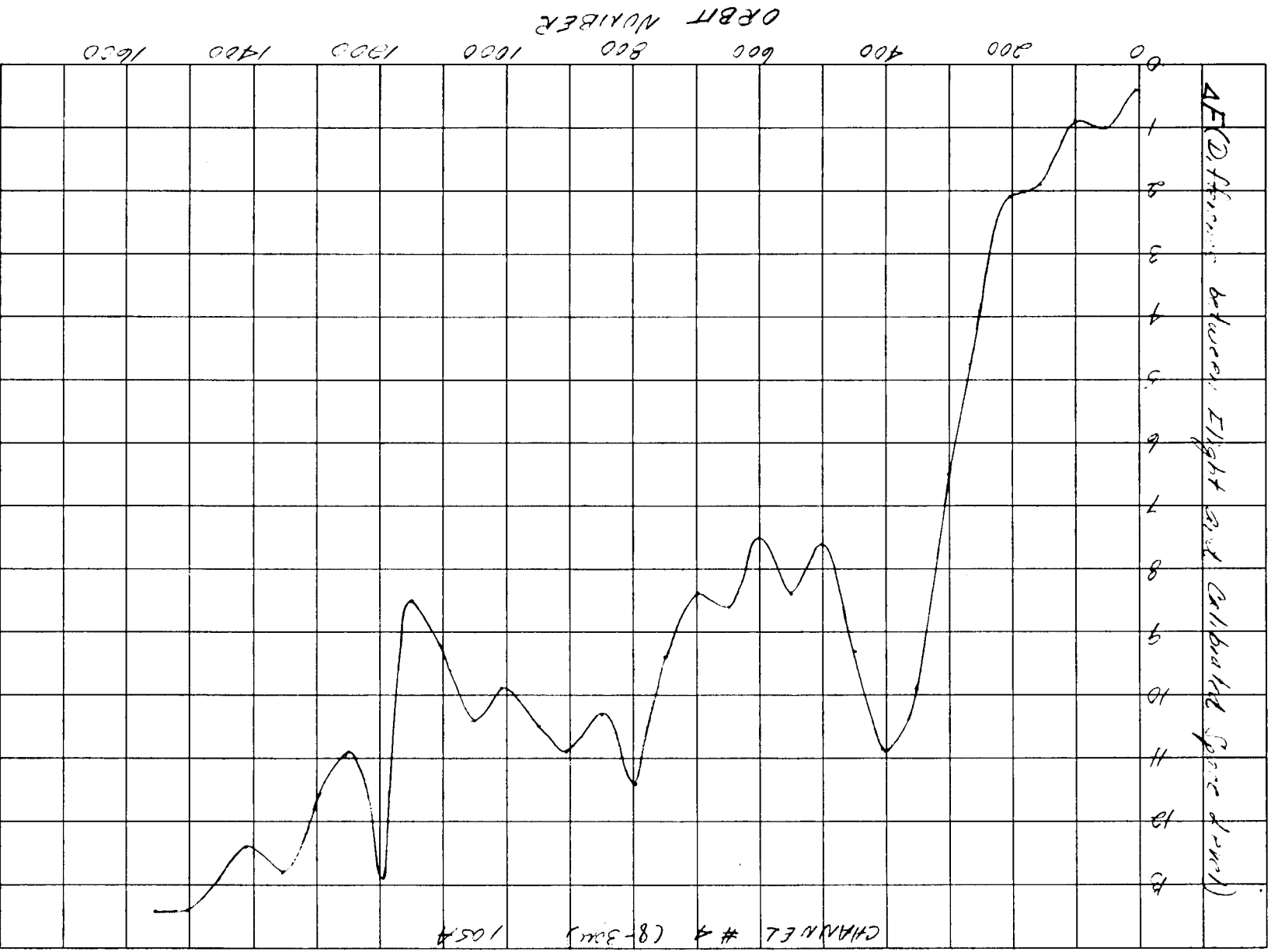


Figure 55—Difference between flight and calibrated space level vs. orbit number, Channel 4.

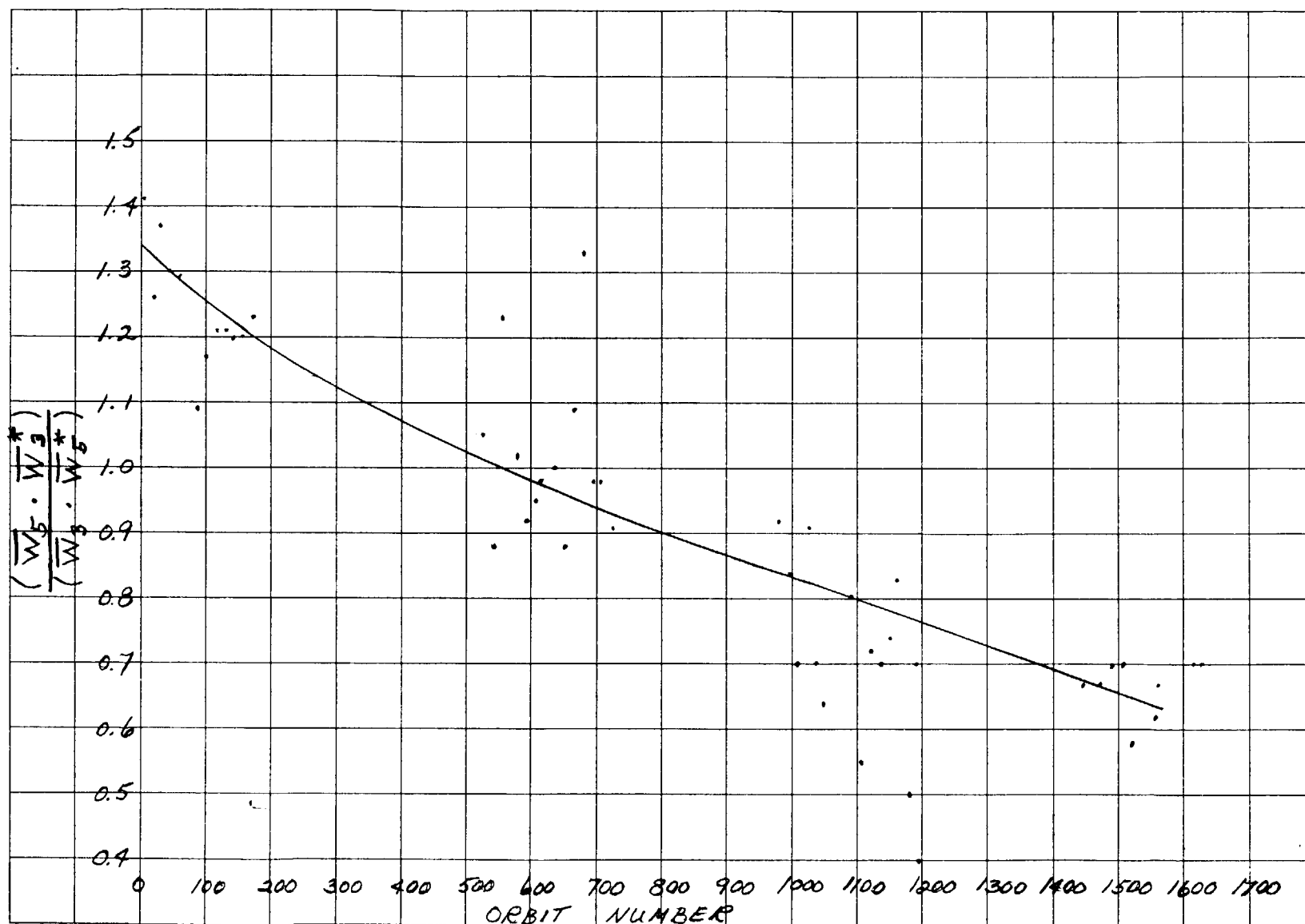


Figure 56—Ratio of \bar{W}_5 to \bar{W}_3 vs. orbit number.

